Doctoral Thesis

Fabrication of Various In-Plane Heterostructures by Using Conversion Reaction of Monolayer h-BN to Graphene on Platinum

Gwangwoo Kim

Department of Energy Engineering

Graduated School of UNIST

2019

Fabrication of Various In-Plane Heterostructures by Using Conversion Reaction of Monolayer h-BN to Graphene on Platinum

Gwangwoo Kim

Department of Energy Engineering

Graduated School of UNIST

Fabrication of Various In-Plane Heterostructures by Using Conversion Reaction of Monolayer h-BN to Graphene on Platinum

A dissertation submitted to the Graduate School of UNIST in partial fulfillment of the requirements for the degree of Doctor of Philosophy of Science

Gwangwoo Kim

12. 07. 2018

Approved by

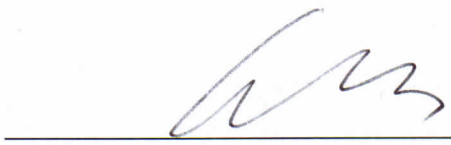

Advisor

Hyeon Suk Shin

Fabrication of Various In-Plane Heterostructures by Using Conversion Reaction of Monolayer h-BN to Graphene on Platinum

Gwangwoo Kim

This certifies that the thesis of Gwangwoo Kim is approved

12. 07. 2018

Advisor: Hyeon Suk Shin

Hyung-Joon Shin

Soon-Yong Kwon

Hyesung Park

Hu Young Jeong

Abstract

Recent advances in the synthesis of graphene and hexagonal boron nitride (h-BN) have enabled the large-scale growth of their monolayers. Although graphene and h-BN have similar atomic arrangements and a negligible difference of about 2% between their lattice constants, their electronic structures are completely different; graphene is a zero-band gap semiconductor, while h-BN is an insulator with a large band gap of 5.9 eV. Because of the structural similarities, it is expected that they can form a seamless interface when combined as a hybrid, leading to precisely controlled electronic and magnetic properties through proper interface control. In addition, the graphene edge without charge trapping sites can be realized similar to pristine graphene by passivating the boundary with insulating h-BN, which shows higher performance in the graphene electronics. However, the growth of heterostructures remains a challenge due to the difficulty in realized clean edges between graphene and h-BN. In this thesis, I will discuss the approach to develop various graphene/h-BN hybrid structures using conversion reaction of h-BN on platinum (Pt) catalyst. First, I will demonstrate the growth of highly crystalline h-BN monolayer on Pt metal substrate through a low-pressure chemical vapor deposition method. Next, I will discuss a catalytic conversion reaction of h-BN to graphene by using Pt catalyst to form an in-plane graphene/h-BN heterostructure. I proposed that this reaction proceeds through h-BN hydrogenation; subsequent graphene growth quickly replaces the initially etched region. Importantly, this conversion reaction enables the controlled formation of patterned in-plane graphene/h-BN heterostructures, without needing the commonly employed protecting mask, simply by using a patterned Pt substrate. Based on patterned conversion, I demonstrate on spatially controlled conversion of h-BN to graphene on an array of Pt nanoparticles (NPs) to realize an array of uniform GQDs embedded in h-BN sheet. The structure allows a dramatic reduction of the number of localized edge states along the perimeter of the quantum dots. I used such GQDs embedded in h-BN as part of van der Waals heterostructures to produce vertical single electron tunneling transistors operating in Coulomb blockade regime, which opens even larger flexibility when designing future devices.

Contents

List of Figures

[Chapter 2]

Figure 1. Schematic diagrams of the LPCVD system used for h-BN growth.

Figure 2. Scheme of electrochemical bubbling-based method used to transfer the h-BN layer.

Figure 3. Thermal decomposition of ammonia borane, forming borazine gas in the high temperature.

Figure 4. (a) Photograph of an h-BN layer transferred from Pt foil to a SiO_2/Si substrate. (b) Optical microscopy image of monolayer h-BN on a SiO_2/Si substrate, taken using 630 nm band-pass-filtered light. (c) SEM image of monolayer h-BN on a SiO_2/Si substrate.

Figure 5. Optical microscope images for monolayer h-BN on top of Si substrate with a 300 nm thermal oxide layer under various light wavelengths: (a) white light, (b) 630 nm, (c) 520nm, and (d) 425 nm band-pass filtered light.

Figure 6. (a) AFM image of monolayer h-BN on a SiO_2/Si substrate; (b) Raman spectrum of monolayer h-BN on a SiO_2/Si substrate; (c) UV-visible absorption spectrum and (d) optical band gap analysis of monolayer h-BN on a quartz substrate. XPS spectra of h-BN on Pt foil: (e) B1s spectrum and (f) N1s spectrum.

Figure 7. AFM images of h-BN transferred onto SiO_2/Si substrate after it was grown on Pt foil at different growth period: (a) 1 min, (b) 5 min, (c) 10 min, and (d) 30 min.

Figure 8. Raman spectra of h-BN transferred onto SiO_2/Si substrate after it was grown on Pt foil at different growth period: (a) 1 min, (b) 5 min, (c) 10 min, and (d) 30 min.

Figure 9. (a) A low-magnification TEM image of monolayer h-BN. (b) The corresponding diffraction pattern of monolayer h-BN showing a set of hexagonal patterns from single layer h-BN. (c) Atomic-resolution TEM image of monolayer h-BN (scale bar: 1 nm). (d) EELS spectrum of monolayer h-BN.

Figure 10. Atomic-resolution TEM image of h-BN. A triangular defect of single boron vacancy in single layer h-BN is indicated. Red and blue dots represent B and N, respectively. (Scale bar: 1 nm)

Figure 11. Monolayer h-BN grain mapping image with an over-laid background of the dark-field TEM image.

Figure 12. (a) Bright-field TEM (BFTEM) image of monolayer h-BN. (b) The corresponding diffraction pattern of monolayer h-BN. (c) Dark-field TEM (DFTEM) image taken from the diffraction

spot marked with the red circle in (b). (d) DFTEM image taken from the diffraction spot marked with the yellow circle in (b).

Figure 13. (a) Optical microscopy image of the four devices fabricated on monolayer h-BN for the four-point probe technique. (b) I-V curve of one of the monolayer h-BN devices, indicating the highly insulating nature of monolayer h-BN.

Figure 14. OM, SEM, and AFM images and Raman spectrum of monolayer h-BN grown on fresh Pt foil (a) and 100 times recycled Pt foil (b).

[Chapter 3]

Figure 1. Thermodynamic energy diagrams of conversion reactions. (a) Conversion reaction from graphene to h-BN; exothermic reaction. (b) Conversion reaction from h-BN to graphene; endothermic reaction.

Figure 2. The conversion reaction on SiO_2/Si substrate. (a,b) Raman spectrum and SEM image of h-BN film transferred onto SiO_2/Si substrate before and after conversion reaction for 20 min. After the conversion reaction, the characteristic peak of h-BN at 1,373 cm^{-1} is not shown due to broad peaks of amorphous carbon.

Figure 3. Conversion mechanism and Raman characterization. (a) Mechanism for the investigated conversion process. Boron, nitrogen, carbon, hydrogen, and platinum atoms are represented in yellow, blue, red, black, and gray, respectively. (b-g) Optical images (b-d) and Raman spectra (e-f) of h-BN, h-BN/graphene, and fully converted graphene samples transferred to SiO_2/Si substrates, resulting from the reaction times of 0 (b,e), 10 (c,f), and 20 min (d,g), respectively.

Figure 4. Morphology and microstructure. SEM and AFM images of h-BN (a,d), h-BN/graphene (b,e), and fully converted graphene (c,f) transferred onto SiO_2/Si substrates, of which conversion time was 0 min (a,d), 10 min (b,e), and 20 min (c,f), respectively. Inset of (e): Height profile corresponding to the white line in (e), indicative of significant wrinkles. (g-h) Atomic-resolution TEM images of monolayer h-BN and converted graphene. (i) EELS spectra of monolayer h-BN (red) and graphene (blue).

Figure 5. Measurement of surface potential for the i-G/BN heterostructure. (a) Optical image of the i-G/BN interface on SiO_2/Si substrate. (b) Raman spectra at different positions around the i-G/BN interface. (c) KPM image of the marked yellow area in (a), taken before transferring from the Pt substrate. (d) Plots of surface potential and BN concentration following the white line in (c).

Figure 6. STM analysis of early conversion. (a) An STM image of the i-G/BN heterostructure on Pt (111). The sample bias (V_s) =50 mV, and the feedback current (I_f) = 5 nA. The interfaces between h-BN and graphene are marked with red dashed lines. (b) A magnification image of the marked white square in (a). (c) Illustration of the i-G/BN heterostructure. (d) Height profile corresponding to the orange line in (a). (e) d*I*/d*V* spectra corresponding to the colored points in (a). (f-h) FFT results corresponding to the colored points marked in (a). Colored arrows indicate (01-10) directions of h-BN or graphene layers, relative angles were estimated as R0° (orange), R3° (green), and R9.5° (blue), respectively.

Figure 7. Scanning tunneling microscopy (STM) study on unreacted h-BN grain boundary in initial conversion reaction. (a) High-resolution STM image of h-BN on the step edge of Pt (111). The red dash line is marked on grain boundary of h-BN. (b) High-magnification image of the marked white square in (a). (c) Height profile corresponding to the orange line in (a). (d,e) The fast Fourier transform (FFT) results of h-BN (right) and h-BN (left) part. The rotational angle difference between two h-BN region was estimated as 23° from FFT images (d,e).

Figure 8. Early conversion of h-BN to graphene. (a-e) SEM images for the conversion times of (a) 0, (b) 0.5, (c) 1, (d) 3, and (e) 5 min, respectively. The SEM images were measured on Pt foil. All scale bars are 500 nm. (f-j) Schematic illustrations of time dependent reaction mechanism.

Figure 9. Effect of Pt step edges on the conversion reaction. (a) SEM image showing two Pt grains after the conversion reaction for 1 min. The contrast difference between two grains comes from the Pt grain orientation. (b,c) Zoom-in images of the green (b) and yellow (c) box in (a). The bright oval shapes in (b) are for h-BN and dark area is for graphene. (d) SEM image of conversion reaction on two Pt grains for 20 min shows full conversion to graphene. (e,f) Zoom-in images of the red (e) and blue (f) box in (d). Inset of (e,f): Raman spectra of fully converted graphene samples transferred onto SiO_2/Si substrate.

Figure 10. Effect of Pt grain boundary on the conversion reaction. (a,b) SEM images of conversion reaction on Pt grain for 1 min. The grain boundary of Pt is marked with the white line and the conversion reaction proceeds in the direction of red arrows. (c,d) Zoom-in images of the blue (c) and green (d) box in (b).

Figure 11. Schemes for two types of initial points in the conversion reaction. (a-c) scheme of the conversion reaction initialized on single defect in basal grain of h-BN. It induces graphene islands. (d-f) scheme of the conversion reaction initialized on grain boundary of h-BN. It induces h-BN islands.

Figure 12. Hydrogen-etching of h-BN on Pt and SiO_2/Si substrates. (a,b) SEM and AFM images of hydrogen-etched h-BN film transferred on SiO_2/Si substrate after the hydrogenation on Pt substrate. (c,d) SEM and AFM images of hydrogen-etched h-BN film on SiO_2/Si substrate.

Figure 13. The conversion reaction on Cu, Pt, and Ru substrates. (a,b) Raman spectrum and SEM image of h-BN film transferred onto SiO_2/Si substrate after conversion reaction on Cu substrate. (c-e) XPS spectra of (c) B 1s, (d) N 1s, and (e) C 1s on Pt substrate. (f-h) XPS spectra of (f) B 1s, (g) N 1s, and (h) C 1s on Ru substrate. The black and red lines are associated with films before and after conversion reaction for 20 min, respectively.

Figure 14. Fabrication of patterned i-G/BN heterostructures. (a) Mask-free patterning process on Pt-patterned substrate. The conversion only occurs at the Pt region. (b) Optical image of the graphene/h-BN stripes on SiO_2/Si substrate. (c) Raman spectra of the h-BN (red) and graphene (blue) regions marked in (b). (d) Raman mapping in the 2D (2630-2730 cm^{-1}) band for the marked area in (b).

Figure 15. Interface of patterned i-G/BN heterostructures. (a) Optical image of the interface between graphene and h-BN grown on patterned substrate. The Raman spectra were obtained at different positions (black line) with 500 nm interval in (a). The white dash line is marked on the interface of h-BN and graphene. (b,c) the spectrum of h-BN (b) was changed to that of graphene (c) in the region between 3 and 4 point. At point 4, the D band is large due to contribution of the interface region. It means that the interface between graphene and h-BN has the good sharpness with less than ~ 500 nm.

Figure 16. Comparison of patterned G/BN heterostructures. (a) Patterned conversion reaction using SiO_2 hard mask.[5] (b) SEM images of the graphene/h-BN stripes on Pt after the etching of SiO_2 mask. The removed SiO_2 masks on the h-BN regions are marked with white dashed lines. (c) Problem of patterned conversion using SiO_2 hard mask.

[Chapter 4]

Figure 1. The fabrication steps of GQD/h-BN in-plane heterostructure based on h-BN to graphene conversion catalyzed by Pt NPs supported by a substrate of SiO_2. (a) The self-assembly of diblock copolymer micelles PS-P4VP with H_2PtCl_6 on Si/SiO_2 substrate. (b) Transfer of h-BN monolayer on SiO_2 substrate covered by Pt NPs (blue spheres – boron atoms, yellow spheres - nitrogen). (c) Formation of the GQDs on top of an array of Pt NPs by catalytically-assisted CVD (red spheres – carbon atoms). (d) The obtained in-plane GQD/h-BN heterostructure after the removal of Pt NPs.

Figure 2. (a-b) The SEM image and Raman spectrum of the CVD grown pristine h-BN monolayer. (c-d) The corresponding XPS spectra: (c) Boron 1s, and (d) Nitrogen 1s.

Figure 3. (a-b) The SEM and AFM images of the as-grown layer of GQD/h-BN on an array of Pt NPs (7 nm) spread over SiO_2 substrate.

Figure 4. Size and spatial distribution of the GQDs. (a-c) The SEM images of 7, 10, and 13 nm sized arrays of Pt NPs on SiO_2 substrates, respectively. (d-f) Corresponding size distribution histograms of Pt NPs on SiO_2 substrates. Numbers give the average (marked by red lines) and the standard deviation. (g-i) The SEM images of GQD/h-BN samples prepared on pristine SiO_2. (j-l) Corresponding size histograms of GQD/h-BN samples. Numbers give the average (marked by red lines) and the standard deviation.

Figure 5. The XPS spectra of GQD/h-BN planar heterostructure on SiO_2 substrate. (a) Survey, and (b) Pt 4f spectra. Blue and red spectra are for as-prepared GQD/h-BN on Pt NPs/SiO_2 substrate (before the aqua regia treatment) and the GQD/h-BN after the aqua regia treatment to remove Pt NPs, respectively.

Figure 6. TEM images of GQD/h-BN. (a, c) Pt NPs on top of GQD/h-BN. (b, d) The GQD/h-BN after aqua regia treatment. The white dots in (a,c) are Pt NPs.

Figure 7. Characterization of GQD/h-BN interface of the in-plane heterostructure with GQDs of the size of 7 nm. (a) Raman spectra of GQD/h-BN planar heterostructure (red) and pristine h-BN (blue). XPS spectra of GQD/h-BN planar heterostructure: (b) boron 1s, (c) nitrogen 1s, and (d) carbon 1s spectrum.

Figure 8. EELS analysis of GQD/h-BN. (a) Schematics of EELS mapping of GQD/h-BN on Pt NPs/SiO_2. (b) TEM image of GQD/h-BN on Pt NPs. The white dots are 7 nm Pt NPs. (c-e) Corresponding EELS mapping images of (c) carbon, (d) boron, and (e) nitrogen, respectively. (f) Magnified image marked in (d). (g) The EELS spectra were obtained at different positions (yellow line, P1 to P10) with 2 nm spatial resolution in f by subtracting the background of the Pt signal from the original EELS spectra.

Figure 9. Scheme of ideal GQD/h-BN heterostructures with (a) zigzag and (b) armchair edges. (c) Estimated heterostructures with more C-B zigzag bonds compared to the C-N zigzag bonds. The binding energies for C-B zigzag, C-N zigzag, and armchair bond in the graphene/h-BN in-plane heterostructure are calculated to be 0.45, 0.41, and 0.39 eV, respectively, by DFT calculations[13].

Figure 10. (a) The measured IR spectra for the GQD/h-BN and mechanical exfoliated h-BN (2 nm thickness) on SiO_2 by AFM-IR. Three spectra on different points were measured for a GQD/h-BN sample. (b) Magnified spectra in the range from 1200 to 1500 cm^{-1}.

Figure 11. (a) UV-vis absorbance spectra of bare h-bN and GQD/h-BN heterostructure. (b) PL spectra of GQD/h-BN samples prepared on 7 (red), 10 (blue), and 13 nm (green) sized Pt NPs/SiO_2 substrate, respectively.

Figure 12. (a) PL spectra of bare h-BN/SiO_2 (green spectrum) and Pt NPs/SiO_2 substrate (black spectrum). (b) PL spectrum of h-BN on SiO_2 substrate (blue spectrum) after carrying out the conversion reaction without Pt NPs in the same condition. The PL spectrum of GQD/h-BN is provided as a reference in (a) and (b).

Figure 13. (a) Scheme of GQDs with the oxidized edges and sp^2 sub-domains isolated by oxygen-functional group (Origin 1). (b) Scheme of the fabrication process of as-prepared GQD/h-BN on Pt NPs/SiO_2 substrate before the treatment with aqua regia. (c) Scheme of bare GQD prepared by O_2 plasma treatment of CVD grown graphene. (d) SEM image of a bare GQD (~7 nm) array prepared in (c). (e) PL spectra of bare GQD (red spectrum) and as-prepared GQD/h-BN on Pt NPs/SiO_2 substrate (blue spectrum).

Figure 14. (a) Scheme of h-BN sheets with nano-sized holes. (b) AFM image of h-BN nano-sized holes by annealing process in H_2 atmosphere. (c) PL spectra of h-BN nano-sized hole (blue spectrum).

Figure 15. (a) Optical image of in-plane graphene/h-BN heterostructure on SiO_2 substrate.[16] (b) Raman spectra of graphene (red) and h-BN (blue) on SiO_2 substrate by using a 532-nm laser. Integration time: 5 sec (graphene), and 60 sec (h-BN). (c) PL spectra of graphene (red), h-BN (blue), and interface (green) by using a 266-nm laser. The reason for the weak PL intensity is because the fraction of the interface regions in the heterostructure is smaller than in the GQD/h-BN structure.

Figure 16. Fabrication procedure for van der Waals tunnel heterostructure comprising the stack of Si/SiO_2/20nm_h-BN/SLG/3L_h-BN/GQD_h-BN/3L_h-BN/SLG/10nm_h-BN. (a) Single layer graphene (SLG), indicated by white arrows, was transferred by flake peeling method on bottom h-BN supported on Si/SiO_2 substrate. (b) Trilayer h-BN, outlined by red dashed line, was then transferred on SLG shown in (a). (c) Separately a PMMA membrane was prepared with ~ 10nm h-BN, another SLG and trilayer h-BN was picked up using this h-BN. This PMMA membrane containing the stack of 3L_h-BN/SLG/10_h-BN was further aligned and dropped on GQD_h-BN on Si/SiO_2. To release this stack from Si/SiO_2, wet transfer procedure following standard KOH etching procedure was performed. (d) Finally, the heterostructure of GQD_h-BN/3L_h-BN/SLG/10nm_h-BN was aligned, and transferred on Si/SiO_2/20nm_h-BN/SLG/3L_h-BN shown in (b). Contacts to top and bottom SLG, as shown in (d), were made by standard electron beam lithography. Scale bar shown in (a) is same for all images.

Figure 17. The h-BN/Gr/2h-BN/GQD/2h-BN/Gr/h-BN multi-channel single electron tunneling transistors. (a) Schematic structure of the van der Waals stack. Double layer graphene system separated by hexagonal boron nitride layers with GQDs embedded in the central layer of h-BN. (b) The low excitation measurements of low bias region of (c). Green arrows indicate the tunneling events through the localized impurity states in the middle h-BN layer with 7 nm GQD. Impurity assisted features

correspond to the localized state which is located approximately 90 meV above the Dirac points in the graphene contacts. (c) $G(V_g,V_b)$ for a device with 7 nm GQDs. (d) The low excitation measurements of low bias region of (e), indicating the tunneling events through the localized density of states in the middle h-BN layer with 13 nm GQD. The olive arrows denote the localized states with the energy 140 meV below the Dirac point. (e) $G(\underline{V_g},V_b)$ for a device with 13 nm GQDs. The red (blue) dashed line mark the event of the Fermi level in the top (bottom) graphene layer aligning with the Dirac point. (f) The magnified plot of (e) denoting a peculiar shape of the Coulomb diamonds when the Fermi level in one of the graphene contacts aligns with the Dirac point. The dashed grey line indicates the cross-section presented in (h). (g) The conductance G(-30V, V_b) plot indicating both peaks of prominent peaks of overlapping diamond boundaries (red arrows) and background of peaks from impurity assisted-tunneling (green arrows) for a device with 13 nm GQD. (h) The conductance $G(V_g$, 0mV) plot indicating peaks occurring from overlapping diamonds in (f). Red arrows in all the plots indicate conductivity peaks which correspond to tunneling through single electron states in GQD.

Figure 18. T = 1.5K tunneling conductance $G(V_b,V_g)$ of Si/SiO_2 substrate supported Gr/h-BN/Gr heterostructures. (a) Tunneling through pristine h-BN trilayer mounted in-between two graphene monolayers (colour scale is blue to white to red, 20nS to 2μS to 4μS). Dark Blue *X* shaped region corresponds to the event of the passage of chemical potential through DPs of graphene layers; vertical features represent phonon-assisted resonant tunneling process. (b) Tunneling through impurity states of low quality tetralayer h-BN mounted in-between monolayer graphene electrodes (colour scale is blue to white to red, 0nS to 20nS to 40nS). Peaks in conductance (red and white) correspond to the tunneling through localized states and follow the square root dependence.

Figure 19. T = 260 mK tunneling conductance $G(V_b,V_g)$ of Si/SiO_2 substrate supported h-BN/Gr/2h-BN/CVD h-BN/2h-BN/Gr/h-BN heterostructure. The area of the device is 82 μm^2. Note, the middle h-BN monolayer was grown by CVD, but no GQD were formed on it. Note, significantly lower conductivity (even though the area of the device is significantly larger than for those presented in the main text) due to the absence of the additional conductance channels due to GQD. There is a small number of the impurity states, however, which might be originating from either defect in the CVD h-BN or due to contamination in between the layers introduced during the fabrication.

Figure 20. Modelling of the single electron charging effect. (a-c) Schematic representation of a single electron charging effect. The corresponding electrostatic lines are denoted in (d). (d) Modelling example of the alignment of the different energy levels in a device with 13 nm GQD. Red (blue) dashed lines - Fermi level in top (bottom) graphene electrode aligning with the Dirac point. Purple lines – Fermi levels in the graphene contacts being aligned with the localized state located in the middle h-BN layer with energy 140 meV below the Dirac point. The set of solid red (blue) lines correspond to single electron

energy levels in GQD aligning with the Fermi level in the top (bottom) electrode. Space between four of such lines forms a Coulomb blockade diamond. Note the distorted shape of the diamond when the Fermi level in the contacts passes through the Dirac points.

Figure 21. Low density non-periodic array of GQD embedded in h-BN matrix and h-BN/Gr/2h-BN/GQD/2h-BN/Gr/h-BN multi-channel single electron tunneling transistors based on such GQD. (a) SEM image of a GQD/h-BN sample obtained after the transfer of h-BN monolayer Pt NPs/SiO_2 substrate and the conversion reaction. It shows GQDs with a long spacing (0.5 to 1.5 μm), marked by white arrows. (b) $G(V_g,V_b)$ for a device with such GQDs.

List of Tables

Chapter 1: Research Background for the In-Plane Heterostructure of Graphene and Hexagonal Boron Nitride

1.1 Overview

Graphene and hexagonal boron nitride (h-BN) are atomic-scale hexagonal lattices made of carbon and boron, nitrogen atoms, respectively. However, graphene has a zero-bandgap semi-metallic property with remarkably high carrier mobility at room temperature[1–3], whereas h-BN[4–9] is an insulating material with a large bandgap of ~6 eV. Accordingly, if precise two-dimensional (2D) domains of graphene and h-BN can be seamlessly stitched together, the in-plane heterostructure with interesting electronic applications could be created[10-11]. The study of the heterostructures of graphene and h-BN has just been started, although theoretical calculations have predicted that various properties such as the band gap opening,[12-14] magnetic properties,[15] and thermal transport properties,[16] which can be controlled by manipulating the size and concentration of each hybrid domains. Continuous atomically thin films consisting of two 2D materials with different atomic compositions have received much interest in terms of their interfaces.[10-11] In a graphene/h-BN heterostructure, the two materials each have hexagonal structures with a similar lattice constant difference of only 2%, so the growth of hybrid structures with lateral hetero-junctions and the formation of interfaces are very interesting.

In this chapter, I review recent trends in the fabrication and property of in-plane graphene/h-BN heterostructures. Two types of sub-chapters are handled: 1) preparation and 2) properties of in-plane graphene/h-BN heterostructures.

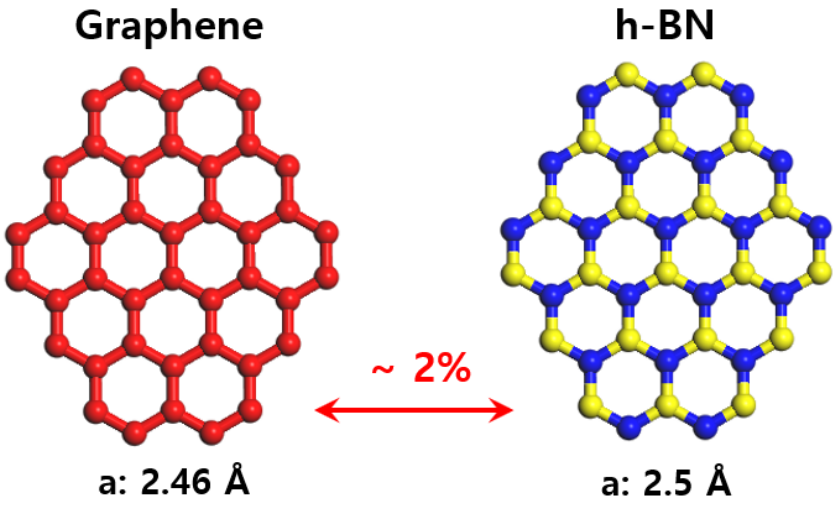

2D material	Element	Electronic property	Bandgap
Graphene	C	Semi-metallic	0 eV
h-BN	B, N	Insulating	~6 eV
TMDCs	Mo, W... + S, Se...	Semiconducting	1.2 ~ 2 eV

*h-BN: Hexagonal Boron Nitride
*TMDCs: Transition Metal Dichalcogenides

Figure 1. Introduction of graphene and hexagonal boron nitride

1.2 Fabrication of In-Plane Graphene/h-BN Heterostructures

Here, we introduce the synthetic methods for fabricating in-plane graphene/h-BN heterostructures and their detailed structures in three sections: 1) growth of BNC, 2) patterned growth, and 3) in-plane epitaxial growth.

1.2.1. Growth of Boron Nitride-Graphene (BNC) Hybrid Structure

To modulate the electronic structures of graphene, various approaches to opening the band gap to convert its semi-metallic character to semiconducting have been investigated. Chemical doping is one feasible approach, and experimental and theoretical studies have shown the that substitution of B or N atoms for the C atoms in graphene is possible.[17-18] Also, a wider band gap in the electronic structure has been predicted for the BC_2N monolayer structure.[19] In 2010, the Ajayan group first reported a synthetic method for producing atomic layers of h-BNC and realized the first in-plane 2D heterostructure.[20] These h-BNC heterostructures were synthesized on Cu foil by CVD from simultaneously introduced CH_4 and ammonia borane as precursors. Their structures were confirmed in high resolution transmission electron microscope (HRTEM) images. For example, one TEM image taken from a two-layered structure (Figure 2a) shows a clear Moiré pattern, which implies turbostratic stacking with a non-zero rotational angle between the two layers, which is associated with a lack of AB stacking. A 2D fast Fourier transform (FFT) pattern (inset of Figure 2a) indicates a relative rotational angle of 16° between the two layers. Although individual atoms can be resolved in the hexagonal packing, it is difficult to identify the positions of the individual B, C, and N atoms in the TEM image because there is only a small difference in their atomic sizes. Therefore, electron energy-loss spectroscopy (EELS) measurements and X-ray photoelectron spectroscopy (XPS) of the h-BNC film were carried out to determine not only their atomic composition but also the types of bonds between atoms. These spectroscopic characterizations revealed that all three elements are sp^2 hybridized, but the domains of graphene and h-BN exist separately in the film. Nonetheless, small photoemission peaks from C-B and C-N bonding were confirmed in XPS spectra, which indicates covalent bonding between the graphene domains and h-BN domains. A schematic drawing of the structure is displayed in Figure 2b. There are two different optical band gaps from absorption edges, which indicates that both the h-BN and graphene domains are large enough to have their individual optical band gap identities.

The Ajayan group recently also reported another approach to forming h-BNC heterostructures called the topological substitution reaction, which converts graphene sheets to h-BN layers.[21] During the reaction, the h-BNC heterostructure can form as an intermediate, and the composition ratio between

graphene and h-BN has been successfully adjusted by controlling the reaction conditions. In brief, CVD-grown graphene transferred onto a silicon substrate is loaded into a vacuum quartz tube and heated up to 1000 °C with an Ar flow. For the reaction, preloaded solid boric acid power is heated up to 300–600 °C with an ammonia gas flow. A two-step mechanism for the substitution reaction was suggested by a DFT calculation. In the first step, nitrogen or boron atoms replace carbon atoms around structural imperfections in the graphene such as the defect edges or carbon atoms functionalized with impurities. The second step is the nucleation of h-BN around the embedded nitrogen atoms, because the subsequent substitution of a boron atom or a BN pair is expected to be much easier around the embedded nitrogen atom than in the bulk graphene. Turbostratic stacking was observed in the multilayer h-BNC with a hexagonal structure consisting of B, C, and N, resulting in different Moire patterns.

In addition to the h-BNC heterostructures consisting of graphene and h-BN domains explained above, 2D boron-carbon-nitrogen alloy structures have been also observed in several studies. These structures are actually difficult to classify as in-plane heterostructures, but they are important from the viewpoint providing a critical clue to understanding the interface formation in in-plane graphene and h-BN heterostructures and elucidating the mechanism of the conversion reaction from graphene to h-BN. The Sutter group reported a mixed boron-nitrogen-carbon phase consisting of h-BN doped with C at the interface between graphene and h-BN that formed during sequential graphene and h-BN growth.[22] The Loh group also observed a boron-carbon-nitrogen alloy during the reaction converting graphene to h-BN.[23] In their work, a single-crystalline Ru (0001) substrate was used as a substrate, and all reactions were carried out under ultrahigh vacuum (UHV) conditions. For the conversion reaction, the graphene sample on Ru (0001) was annealed at 900–1000 °C in vaporized borazine. The reaction process can be processed in which borazine molecules are catalytically decomposed by Ru. The atomic hydrogen generated by this decomposition may participate in the etching of carbon atoms from the graphene. A STM study revealed structural changes depending on the borazine dosage. At a low borazine dose of 5 Langmuir (1 Langmuir corresponds to an exposure of 10^{-6} torr for 1s), the brick and mortar structure shown in Figure 2c was observed. STM studies revealed that the threads in the mortar structure are graphene nanoribbons, while brick region consists of a mixed h-BC_2N structure. From the different elemental contrasts (carbon atoms are bright and BN is dark), two dominant isomers were identified (Figure 2d), which well agrees with the theoretical prediction of the most stable configurations of h-BC_2N polymorphic structures.[19, 24] Although the approaches taken by Ajayan group and by Loh group are conceptually similar, the intermediate structures are totally different. The main difference between the two results is the type of substrate. However, the exact catalytic role of substrate and the reaction mechanism are still not clearly understood, and further investigations are required to determine them.

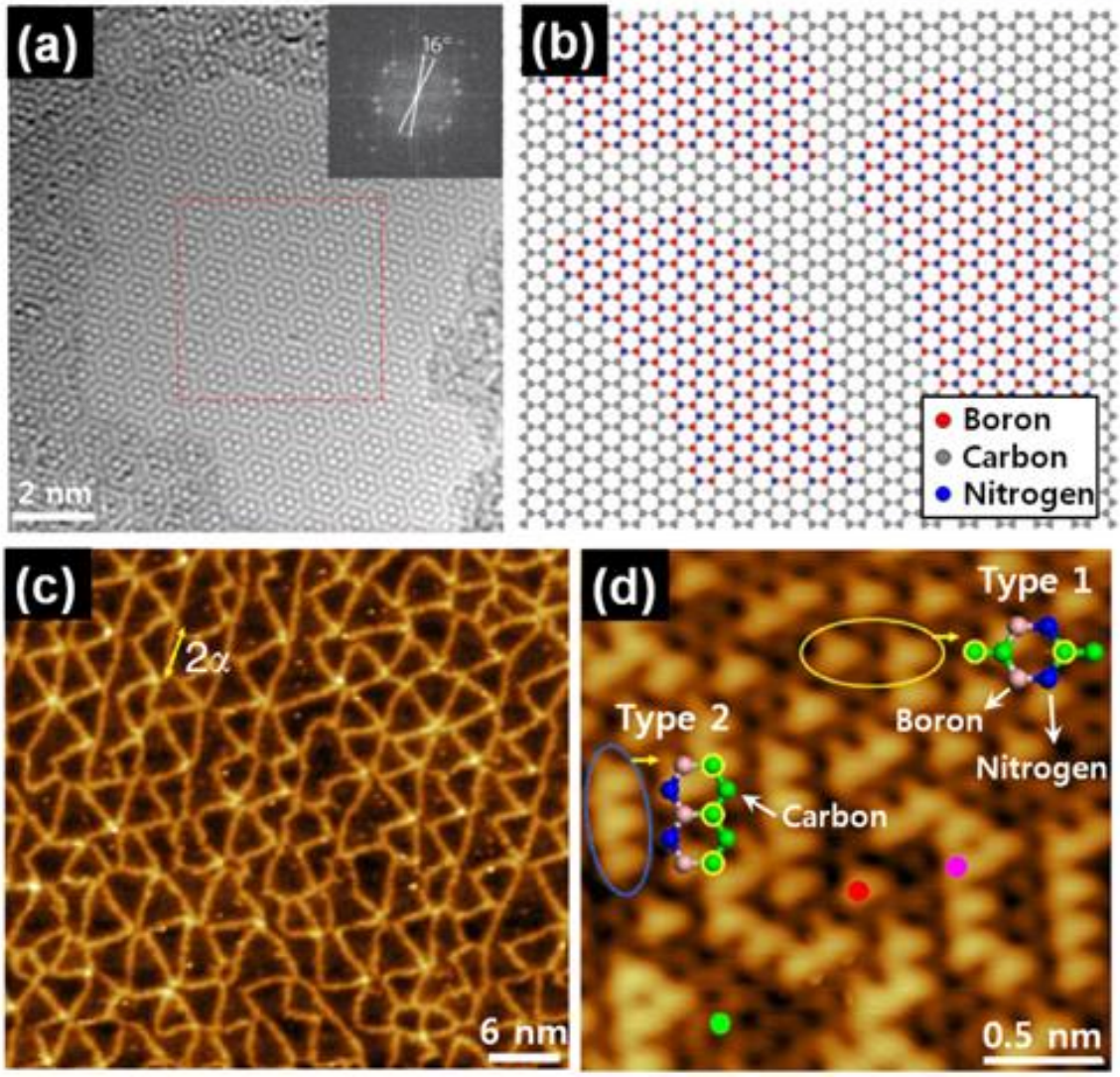

Figure 2. (a) HRTEM image of a two-layer region. The FFT in the inset reveals a two-layer packing with a relative rotational angle of 16°. (b) Atomic model of the h-BNC film showing hybridized h-BN and graphene domains. (c) Phase-segregated GNRs modulated by the Moiré superlattice encircling the mixed h-BC_xN domains to form a brick-and-mortar pattern. (d) Atomic imaging of h-BC_2N revealing the two most stable isomer structures, as illustrated in the in-sets.

1.2.2. In-Plane Epitaxial Growth

Owing to the chemical instability of graphene or h-BN edges,[25] they can have catalytic ability for the in-plane epitaxial growth. The possibility of in-plane epitaxial growth of graphene and h-BN heterostructures has been demonstrated both on single-crystalline substrates and on bulk Cu foil. Sutter et al. first reported two-step growth i) growth of graphene islands, and ii) continuous growth of h-BN from edges of graphene islands of laterally connected graphene and h-BN.[22] However, a mixed B-C-N phase was observed between the graphene and h-BN under normal reaction conditions, as explained in section 1.2.1. By applying a low pressure of oxygen to remove carbon adatoms on the Ru (0001) surface, atomically sharp interfaces could be obtained. In contrast, Yabo et al. reported a similar structure that was obtained in the reverse order, where h-BN islands were first grown on the Rh (111) surface and then graphene was patched onto the uncovered surface until the hybrid structure completely evolved (Figure 3a and b).[26] Even on Cu foil, lateral epitaxy between graphene and h-BN has recently been confirmed. Han et al.[27] and Liu et al.[28] individually reported the epitaxially continuous growth of an h-BN layer from graphene edges grown on Cu foil (Figure 3c). These authors used very similar methods in which highly diluted CH_4 gas was used as the carbon precursor. This method is known to grow monolayer graphene with good crystallinity and well-defined zigzag edges.[29-30] As a precursor for h-BN, ammonia borane (NH_3-BH_3) was used. The only difference between the methods is that Han et al. maintained a high reaction temperature during two-step growth,[27] whereas Liu et al. cooled down the sample after the growth of graphene and etched the graphene edges with hydrogen before BN growth.[28] Using an advanced growth technique, an in-plane graphene/h-BN/graphene heterostructure is demonstrated by alternatively introducing the precursor ethylene and borazine gases every 50 s (Figure 3d).[31] The contrast in the SEM image differentiates the graphene strips from the hBN strips grown on Ru(0001) (Figure 3e–g). This result implies that in-plane heteroepitaxy is preferred at the edge of each material. The detailed interface structure is discussed in section 1.2.3.

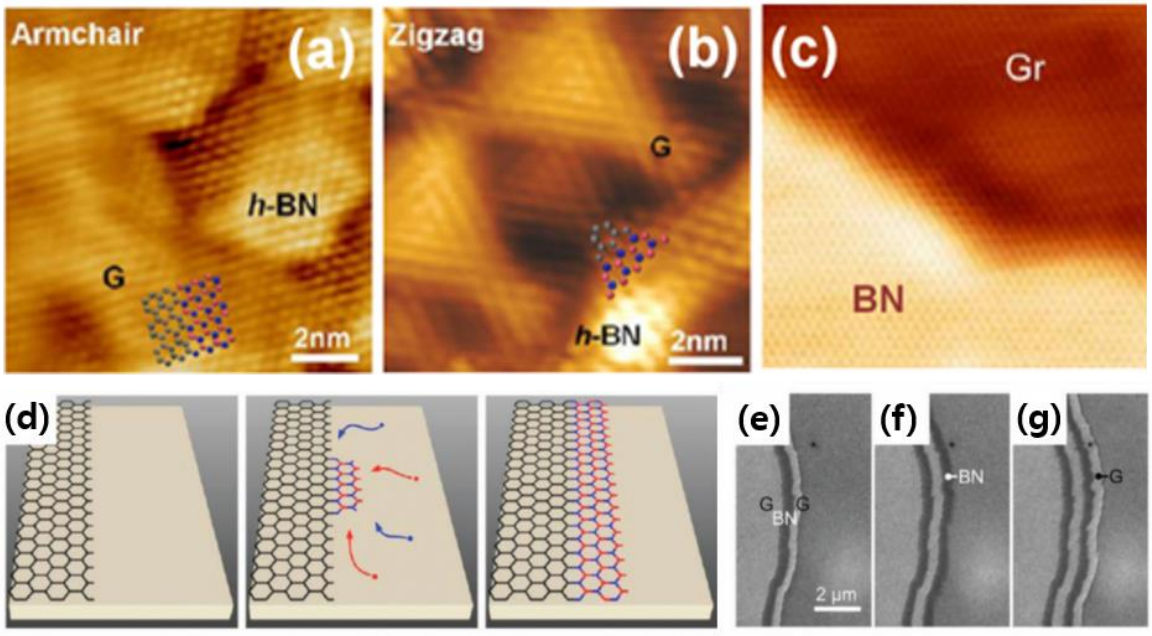

Figure 3. (a, b) Atomically resolved STM images of armchair and zigzag linking edges, respectively. (c) STM image of a graphene-BN boundary (7.5 nm by 5 nm, sample bias 0.5 V). (a) Schematic illustration of the sequential growth of h-BN and graphene at the edge of a 2D seed crystal. (e–g) Real-time microscope images of the stepwise growth of a monolayer superlattice of graphene and h-BN strips on Ru (0001) via alternating the exposure of ethylene and borazine, respectively at 700 ^{o}C.

1.2.3. Patterned Regrowth

Scalable and patterned heterostructures are required to realize integrated circuits in a 2D atomic layer. Park's group produced lateral junctions between h-BN and graphene by a process called patterned regrowth, which is described in Figure 4a.[10] They first grew graphene on Cu foil, then carried out the lithographic patterning, and finally made lateral junctions by growing h-BN in the areas where graphene was removed by the lithographic patterning (Figure 4a). In this way, structures like atomically thin circuitry with a metal and an insulator were formed. Figure 4b shows a dark-field TEM image of a boundary region of graphene and h-BN. On the other hand, the Ajayan group realized lateral h-BN/graphene heterostructures by the opposite patterned regrowth. They first prepared a lithographically patterned h-BN layer and then grew graphene.[11] This allows for the creation of an owl-patterned in-plane graphene/h-BN heterostructure (Fig. 4d). The ADF-STEM image clearly shows the border between the hBN and graphene regions (Fig. 4e), but the atomic orientation was not explicitly observed at the interface. Instead, the existence of h-BN and graphene was indirectly confirmed by two different diffraction spots in the 2D FFT pattern. The difficulty in obtaining atomic resolved STEM images at the interface can be attributed to residues of polymers used in photolithographic and transfer processes and the highly corrugated nature of the Cu and Ni foil.[32] Furthermore, the EELS mapping image of the boron atoms shows the sharp interface between the hBN and graphene regions (Fig. 4f). However, the two sets of hexagonal spots from the hBN and graphene lattices at the junction region in the FFT pattern are randomly rotated (not shown here), indicating that in-plane epitaxy growth does not take place.

1.2.4. Patterned Conversion of Graphene to Hexagonal Boron Nitride

The patterned regrowth involves removal of selected areas of graphene or h-BN. On the other hand, patterned 2D lateral heterostructures can also be achieved using another approach such as substitution or conversion from graphene to h-BN without an etching process. This method was already described in section 1.2.1 to explain the methods for the growth of h-BNC structures as intermediate materials. By using a protecting layer like SiO_2 or a metal layer, only non-protected graphene can be converted into h-BN. In these approaches, patterned lateral heterostructures consisting of graphene, h-BN, and h-BNC were also achieved by twice patterned regrowth (1. 50% conversion for h-BNC, and 2. 100 % conversion for h-BN), as shown in Figure 8c.[21]

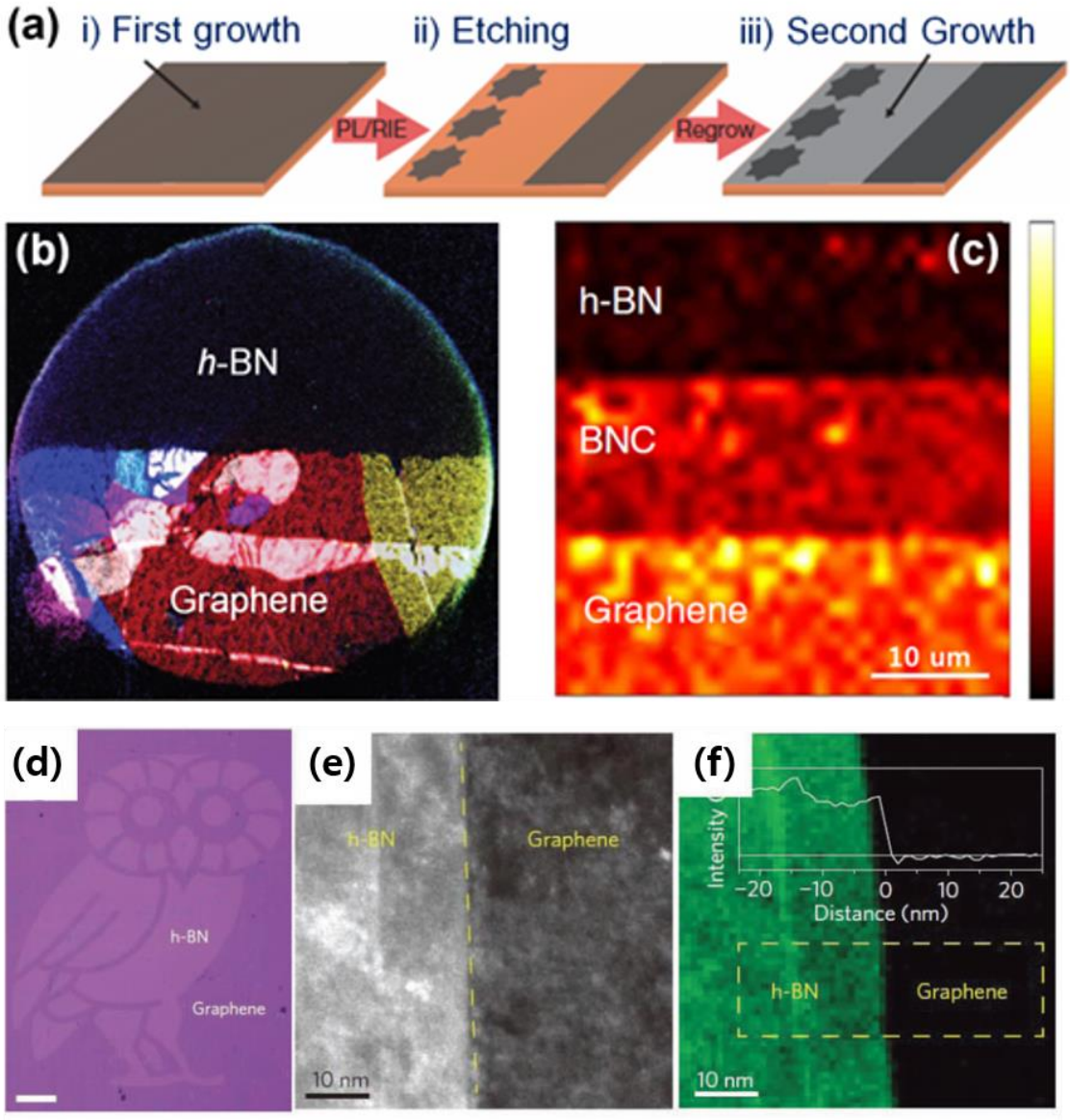

Figure 4. (a) Schematic for formation of atomically thin lateral heterojunctions using photolithography and reactive ion etching. (b) False-colour DF-TEM image of a suspended graphene/h-BN sheet with the junction region. (c) Raman mapping at 2D peak (2700 cm^{-1}) of graphene/h-BNC/h-BN alternating strips synthesized by this two-step conversion. (d) Optimal image of a micrometer-sized owl pattern for an in-plane graphene/h-BN heterostructure; the scale bar is 100 mm. (e) STEM-ADF image of the graphene/h-BN interface. (f) EELS mapping of boron from the area in (e). The inset shows the intensity profile along the trajectory in the dashed box.

1.3. Properties of In-Plane Graphene/h-BN Heterostructures

Unique properties have been predicted for covalently bonded interfaces between monolayer graphene and h-BN. Owing to the short history of lateral heterostructures, many properties of these interfaces are still unknown, but there has been a meaningful advance in the measurement of such properties in the recent few years. In these sections, the electrical and optical properties of h-BNC heterostructures and the patterned 2D lateral heterostructures are demonstrated. In addition, the interface structure and lateral epitaxy are discussed.

1.3.1. Electrical Properties of In-Plane Graphene/h-BN Heterostructures

The first h-BNC film synthesized by Ci et al. exhibited a wide band gap of ~18 meV, as estimated by temperature-dependent resistance measurement.[20] The UV absorption spectra presented the two different optical bandgaps further verifying that the hybrid domains are composed of h-BN and graphene nano-sized domains rather than substitutional doping or alloyed phase of h-BN and graphene. A small electron and hole mobility was observed in the h-BNC based FETs, which might well be due to the electron scattering at the boundaries between h-BN and graphene domains. Different from this result, vertically aligned hBN-C phase-separated composite nanosheets were observed on Si/SiO_2 substrates by a non-catalytic CVD-based strategy.

The transfer characteristics of an h-BNC film that was converted from graphene by the topological substitution reaction were also investigated.[21] Interestingly, this work showed that the carrier mobility and on/off ratio in a FET fabricated with a ternary h-BNC 2D layer could be tuned through a controllable transition from highly conductive graphene, to semiconducting h-BNC, and finally to insulating h-BN as the concentration of h-BN substituted in the graphene layer increased. The changes in the electric parameters such as the carrier mobility and on/off ratio of the FETs were systematically measured, as plotted in Figure. 5a. In a complete conversion cycle (in which the atomic concentration of BN increases from 0 % to 100 %), the resistivity of h-BNC first increases slightly and then goes up exponentially. The mobility exhibits the inverse trends. The source-drain current on/off ratio goes up initially and then decreases at a 40% BN concentration (Figure 5a). The semiconducting-like behavior, on-off ratio may be induced by an electron confinement effect induced by the quasi-one-dimensional conducting channel in h-BNC that arises with increasing h-BN concentration. However, the small graphene domains might be disconnected at higher BN concentrations, resulting in the decrease in the on/off ratio. This mechanism of semiconducting behavior is similar to that of the band gap opening observed in graphene

with patterned hydrogen adsorbates.[33] The electronic structures of a BNC mixed structure (h-BC_2N) were also investigated using scanning tunneling spectroscopy (STS) before and after decoupling from the Ru substrate (Figure 5b).[23] Upon intercalation, excluding the influence of hybridization between h-BC_2N and the metal substrate, an energy gap of 2 eV is observed in the averaged STS data (blue line), which is meaningful because the theoretically predicted band gap is 1.6 eV for the h-BC_2N configuration.[19, 34] The carefully patterned graphene and h-BN in-plane hybrid structure incorporating both metal and dielectric components could be a good supplement for various types of graphene-based devices such as resonators, amplifiers, multipliers, and mixers for high-frequency applications. Liu et al. demonstrated a graphene/h-BN resonator as one possible application (Figure 5c).[11] In addition, these heterostructures could be fabricated by a multiple transfer process for ultraflat three-dimensionally interconnected devices (or three-dimensional electronics) (Figure 5d).[10] This approach provides the possibility of mechanically flexible and optically transparent electronics.

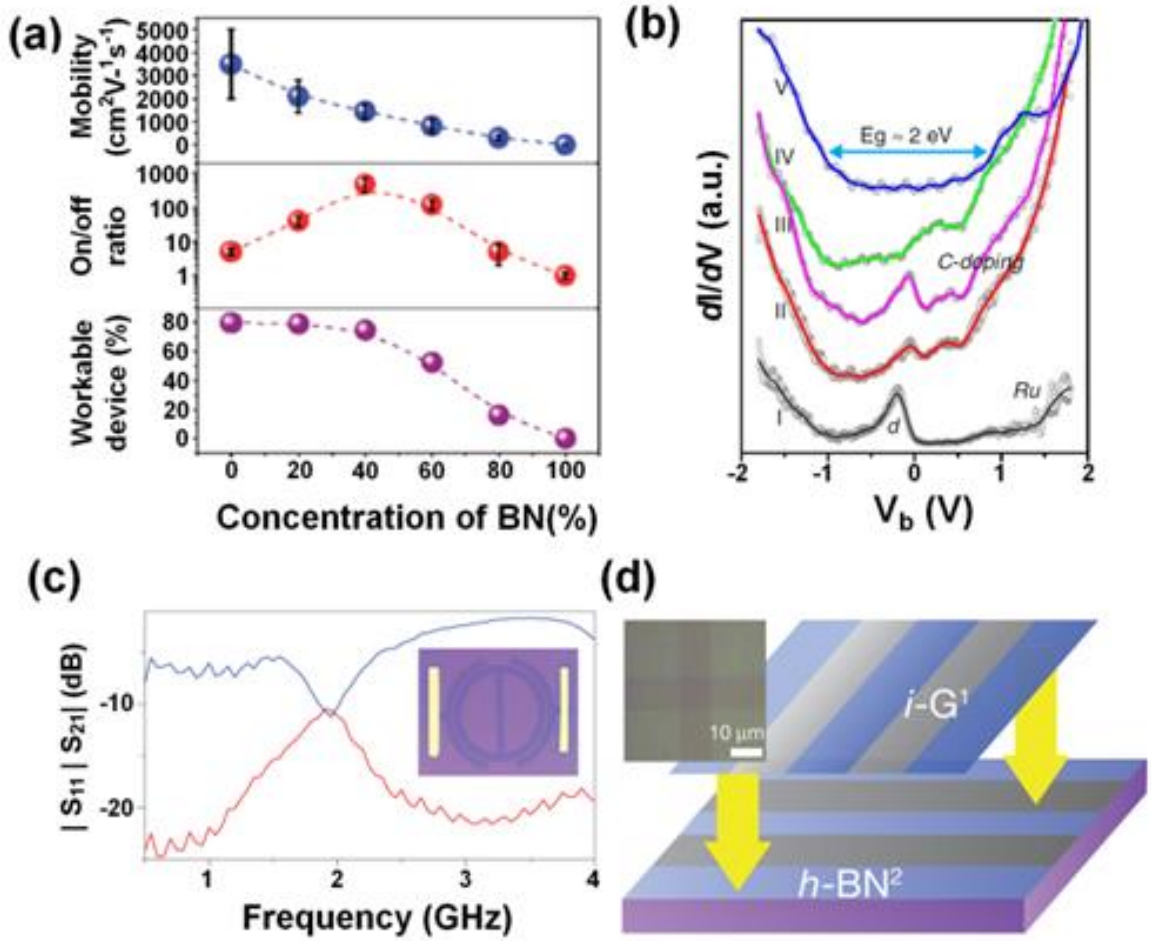

Figure 5. (a) Plot of the mobility, on/off ratio, and percent-age of workable devices versus the BN concentration. (b) The *dI*/*dV* spectra collected at bare Ru (I), (II) bright spot (red spot in Figure 2d), (III) bright clusters (pink spot in Figure 2d), (IV), dark region (green spot in Figure 2d), and (V) decoupled BCN. (c) Plot of insertion (|S21|) and return (|S11|) loss versus frequency. Inset: optical image of the two-dimensional graphene/h-BN layer resonator. (d) A schematic of a multiple transfer process for ultraflat three-dimensional interconnects. Inset of (d) is an optical image of device.

1.3.2. Interface and lateral epitaxy

For lateral heterostructures, the main questions are how and what chemical bonding occur at the interface between two different materials forms and how coherent the lattice between the two different materials is. Recent STM or TEM studies of the interface have provided important information to answer these questions. Gao et al. investigated the interfacial structure between graphene and h-BN by STM.[26] In particular, the STM study combined with a theoretical prediction revealed that that zigzag interfaces (Figure 3b) are energetically more favorable than armchair interfaces (Figure 3a). The atomic resolution STM image obtained in their work clearly showed obvious lateral epitaxy between graphene and h-BN, and such epitaxy was also confirmed for other graphene and h-BN heterostructures synthesized on Ru (0001).[22] However, owing to the strong interactions of graphene with Ru[35-36] or Rh[35, 37] and of h-BN with Ru[38-39] or Rh[39-40] the lattice direction of graphene or h-BN is aligned with the metal lattice direction, i.e., the relative rotational angle with respect to the metal surface is zero. Therefore, it is not clear whether the identical directional orientation between the graphene and h-BN is mainly due to the vertical epitaxy with the metal surface or due to the lateral epitaxy between graphene and h-BN.

Unlike single crystalline substrates like Ru (0001) and Rh (111), various rotational orientations of graphene and h-BN on Cu have been confirmed.[36] Therefore, the interaction with Cu substrate in the epitaxial growth of in-plane heterostructures can be excluded. Indeed, identical directions of graphene and h-BN at the interface were confirmed by STM[28] and TEM[27], which demonstrated laterally epitaxial growth of h-BN from graphene edges on Cu foil. Since the edge structure in heterostructures may affect their physical properties,[41] controlling this structure may be experimentally necessary in future.

The junction between two hybrid structures was frequently observed (Figure 6a), indicating that the interface of graphene and h-BN is vulnerable to fracture by thermal stress, which had further been verified by DFT calculations.[27] Therefore, the C reservoir introduced can be completely eliminated when the growth process is precisely controlled, where h-BN synthesized can inherit the intrinsic lattice orientation of graphene to form atomically a sharp graphene/h-BN interface. It has also been reported that the lateral heteroepitaxy of h-BN is used to form in-plane graphene/h-BN heterostructures, which are shown to exhibit an abrupt one-dimensional interface and the lattice orientation is solely determined by the graphene rather than supporting metal substrates.[28, 42] The selective growth of vertical or in-plane graphene/hBN heterostructures can be achieved through a temperature-triggered switching reaction or controlling the precursor concentrations and growth time, shown in Figure 6b-d.[42, 43]

More recently, theoretical calculations have suggested that the growth of C atoms from h-BN is energetically preferential at the vertices instead of the edges.[44] The formation energy and binding energy

of the N-terminated heterostructure are lower than that of the B-terminated one, resulting in the lower stability of this configuration, which is agreeable with the experimental results.[42] A subsequent study reveals that spin-polarized electronic states with half-metallic phase are identified when the graphene domain is terminated with zigzag edges, whereas a robust semiconducting behavior is confirmed with an armchair interface.[45] Based on the lateral structure of graphene and h-BN, a pronounced thermal rectification behavior is observed with heat current transport from h-BN to graphene, which can be qualitatively attributed to the resonance effect between out-of-plane phonon modes of the graphene and h-BN domain in the low frequency region.[46]

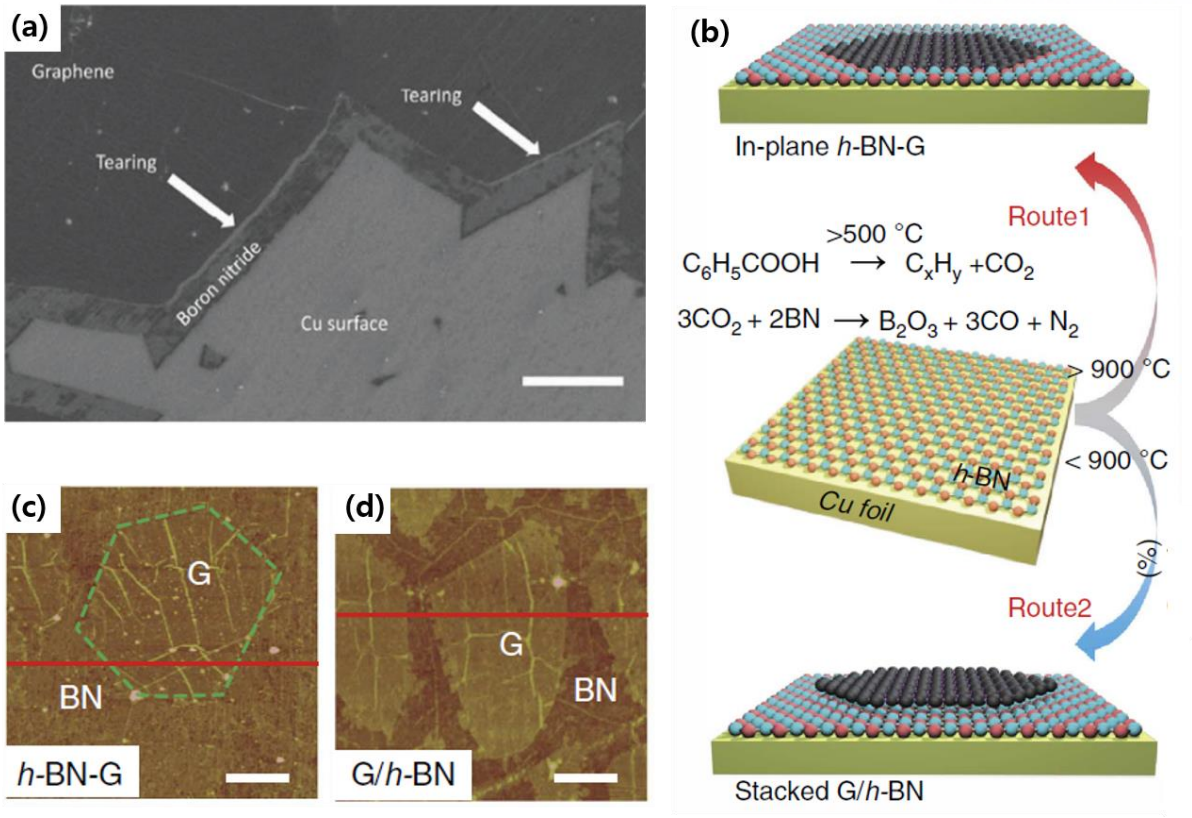

Figure 6. (a) Cooling-induced tearing of the interface between graphene and h-BN. (b) Schematic illustration of the temperature-triggered switching growth between in-plane h-BN-G and stacked G/h-BN heterostructures, defined as Route 1 and Route 2, respectively. (c,d) AFM height images of h-BN-G and G/h-BN after being transferred onto 300-nm-thick SiO_2/Si substrates

1.4 Reference

1. Novoselov, K. S.; Geim, A. K.; Morozov, S. V.; Jiang, D.; Zhang, Y.; Dubonos, S. V.; Grigorieva, I. V.; Firsov, A. A. Electric field effect in atomically thin carbon films. *Science* **2004**, *306*, 666–669.
2. Li, X. et al. Large-area synthesis of high-quality and uniform graphene films on copper foils. *Science* **2009**, *324*, 1312–1314.
3. Chen, J-H.; Jang, C.; Xiao, S.; Ishigami, M.; Fuhrer, M. S. Intrinsic and extrinsic performance limits of graphene devices on SiO_2. *Nat. Nanotechnol.* **2008**, *3*, 206–209.
4. Corso, M. et al. Boron nitride nanomesh. Science 303, 217–220 (2004).
5. Morscher, M.; Corso, M.; Greber, T.; Osterwalder, J. Formation of single layer h-BN on Pd (111). *Surf. Sci.* **2006**, *600*, 3280–3284.
6. Goriachko, A.; Knapp, M.; Over, H. Self-assembly of a hexagonal boron nitride nanomesh on Ru (0001). *Langmuir* **2007**, *23*, 2928–2931.
7. Kester, D. J.; Ailey, K. S.; Davis, R. F.; More, K. L. Phase evolution in boron-nitride thin-films. *J. Mater. Res.* **1993**, *8*, 1213–1216.
8. Nagashima, A.; Tejima, N.; Gamou, Y.; Kawai, T.; Oshima, C. Electronic dispersion relations of monolayer hexagonal boron nitride formed on the Ni (111) surface. *Phys. Rev. B* **1995**, *51*, 4606.
9. Rokuta, E.; Hasegawa, Y.; Suzuki, K.; Gamou, Y.; Oshima, C.; Nagashima, A. Phonon dispersion of an epitaxial monolayer film of hexagonal boron nitride on Ni (111). *Phys. Rev. Lett.* **1997**, *79*, 4609.
10. Levendorf, M. P.; Kim, C-J.; Brown, L.; Huang, P. Y.; Havener, R. W.; Muller, D. A.; Park, J. Graphene and boron nitride lateral heterostructures for atomically thin circuitry. *Nature* **2012**, *488*, 627–632.
11. Liu, Z. et al. In-plane heterostructures of graphene and hexagonal boron nitride with controlled domain sizes. *Nat. Nanotechnol.* **2013,** *8*, 119-124.
12. Bae, S. et al. Roll-to-roll production of 30-inch graphene films for transparent electrodes. *Nat. Nanotechnol.* **2010,** *5*, 574-578.
13. Li, J.; Shenoy, V. B. Graphene quantum dots embedded in hexagonal boron nitride sheets. *Appl. Phys. Lett.* **2011,** *98*, 013105.
14. Jun, S.; Li, X.; Meng, F.; Ciobanu, C. V. Elastic properties of edges in BN and SiC nanoribbons and of boundaries in C-BN superlattices: A density functional theory study. *Phys. Rev. B.* **2011,** *83*, 153407.
15. Ramasubramaniam, A.; Naveh, D. Carrier-induced antiferromagnet of graphene islands embedded in hexagonal boron nitride. *Phys. Rev. B.* **2011,** *84*, 075405.
16. Jiang, J.-W.; Wang, J.-S.; Wang, B.-S. Minimum thermal conductance in graphene and boron nitride superlattice. *Appl. Phys. Lett.* **2011,** *99*, 043109.

17. Wang, X.; Li, X.; Zhang, L.; Yoon, Y.; Weber, P. K.; Wang, H.; Guo, J.; Dai, H. N-doping of graphene through electrothermal reactions with ammonia. *Science* **2009,** *324*, 768-771.
18. Lherbier, A.; Blase, X.; Niquet, Y.-M.; Triozon, F.; Roche, S. Charge transport in chemically doped 2D graphene. *Phys. Rev. Lett.* **2008,** *101*, 036808.
19. Liu, A. Y.; Wentzcovitch, R. M.; Cohen, M. L. Atomic arrangement and electronic structure of BC_2N. *Phys. Rev. B.* **1989,** *39*, 1760-1765.
20. Ci, L.; Song, L.; Jin, C.; Jariwala, D.; Wu, D.; Li, Y.; Srivastava, A.; Wang, Z. F.; Storr, K.; Balicas, L.; Liu, F.; Ajayan, P. M. Atomic layers of hybridized boron nitride and graphene domains. *Nat. Mater.* **2010,** *9*, 430-435.
21. Gong, Y.; Shi, G.; Zhang, Z.; Zhou, W.; Jung, J.; Gao, W.; Ma, L.; Yang, Y.; Yang, S.; You, G.; Vajtai, R.; Xu, Q.; MacDonald, A. H.; Yakobson, B. I.; Lou, J.; Liu, Z.; Ajayan, P. M. Direct chemical conversion of graphene to boron-and nitrogen-and carbon-containing atomic layers. *Nat. Commun.* **2014,** *5*, 3193.
22. Sutter, P.; Cortes, R.; Lahiri, J.; Sutter, E. Interface formation in monolayer graphene-boron nitride heterostructures. *Nano Lett.* **2012,** *12*, 4869-4874.
23. Lu, J.; Zhang, K.; Liu, X. F.; Zhang, H.; Sum, T. C.; Neto, A. H. C.; Loh, K. P. Order–disorder transition in a two-dimensional boron–carbon–nitride alloy. *Nat. Commun.* **2013,** *4*, 2681.
24. Lu, P.; Zhang, Z.; Guo, W. Electronic Structures of BC_2N Nanoribbons. *J. Phys. Chem. C* **2011,** *115*, 3572-3577.
25. Girit, Ç. Ö.; Meyer, J. C.; Erni, R.; Rossell, M. D.; Kisielowski, C.; Yang, L.; Park, C.-H.; Crommie, M. F.; Cohen, M. L.; Louie, S. G.; Zettl, A. Graphene at the edge: stability and dynamics. *Science* **2009,** *323*, 1705-1708.
26. Gao, Y.; Zhang, Y.; Chen, P.; Li, Y.; Liu, M.; Gao, T.; Ma, D.; Chen, Y.; Cheng, Z.; Qiu, X.; Duan, W.; Liu, Z. Toward monolayer uniform hexagonal boron nitride–graphene patchworks with zigzag linking edges. *Nano Lett.* **2013,** *13*, 3439-3443.
27. Han, G. H.; Rodríguez-Manzo, J. A.; Lee, C.-W.; Kybert, N. J.; Lerner, M. B.; Qi, Z. J.; Dattoli, E. N.; Rappe, A. M.; Drndic, M.; Johnson, A. T. C. Continuous growth of hexagonal graphene and boron nitride in-plane heterostructures by atmospheric pressure chemical vapor deposition. *ACS Nano* **2013,** *7*, 10129-10138.
28. Liu, L.; Park, J.; Siegel, D. A.; McCarty, K. F.; Clark, K. W.; Deng, W.; Basile, L.; Idrobo, J. C.; Li, A.-P.; Gu, G. Heteroepitaxial growth of two-dimensional hexagonal boron nitride templated by graphene edges. *Science* **2014,** *343*, 163-167.
29. Yu, Q.; Jauregui, L. A.; Wu, W.; Colby, R.; Tian, J.; Su, Z.; Cao, H.; Liu, Z.; Pandey, D.; Wei, D.; Chung, T. F.; Peng, P.; Guisinger, N. P.; Stach, E. A.; Bao, J.; Pei, S.-S.; Chen, Y. P. Control and

characterization of individual grains and grain boundaries in graphene grown by chemical vapour deposition. *Nat. Mater.* **2011,** *10*, 443-449.

30. Vlassiouk, I.; Regmi, M.; Fulvio, P.; Dai, S.; Datskos, P.; Eres, G.; Smirnov, S. Role of hydrogen in chemical vapor deposition growth of large single-crystal graphene. *ACS Nano* **2011,** *5*, 6069-6076.
31. Sutter, P.; Huang, Y.; Sutter, E. Nanoscale integration of two-dimensional materials by lateral heteroepitaxy. *Nano Lett.* **2014**, *14*, 4846-4851.
32. Zhang, Y.; Gao, T.; Gao, Y.; Xie, S.; Ji, Q.; Yan, K.; Peng, H.; Liu, Z. Defect-like structures of graphene on copper foils for strain relief investigated by high-resolution scanning tunneling microscopy. *ACS Nano* **2011,** *5*, 4014-4022.
33. Balog, R.; Jorgensen, B.; Nilsson, L.; Andersen, M.; Rienks, E.; Bianchi, M.; Fanetti, M.; Laegsgaard, E.; Baraldi, A.; Lizzit, S.; Sljivancanin, Z.; Besenbacher, F.; Hammer, B.; Pedersen, T. G.; Hofmann, P.; Hornekaer, L. Bandgap opening in graphene induced by patterned hydrogen adsorption. *Nat. Mater.* **2010,** *9*, 315-319.
34. Nozaki, H.; Itoh, S. Lattice dynamics of BC_2N. *Phys. Rev. B.* **1996,** *53*, 14161-14170.
35. Batzill, M. The surface science of graphene: Metal interfaces, CVD synthesis, nanoribbons, chemical modifications, and defects. *Surf. Sci. Rep.* **2012,** *67*, 83-115.
36. Brugger, T.; Günther, S.; Wang, B.; Dil, J. H.; Bocquet, M.-L.; Osterwalder, J.; Wintterlin, J.; Greber, T. Comparison of electronic structure and template function of monolayer graphene and a hexagonal boron nitride nanomesh on Ru (0001) *Phys. Rev. B.* **2009,** *79*, 045407.
37. Wang, B.; Caffio, M.; Bromley, C.; Früchtl, H.; Schaub, R. Coupling epitaxy, chemical bonding, and work function at the local scale in transition metal-supported graphene. *ACS Nano* **2010,** *4*, 5773-5782.
38. Sutter, P.; Lahiri, J.; Albrecht, P.; Sutter, E. Chemical vapor deposition and etching of high-quality monolayer hexagonal boron nitride films. *ACS Nano* **2011,** *5*, 7303-7309.
39. Preobrajenski, A. B.; Nesterov, M. A.; Ng, M. L.; Vinogradov, A. S.; Mårtensson, N. Monolayer h-BN on lattice-mismatched metal surfaces: On the formation of the nanomesh. *Chem. Phys. Lett.* **2007,** *446*, 119-123.
40. Laskowski, R.; Blaha, P.; Gallauner, T.; Schwarz, K. Monolayer model of the hexagonal boron nitride nanomesh on the Rh (111) surface. *Phys. Rev. Lett.* **2007,** *98*, 106802.
41. Liu, Y.; Bhowmick, S.; Yakobson, B. I. BN white graphene with “colorful” edges: The energies and morphology. *Nano Lett.* **2011,** *11*, 3113-3116.

42. Gao, T.; Song, X.; Du, H.; Nie, Y.; Chen, Y.; Ji, Q.; Sun, J.; Yang, Y.; Zhang, Y.; Liu, Z. Temperature-triggered chemical switching growth of in-plane and vertically stacked graphene-boron nitride heterostructures. *Nat. Commun.* **2015**, *6*, 6835

43. Kim, S. M.; Hsu, A.; Araujo, P. T.; Lee, Y.-H.; Palacios, T.; Dresselhaus, M.; Idrobo, J.-C.; Kim, K. K.; Kong, J. Synthesis of patched or stacked graphene and hBN flakes: a route to hybrid structure discovery. *Nano Lett.* **2013**, *13*, 933-941.

44. Loh, G. C.; Pandey, R. A graphene–boron nitride lateral heterostructure – a first-principles study of its growth, electronic properties, and chemical topology. *J. Mater. Chem. C* **2015**, *3*, 5918–5932.

45. Zhang, D.; Zhang, D.-B.; Yang, F.; Lin, H.-Q.; Xu H.; Chang, K. Interface engineering of electronic properties of graphene/boron nitride lateral heterostructures. *2D Mater.* **2015**, *2*, 041001.

46. Chen, X.-K.; Xie, Z.-X.; Zhou, W.-X.; Tang L.-M.; Chen, K.-Q. Thermal rectification and negative differential thermal resistance behaviors in graphene/hexagonal boron nitride heterojunction. *Carbon* **2016**, *100*, 492–500.

Chapter 2: Growth of Monolayer Hexagonal Boron Nitride on Platinum Using Chemical Vapor Deposition

2.1 Abstract

Hexagonal boron nitride (h-BN) is gaining significant attention as a two-dimensional dielectric material, along with graphene and other such materials. Herein, we demonstrate the growth of highly crystalline, monolayer h-BN on Pt foil through a low-pressure chemical vapor deposition method that allowed h-BN to be grown over a wide area (8×25 mm^2). An electrochemical bubbling-based method was used to transfer the grown h-BN layer from the Pt foil onto an arbitrary substrate. This allowed the Pt foil, which was not consumed during the process, to be recycled repeatedly. The UV-visible absorption spectrum of the monolayer h-BN suggested an optical band gap of 6.06 eV, while a high-resolution transmission electron microscopy image of the same showed the presence of distinct hexagonal arrays of B and N atoms, which were indicative of the highly crystalline nature and single-atom thickness of the h-BN layer. This method of growing monolayer h-BN over large areas was also compatible with use of a sapphire substrate.

2.2 Introduction

Hexagonal boron nitride (h-BN), which has a two-dimensional (2D) strong sp^2 covalent bond-containing honeycomb structure that is similar to that of graphene,[1-3] has attracted much attention because of its high mechanical strength and thermal conductivity.[4-6] However, graphene exhibits semimetallic properties and has a zero-band gap, while h-BN is an insulator with a direct band gap of 5–6 eV. This is attributable to the partially ionic character of the B-N bonds.[7-11] In addition, in contrast to graphene, h-BN is known to be chemically stable in air at temperatures as high as 1000 °C.[12,13] Highly purified h-BN exhibits intense excitonic luminescence bands for wavelengths ranging from 215 to 227 nm, which are sufficiently strong to cause stimulated emission. Therefore, high-quality h-BN is a promising material for deep UV optoelectronic devices.[14]

Monolayer h-BN has been grown on single-crystal transition metals such as Au(111), Ru(001), Rh(111), and Pt(111) in ultrahigh vacuum (UHV) chemical vapor deposition (CVD) systems by introducing a borazine precursor.[15-19] However, it is extremely difficult to grow and characterize

monolayer h-BN and to transfer it onto other substrates, owing to the complex nature of the UHV CVD systems used. Along with the recent progress made in research on graphene, attempts have also been made to grow h-BN on Cu and Ni foils using atmospheric pressure CVD (APCVD) or low-pressure CVD (LPCVD) methods and then transfer it onto other substrates via widely used etching processes.[20-25] During these growth processes, h-BN has been known to exhibit different behaviors, depending on the precursor used. Borazine as a precursor induced growth of h-BN in multilayer form, with the layers being between 5 and 50 nm in thickness.[20,21] On the other hand, the use of a mixture of ammonia and diborane as the precursor suggested that the thickness of the grown h-BN layers could be controlled by changing the growth temperature and period; however, it was hard to obtain uniform single layers of h-BN because the growth rate during the process was high.[22] The growth rate of h-BN can be decreased by using a powdered precursor such as ammonia borane. Indeed, it was reported that by using ammonia borane as the precursor, it was possible to grow monolayer h-BN on Cu foil within 40 min, with multiple layers being formed on some sites. It was also noticed that the density of these multiple layers increased with an increase in the growth period.[23]

Herein, we report the growth of a high-quality monolayer h-BN over a large area via a simple LPCVD method. This growth was achieved by employing Pt foil and ammonia borane as the substrate and precursor, respectively. The single layer of h-BN grown on Pt foil could be successfully transferred onto an arbitrary substrate via an electrochemical bubbling-based method. This method of transferring h-BN has numerous advantages: it is rapid, allows for the recycling of the Pt foil, and does not result in Pt residues. High-resolution transmission electron microscopy (HRTEM) images showed clearly that the layer of h-BN comprised hexagonal arrays of B and N atoms, indicating the highly crystalline and monolayer nature of the grown h-BN.

2.3 Experimental Section

2.3.1 Growth of Monolayer h-BN Using CVD Methods

The monolayer h-BN was prepared by a LPCVD method. Figure 1 shows a schematic of the LPCVD system used for growing monolayer h-BN. Platinum foil (99.95 % purity, 0.125 mm thick, Goodfellow) was placed at the middle of a 2 inch quartz tube CVD system and ammonia borane (97 % purity, Sigma-Aldrich) was placed at a sub-chamber. The furnace was heated to 1100 ^{o}C in flow of a hydrogen gas (10 sccm), and the sub-chamber was heated to 130 ^{o}C for the decomposition of ammonia borane. The Pt foil was pre-annealed at 1100 ^{o}C for 30 min in flow of H_2 gas to remove some impurity. The growth of h-BN on Pt foil was initiated by opening a valve of the sub-chamber. During the growth, the pressure was maintained at 0.1 Torr. After finishing the growth, the furnace was quickly cooled down to room temperature under H_2 gas condition.

2.3.2 Electrochemical Bubbling Method for Transferring h-BN onto Target Substrate

Pt foil is an expensive and chemically inert material. Thus, the commonly used etching-based transfer method for Cu and Ni substrates is not suitable for the transfer of the h-BN layer grown on Pt foil. We were able to use this bubbling-based transfer method to successfully transfer the h-BN layer grown on Pt foil onto arbitrary substrates in a manner that allowed the Pt foil to be recycled. Figure 2 shows a schematic of the bubbling-based transfer method, which is based on the electrolysis of water. The front side of the h-BN film on the Pt foil was covered with PMMA. The Pt foil was immersed in an aqueous solution of 1 M NaOH for an electrochemical delamination. The PMMA/h-BN/Pt foil and a bare Pt foil were utilized as a cathode and an anode, respectively. The bubbling transfer was performed under a constant current of 1 A (corresponding electrolytic voltage of 5 - 12 V) for 1 - 5 min. The application of a constant current for a few minutes caused the PMMA/h-BN layer to detach from the Pt foil because of the formation of H_2 bubbles. The bubbling process could usually be completed in less than 5 min, a duration much smaller than that of the etching process using an etchant with Cu and Ni foils. Furthermore, the transferred h-BN layer was free of metal residues, which is an advantage of this transfer process. After peeling off the PMMA/h-BN film from the Pt foil, it was rinsed with deionized water in order to remove residual NaOH solution. Then, it was transferred into a SiO_2(300 nm)/Si substrate, and finally was dipped into acetone to remove PMMA. It should be noted that the Pt foil used in the growth of h-BN was recyclable since Pt was not consumed during the process.

2.3.3 Characterization of Monolayer h-BN

The surface morphology of the single layer h-BN was characterized by optical microscope (Axio Scope.A1, Carl Zeiss), scanning electron microscope (S-4800, Hitachi), and atomic force microscope (Dimension 3100, Veeco). Raman spectra were measured using a micro Raman spectrometer (Alpha 300s, WITec GmbH) with a 532 nm laser. UV-visible absorption spectrum (Cary 5000 UV-Vis-NIR, Agilent) was measured to estimate the optical band gap of monolayer h-BN transferred into a quartz substrate. X-ray photoelectron spectra (K-Alpha, Thermo Fisher) were measured to identify boron and nitrogen atoms of h-BN. Low voltage Cs aberration-corrected transmission electron microscopy (Titan Cube G2 60-300, FEI), which was operated at 80 kV with monochromated electron beam, was used for ultra-high-resolution imaging of the h-BN along with selected area electron diffraction (SAED) pattern and electron energy loss spectroscopy (EELS).

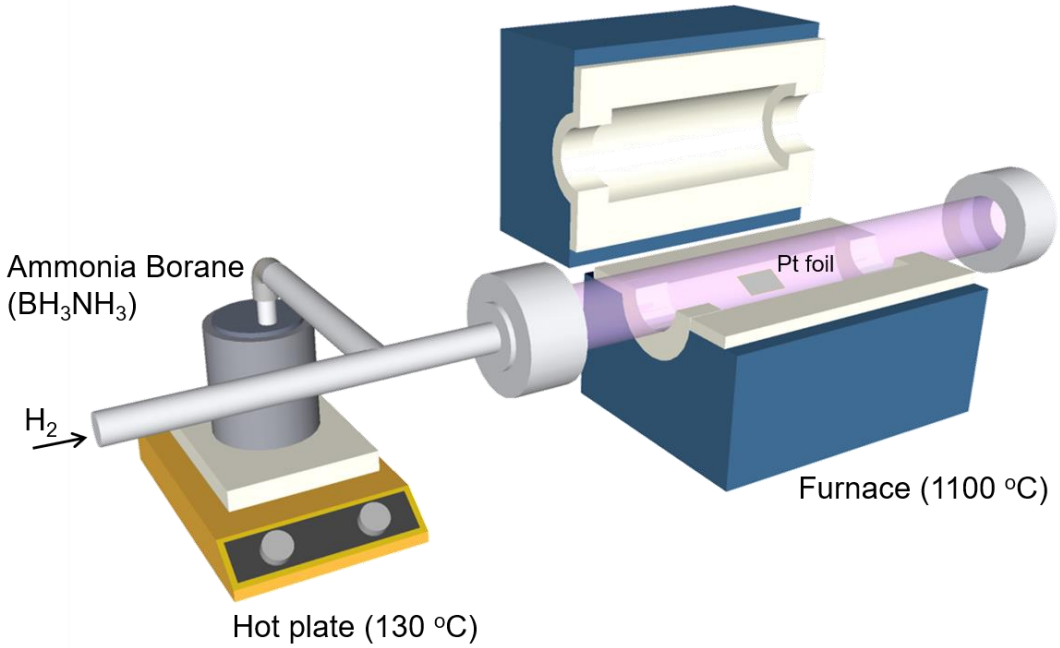

Figure 1. Schematic diagrams of the LPCVD system used for h-BN growth.

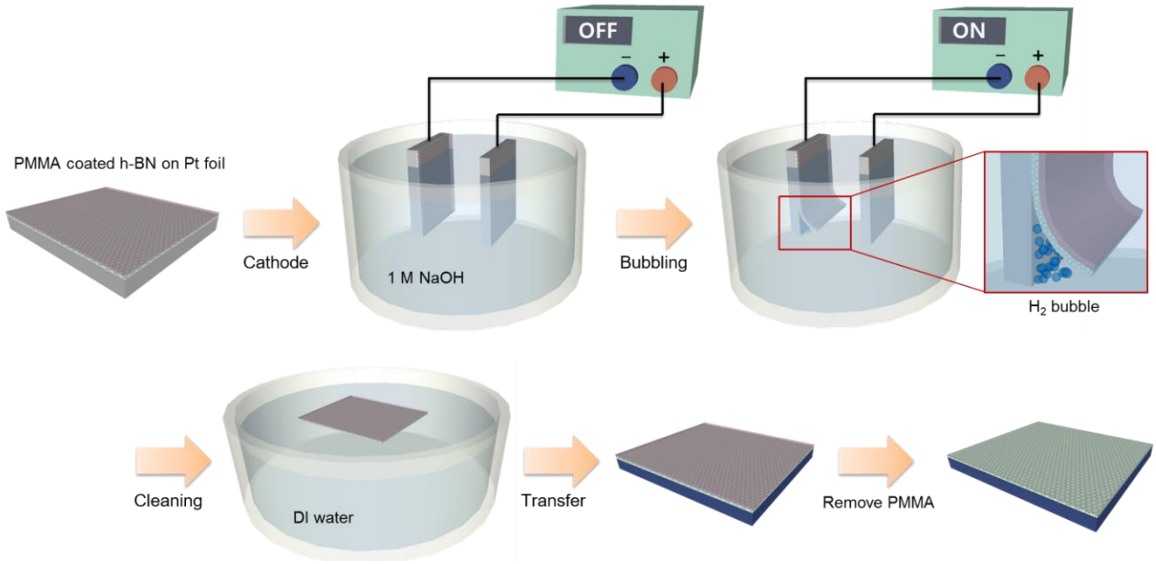

Figure 2. Scheme of electrochemical bubbling-based method used to transfer the h-BN layer.

2.4 Results and Discussion

2.4.1 Growth Mechanism of Monolayer h-BN on Pt Substrate

Figure 1 shows a schematic of the LPCVD system used for growing monolayer h-BN. Ammonia borane (NH_3-BH_3) was used as the precursor because it is stable under ambient conditions. Borazine is moisture sensitive and can be hydrolyzed to boric acid, ammonia, and hydrogen.[26] To grow monolayer h-BN on Pt foil, the temperature within the LPCVD system was set to 1100 °C, and the precursor, ammonia borane, was heated to 130 °C, since it decomposes into hydrogen, polyiminoborane (BHNH; solid), and borazine ($(HBNH)_3$; gas) at this temperature.[27,28] The produced borazine gas was made to diffuse from the source bottle into the furnace, where it was adsorbed onto the Pt foil. Monolayer h-BN was thus formed from borazine via thermal decomposition as shown in Figure 3. Because of the weak bonding of the borazine molecules with the grown h-BN layer at the growth temperature, any precursor molecules that were adsorbed onto the grown layer were rapidly desorbed back into the gas phase.[18,19] The growing h-BN film essentially constituted an inert blanket that progressively covered an increasingly larger fraction of the Pt foil surface during the growth process, resulting in the eventual self-termination of the growth of the layer, with it being one atom thick. Thus, uniform, monolayer h-BN could be grown on Pt foil without multiples layers being formed, regardless of the duration of the growth process.

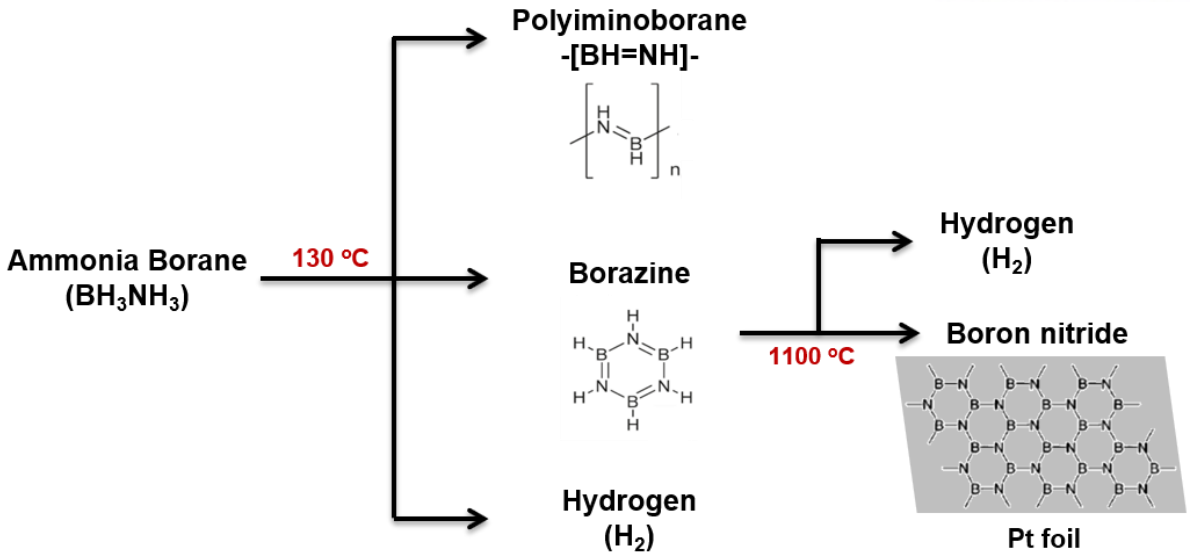

Figure 3. Thermal decomposition of ammonia borane, forming borazine gas in the high temperature.

2.4.2 Characterization of Monolayer h-BN

It is hard to observe monolayer h-BN on a SiO_2(300 nm)/Si substrate using an optical microscope under a white light source because its optical contrast is less than 1.5%.[31] Figure 4(a) shows an optical image of monolayer h-BN under a white light source. The h-BN region is barely distinguishable without residues at its edges. The contrast of a layer of h-BN on a SiO_2(300 nm)/Si substrate changes with the wavelength of the incident light.[31] BN is darker than the substrate at wavelengths longer than ~530 nm and brighter at shorter ones, with the optical contrast of monolayer h-BN on a SiO_2(300 nm)/Si substrate being the highest at 590 nm. Monolayer h-BN could be noticed more clearly under a light source with a 630 nm band-pass filter than was the case under a white-light source alone. Figure 4(b) shows an optical microscopy image of monolayer h-BN under a light source with a 630 nm band-pass filter. (See Figure 5 for the differences in the optical contrasts of h-BN under white-light sources with 425, 520, and 630 nm band-pass filters). In contrast to optical microscopy, scanning electron microscopy (SEM) allowed us to easily identify an h-BN layer on a SiO_2/Si substrate (Figure 4(c)). The thickness of an h-BN layer transferred onto a SiO_2/Si substrate could be determined using atomic force microscopy (AFM). Figure 6(a) shows an AFM image of a layer of h-BN transferred onto a SiO_2/Si substrate, with the thickness of the layer, which was less than 0.48 nm, indicated in the image. This value was consistent with that reported previously for monolayer h-BN.[23] Note that the thicknesses of the h-BN layers grown on Pt foil using different growth periods (1 min to 30 min) were all less than 0.48 nm, indicating that only monolayer h-BN was grown in all the cases (See Figure 7).

Figure 6(b) shows the Raman spectrum of h-BN on a SiO_2/Si substrate, obtained using a 532 nm laser. A characteristic Raman peak of bulk, single-crystal h-BN was observed at 1366 cm^{-1} and was attributable to the E_{2g} phonon mode.[31,32] This peak shifts to ~1370 cm^{-1} in the case of monolayer h-BN and to ~1364 cm^{-1} for bilayer h-BN.[31] In our study, the E_{2g} phonon mode for all h-BN layers grown using the various growth periods appeared at 1372 cm^{-1}, indicating that all the h-BN layers grown were monolayers (See Figure 8). The results of Raman spectroscopy were consistent with the AFM results.

The UV-visible absorption spectrum of monolayer h-BN was determined, with the h-BN film exhibiting almost zero absorbance in the visible-light range and abrupt absorption in the UV region. This suggested the presence of an optical band gap (OBG), which was calculated using the formula for a direct band semiconductor[7] and determined to be 6.06 eV, as shown in Figure 6(d). The optical band gap energy was determined by the formula of a direct band gap semiconductor; $\alpha = C(E - E_g)^{1/2}/E$ (where α is the absorption coefficient, C is a constant, E is the photon energy and E_g is the optical bandgap energy). The plot of $(\alpha E)^2$ as a function of E should be a straight line. Therefore, when

$(\alpha E)^2 = 0$, the E value should be equal to E_g. This value was consistent with that predicted by theoretical calculations (6.0 eV).[33] X-ray photoemission spectroscopy (XPS) was performed on the as-grown single layer of h-BN to check for the presence of the elements B and N and to determine their elemental ratios. The binding energies for the B 1s and N 1s peaks, determined from the XPS spectra, were 190.38 (Figure 6(e)) and 397.88 eV (Figure 6(f)), respectively. These values matched with those previously reported for h-BN.[20,22] The ratio of B and N atomic % in monolayer h-BN, calculated from the XPS results, was 1:1.03.

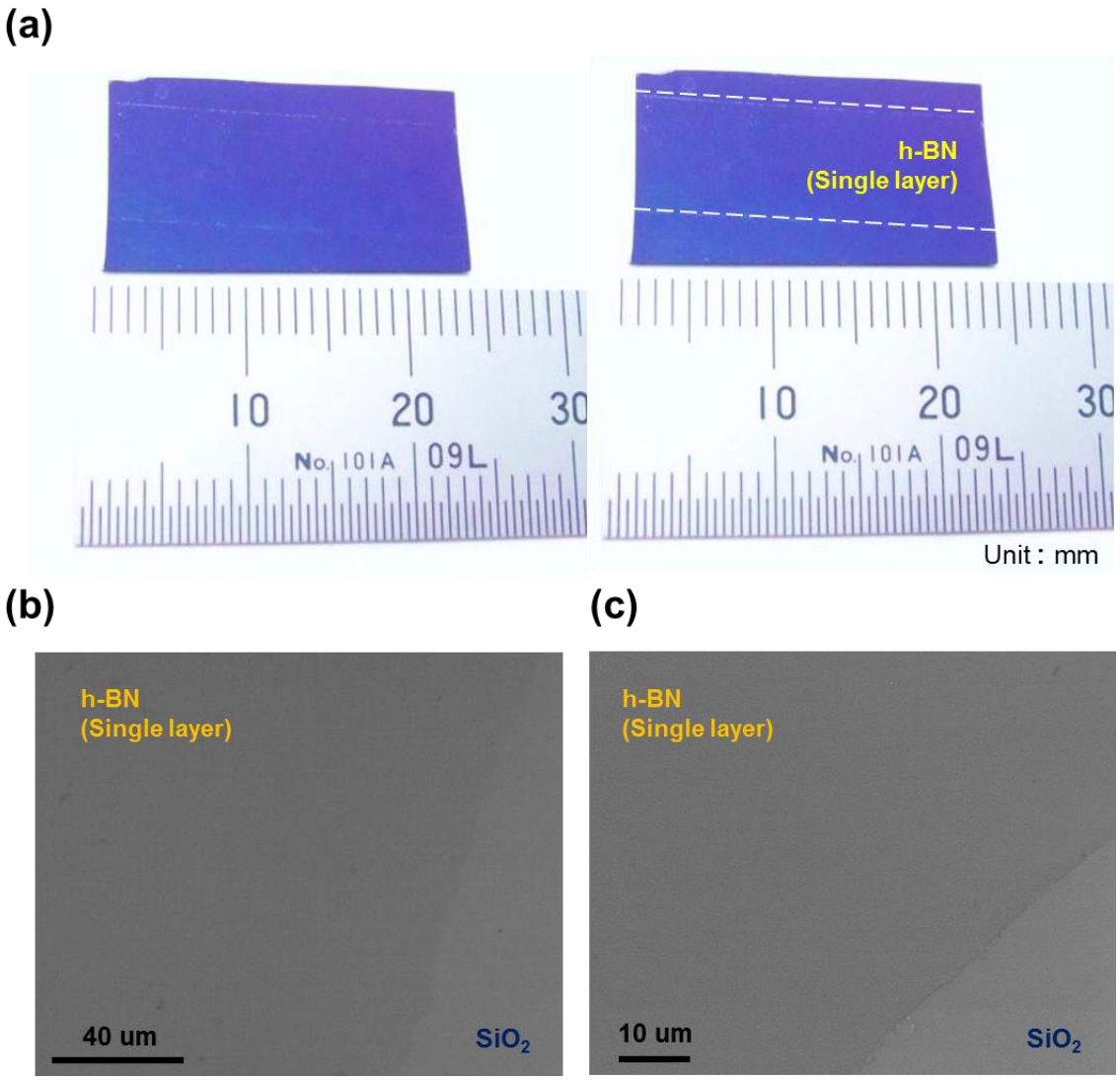

Figure 4. (a) Photograph of an h-BN layer transferred from Pt foil to a SiO_2/Si substrate. (b) Optical microscopy image of monolayer h-BN on a SiO_2/Si substrate, taken using 630 nm band-pass-filtered light. (c) SEM image of monolayer h-BN on a SiO_2/Si substrate.

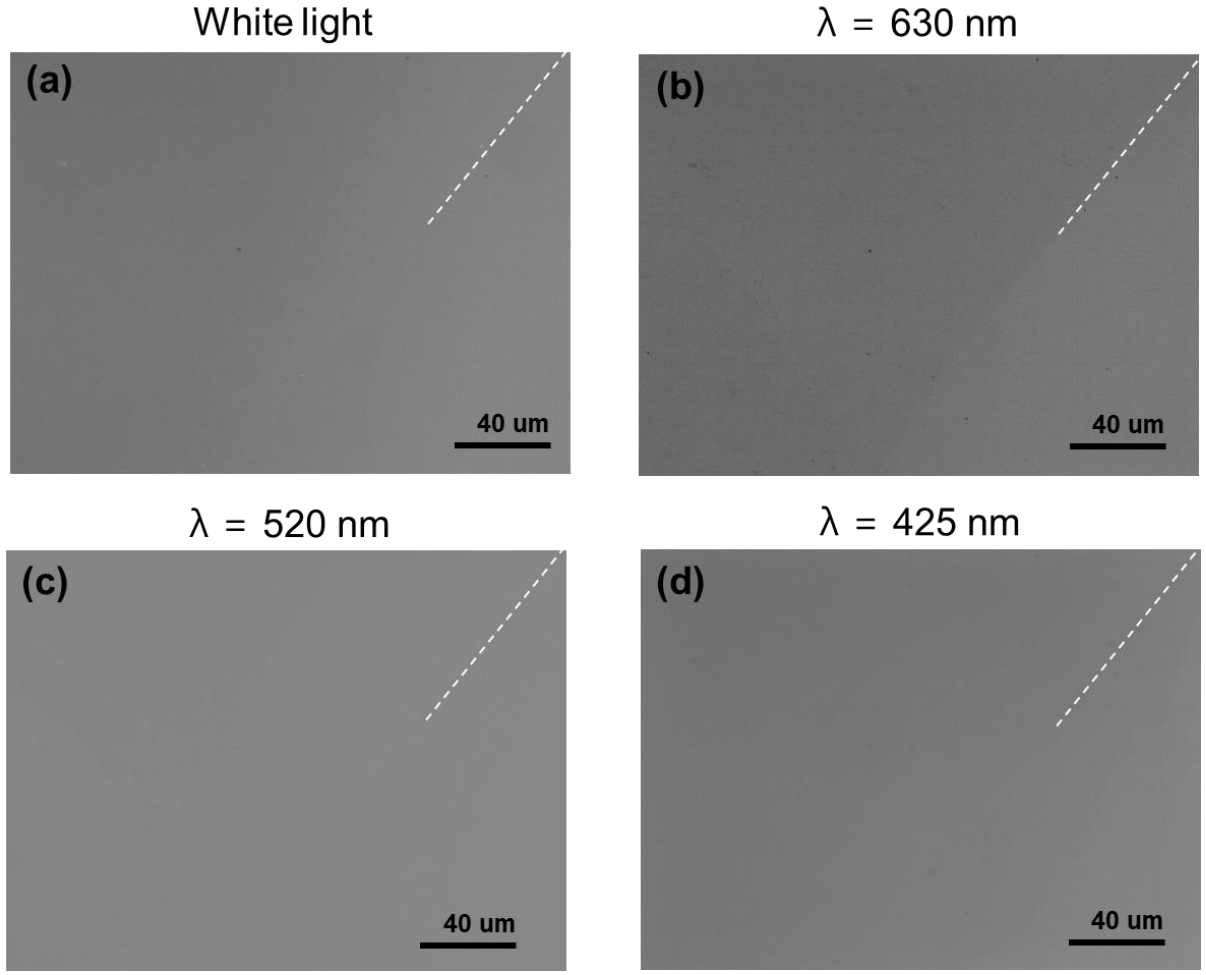

Figure 5. Optical microscope images for monolayer h-BN on top of Si substrate with a 300 nm thermal oxide layer under various light wavelengths: (a) white light, (b) 630 nm, (c) 520nm, and (d) 425 nm band-pass filtered light.

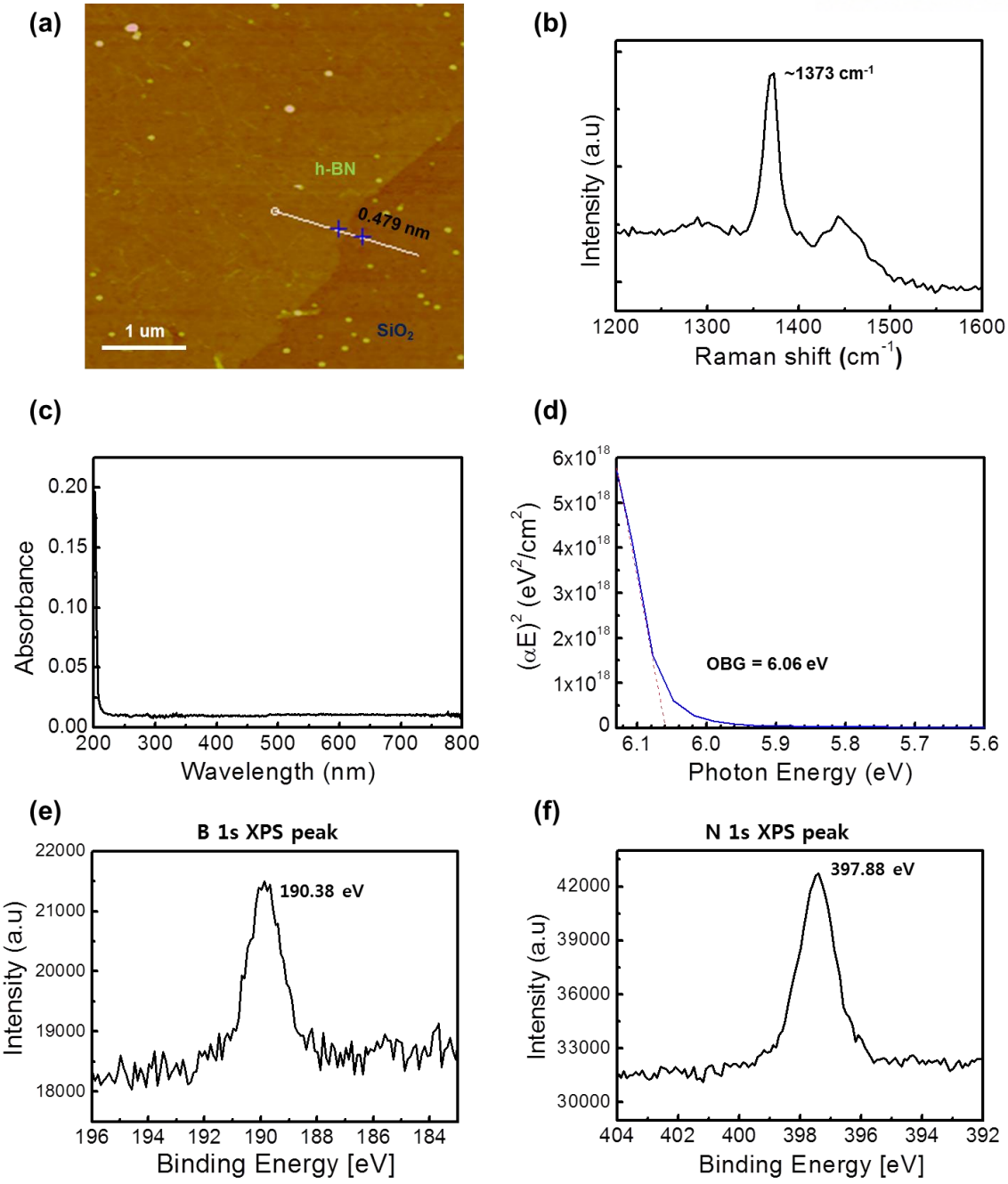

Figure 6. (a) AFM image of monolayer h-BN on a SiO_2/Si substrate; (b) Raman spectrum of monolayer h-BN on a SiO_2/Si substrate; (c) UV-visible absorption spectrum and (d) optical band gap analysis of monolayer h-BN on a quartz substrate. XPS spectra of h-BN on Pt foil: (e) B1s spectrum and (f) N1s spectrum.

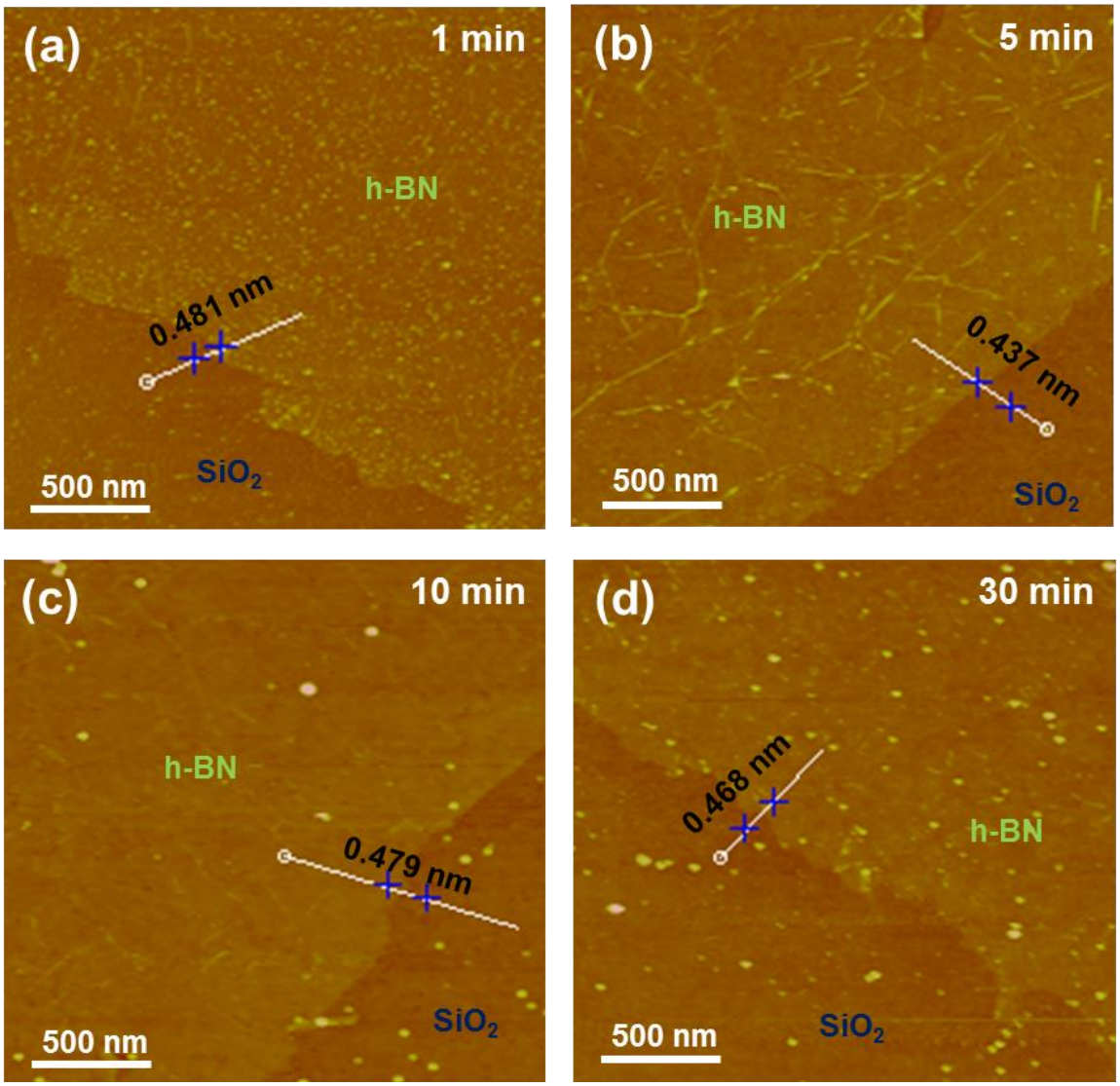

Figure 7. AFM images of h-BN transferred onto SiO_2/Si substrate after it was grown on Pt foil at different growth period: (a) 1 min, (b) 5 min, (c) 10 min, and (d) 30 min.

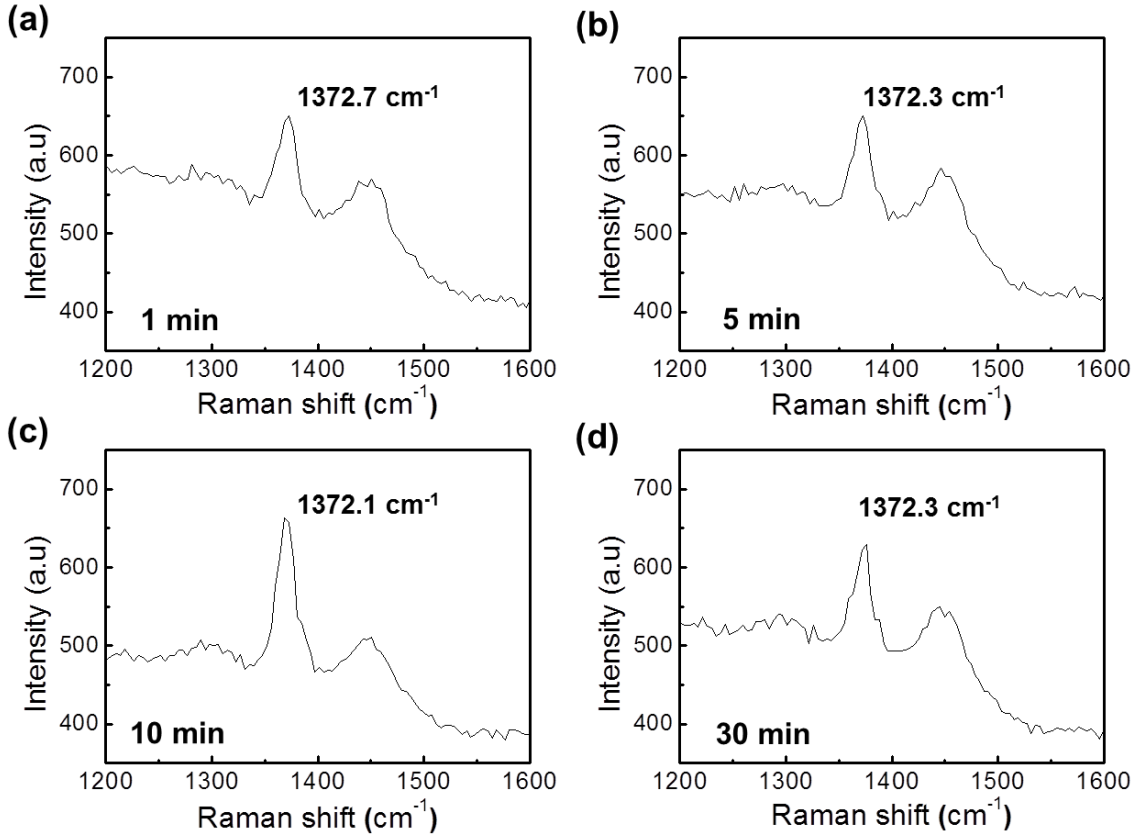

Figure 8. Raman spectra of h-BN transferred onto SiO_2/Si substrate after it was grown on Pt foil at different growth period: (a) 1 min, (b) 5 min, (c) 10 min, and (d) 30 min.

2.4.3 Transmission Electron Microscopy measurement of monolayer h-BN

Figure 9(a) shows a low-magnification bright-field (BF) TEM image of the freestanding h-BN film after it was transferred onto a hole with 2 μm in diameter in Au quantifoil TEM grid. The h-BN film covered the entire mesh well without broken regions and ripples. The selective area electron diffraction (SAED) pattern in Figure 9(b) clearly indicates a set of hexagonal diffraction spots matched well with the $(10\bar{1}0)$ index of monolayer h-BN. To directly observe the atomic structure of monolayer h-BN, we used a Cs aberration-corrected electron microscopy operated at 80 kV. We matched boron and nitrogen atom sites in the h-BN lattice, as illustrated in Figure 9(c), since boron vacancies are firstly generated at 80 keV, followed by the removal of the neighboring nitrogen atoms that surrounded the point defects, owing to the difference in the knock-on damage thresholds of the boron (74 keV) and nitrogen (84 keV) atoms in a BN sheet. The HRTEM image in Figure 10 was used for identifying the B and N atoms by the presence of a single boron vacancy and an expanded large triangular defect. Electron energy loss spectroscopy (EELS) was qualitatively carried out for elemental analysis of the h-BN film. Figure 9(d) represents an EELS spectrum with two visible edges corresponding to the characteristic K-shell ionization edges of B and N, respectively.[34, 35] In addition, the characteristic π^* and σ^* energy loss peaks at the boron K edge prove that h-BN has sp^2 hybridization bonds. Furthermore, it was found from dark-field TEM images that the grain size of h-BN reaches to a few micrometer range (see Figure 11 and 12). Details on the grain size and grain boundaries of h-BN are under study.

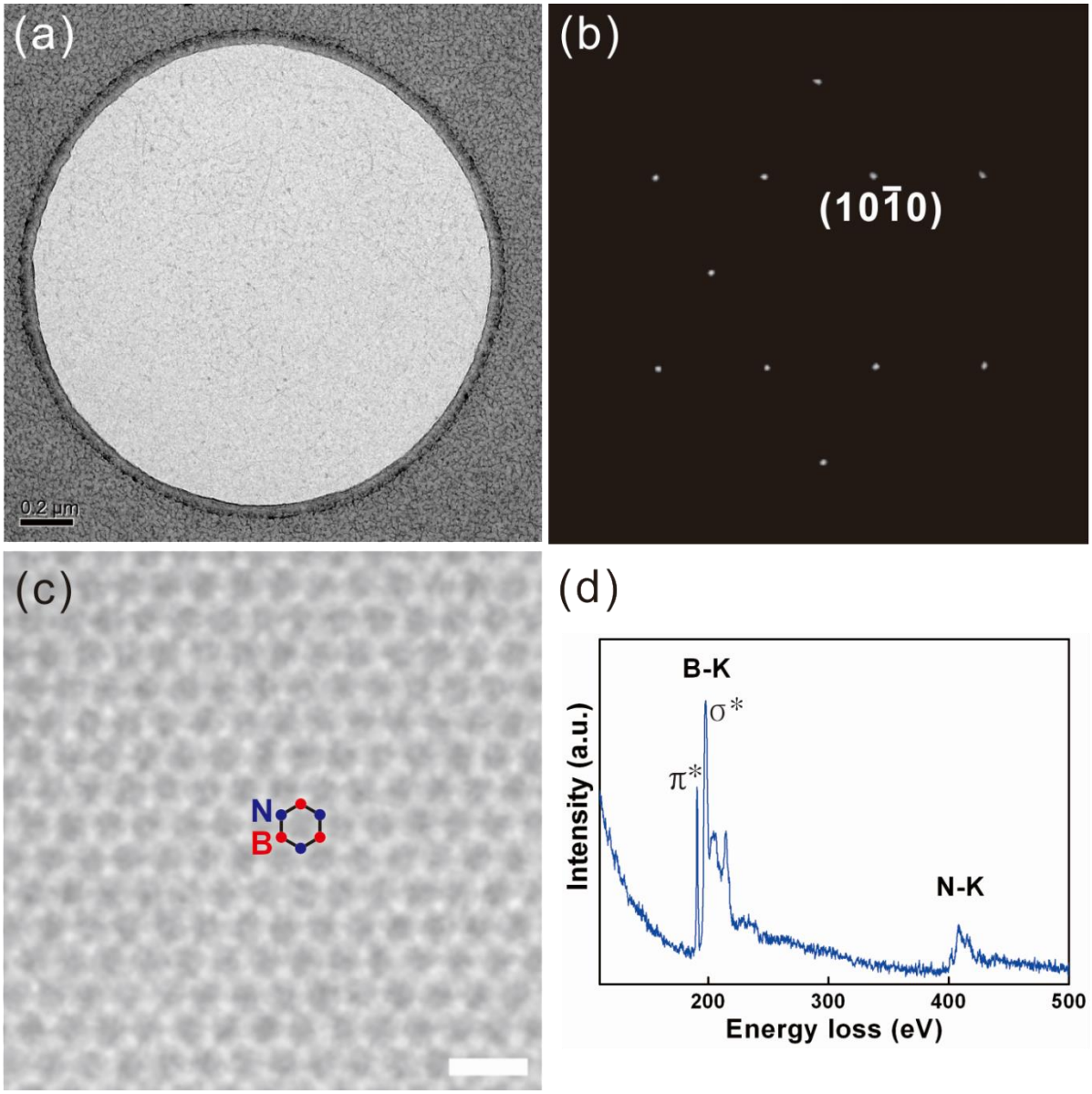

Figure 9. (a) A low-magnification TEM image of monolayer h-BN. (b) The corresponding diffraction pattern of monolayer h-BN showing a set of hexagonal patterns from single layer h-BN. (c) Atomic-resolution TEM image of monolayer h-BN (scale bar: 1 nm). (d) EELS spectrum of monolayer h-BN.

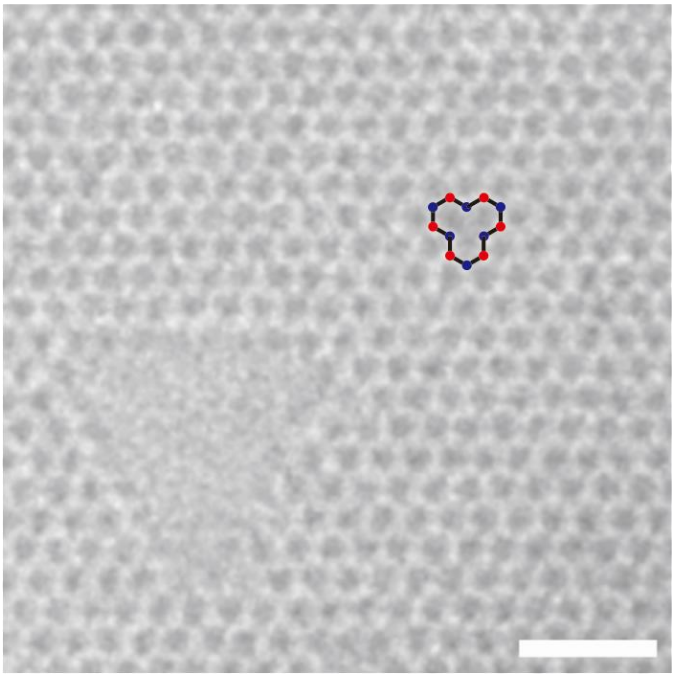

Figure 10. Atomic-resolution TEM image of h-BN. A triangular defect of single boron vacancy in single layer h-BN is indicated. Red and blue dots represent B and N, respectively. (Scale bar: 1 nm)

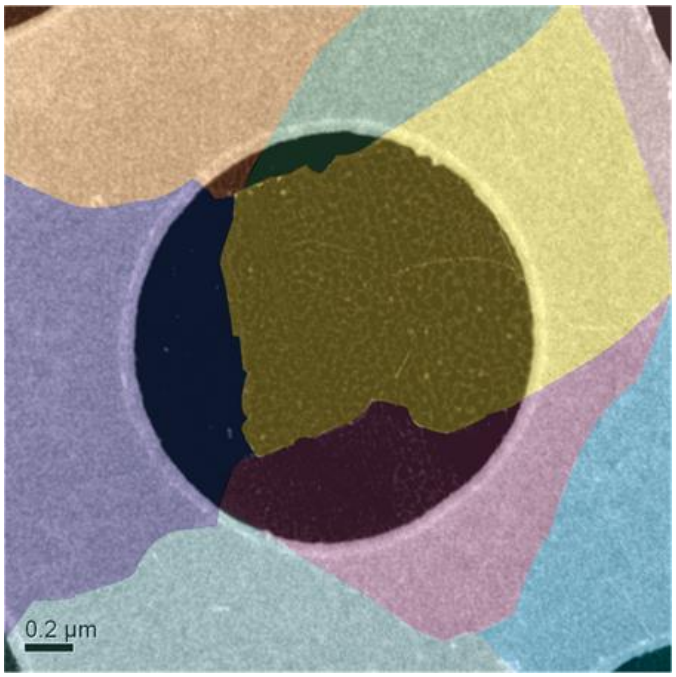

Figure 11. Monolayer h-BN grain mapping image with an over-laid background of the dark-field TEM image.

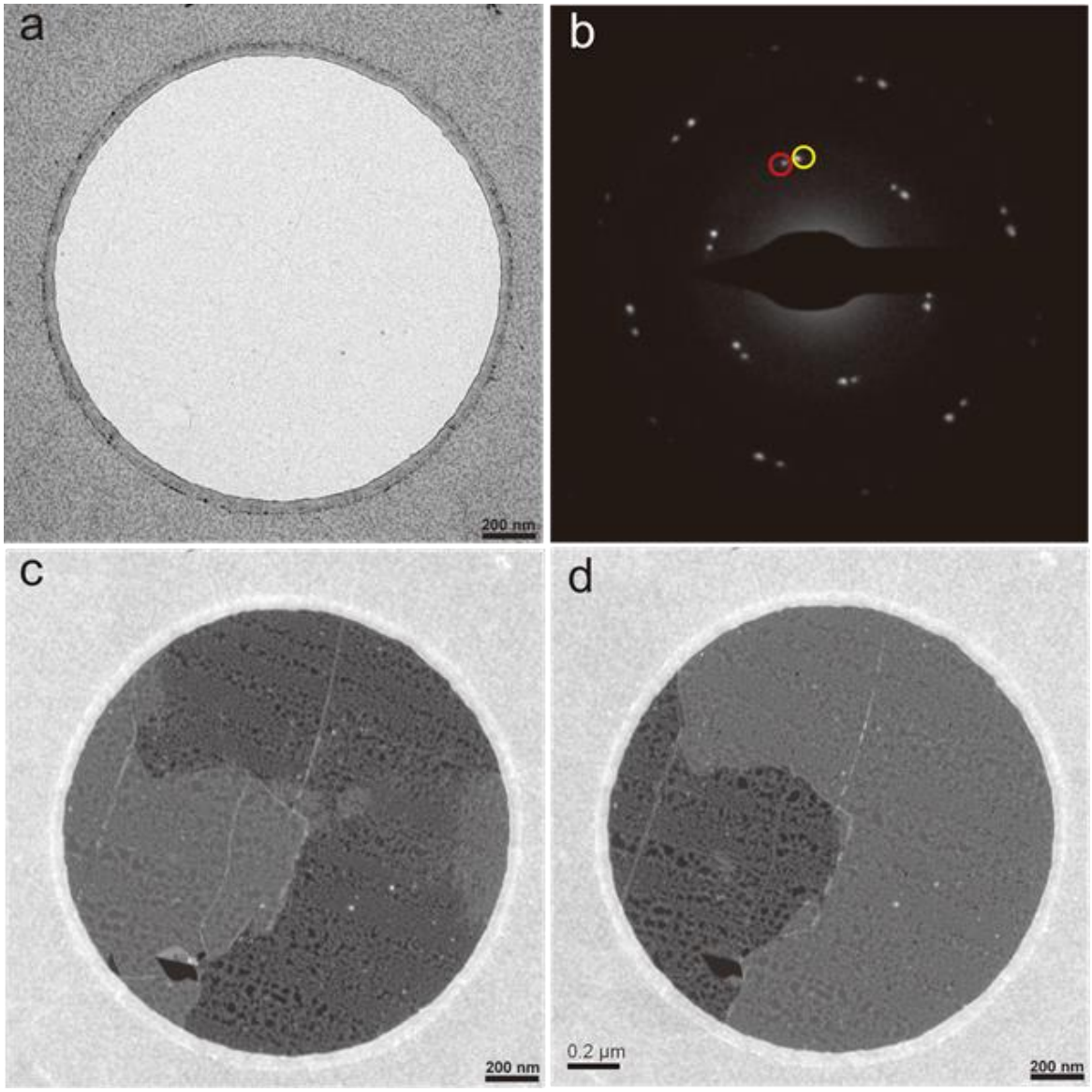

Figure 12. (a) Bright-field TEM (BFTEM) image of monolayer h-BN. (b) The corresponding diffraction pattern of monolayer h-BN. (c) Dark-field TEM (DFTEM) image taken from the diffraction spot marked with the red circle in (b). (d) DFTEM image taken from the diffraction spot marked with the yellow circle in (b).

2.4.4 Electrical Characteristics and Recyclable growth of Monolayer h-BN

The quality of the h-BN layer was estimated on the basis of its resistance. It was previously reported that current can flow through the layer if the carbon is doped into h-BN.[36,37] The electrical characteristics of the h-BN layer were determined using the four-point probe technique. Figure 13(a) shows an optical image of the four devices fabricated on a single layer of h-BN, with the channel length and width being 1 um and 5 um, respectively. The I-V curve in Figure 13(b) shows that no current flowed through the devices. The I-V curves of the other devices were same as that in Figure 13(b). Thus, it was determined that the h-BN layer exhibited excellent insulating properties, which were indicative of its high quality.

As can be seen from Figure 14, there was no change in the quality of the h-BN layers grown even when the Pt foil was recycled and used to grow monolayer h-BN 100 times. This showed that the Pt foil could be used repeatedly as previously mentioned. Therefore, in contrast to Cu and Ni foils, Pt foil has numerous advantages. It allows for the synthesis of highly crystalline, monolayer h-BN with sufficient reproducibility while being recyclable. In addition, the formed single layer of h-BN could be transferred through a rapid bubbling-based method.

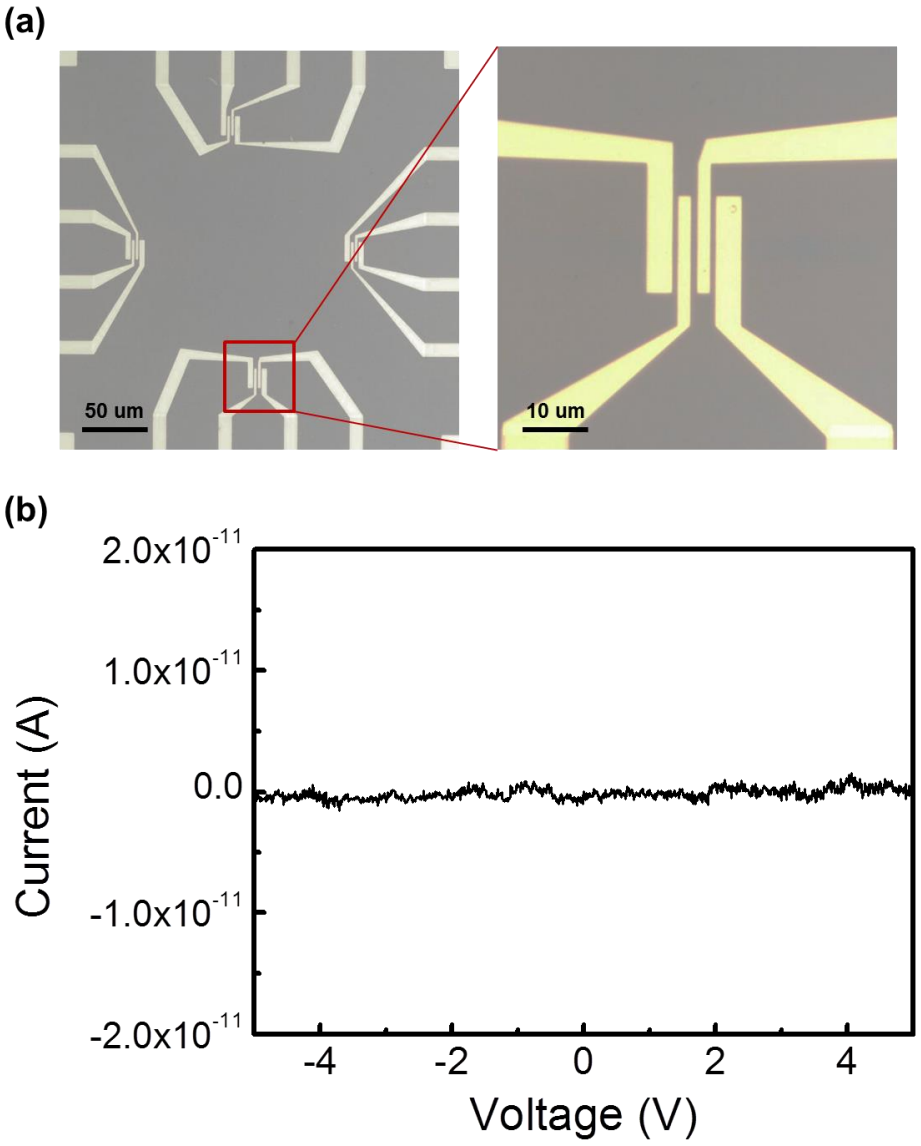

Figure 13. (a) Optical microscopy image of the four devices fabricated on monolayer h-BN for the four-point probe technique. (b) I-V curve of one of the monolayer h-BN devices, indicating the highly insulating nature of monolayer h-BN.

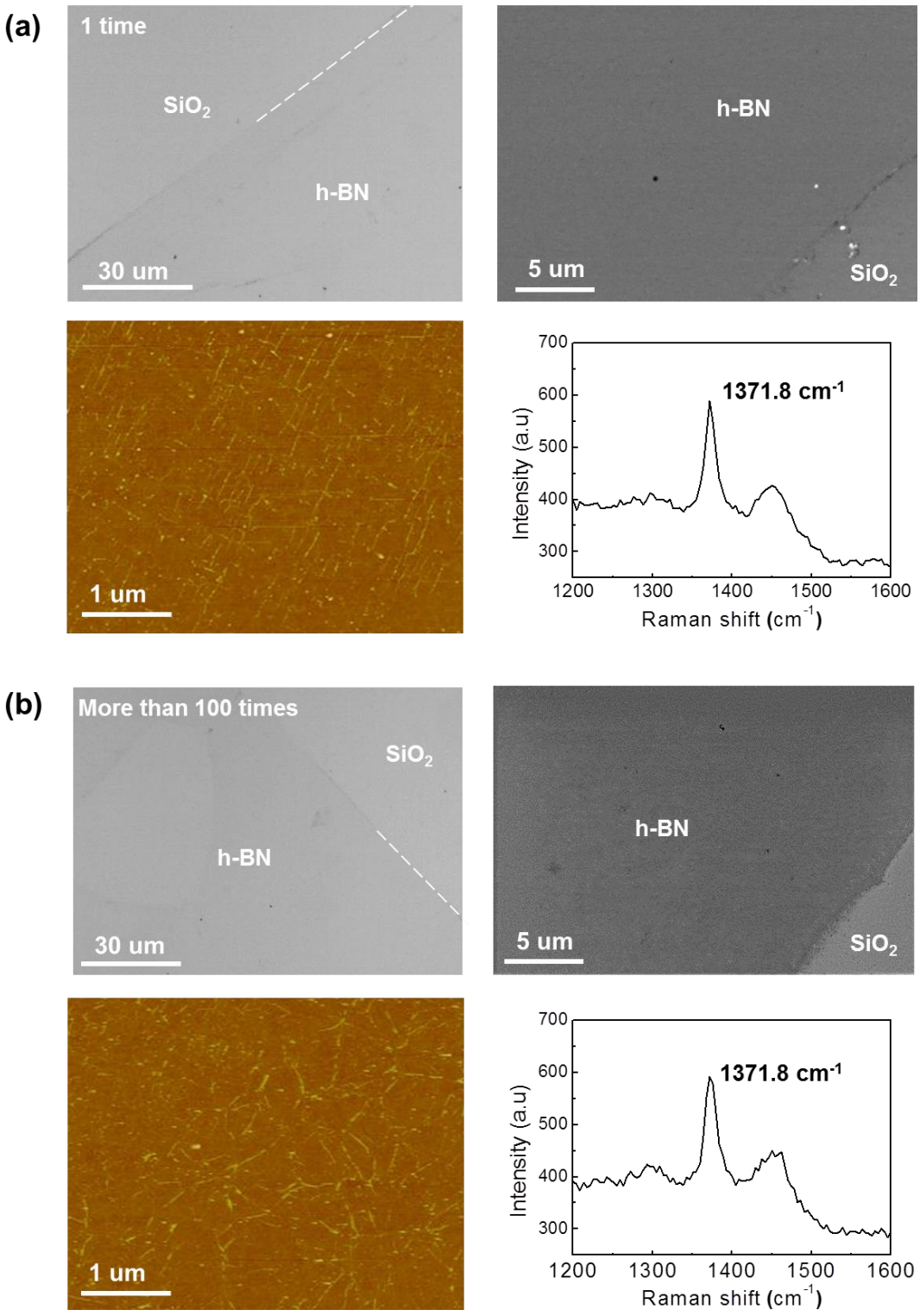

Figure 14. OM, SEM, and AFM images and Raman spectrum of monolayer h-BN grown on fresh Pt foil (a) and 100 times recycled Pt foil (b).

2.5 Conclusion

In summary, we were able to synthesize high-quality, monolayer h-BN on Pt foil over a large area using an LPCVD method. The h-BN film grown on Pt foil could be transferred onto a SiO_2/Si substrate by using the electrochemical bubbling-based method. The Pt foil could be used repeatedly, with the quality of the grown h-BN layers remaining unchanged even after 100 growth cycles. More importantly, the HRTEM results showed clearly the presence of hexagonal arrays of B and N atoms, indicating that the h-BN layer was highly crystalline and single-atom thick. The UV-visible absorption spectrum of monolayer h-BN revealed an optical band gap of 6.06 eV. The h-BN film also exhibited excellent insulating properties, suggesting that it can be used as a dielectric layer. This method provides a wide range of advantages in that it allows for the synthesis of highly crystalline, monolayer h-BN with sufficient reproducibility, with the Pt foil used during the process being recyclable. Further, the grown h-BN film could be transferred to other substrates through the rapid bubbling-based transfer method.

2.6 Reference

1. Corso, M.; Auwarter, W.; Muntwiler, M.; Tamai, A.; Greber, T.; Osterwalder, J. Boron nitride nanomesh. *Science* **2004**, *303*, 217-220.
2. Paine, R. T.; Narula, C. K. Synthetic routes to boron nitride. *Chem. Rev.* **1990**, *90*, 73-91.
3. Lee, C.; Li, Q.; Kalb, W.; Liu, X.-Z.; Berger, H.; Carpick, R. W.; Hone, J. Frictional characteristics of atomically thin sheets. *Science* **2010**, *328*, 76-80.
4. Zhi, C.; Bando, Y.; Tang, C.; Kuwahara, H.; Golberg, D. Large-scale fabrication of boron nitride nanosheets and their utilization in polymeric composites with improved thermal and mechanical properties. *Adv. Mater.* **2009**, *21*, 2889-2893.
5. Lipp, A.; Schwerz, K. A.; Hunold, K. Hexagonal boron nitride: fabrication, properties and applications. *J. Eur. Ceram. Soc.* **1989**, *5*, 3-9.
6. Sevik, C.; Kinaci, A.; Haskins, J. B.; Cagin, T. Influence of disorder on thermal transport properties of boron nitride nanostructures. *Phys. Rev. B* **2012**, *86*, 075403.
7. Yuzuriha, T. H.; Hess, D. W. Structural and optical properties of plasma-deposited boron nitride films. *Thin Solid Films* **1986**, *140*, 199-207.
8. Zunger, A.; Katzir, A.; Halperin, A. Optical properties of hexagonal boron nitride. *Phys. Rev. B* **1976**, *13*, 5560-5573.
9. Watanabe, K.; Taniguchi, T.; Kanda, H. Direct-bandgap properties and evidence for ultraviolet lasing of hexagonal boron nitride single crystal. *Nat. Mater.* **2004**, *3*, 404-409.
10. Golberg, D.; Bando, Y.; Huang, Y.; Terao, T.; Mitome, M.; Tang, Ch.; Zhi, C. Boron nitride nanotubes and nanosheets. *ACS Nano* **2010**, *4*, 2979-2993.
11. Pacile, D.; Meyer, J. C.; Girit, C. O.; Zettl, A. The two-dimensional phase of boron nitride: Few-atomic-layer sheets and suspended membranes. *Appl. Phys. Lett.* **2008**, *92*, 133107.
12. Motojima, S.; Tamura, Y.; Sugiyama, K. Low temperature deposition of hexagonal BN films by chemical vapour deposition. *Thin Solid Films* **1982**, *88*, 269-274.
13. Hao, X. P.; Cui, D. L.; Shi, G. X.; Yin, Y. Q.; Xu, X. G.; Jiang, M. H.; Xu, X. W.; Li, Y. P. Low temperature benzene thermal synthesis and characterization of boron nitride nanocrystals. *Mater. Lett.* **2001**, *51*, 509-513.
14. Watanabe, K.; Taniguchi, T.; Niiyama, T.; Miya, K.; Taniguchi, M. Far-ultraviolet plane-emission handheld device based on hexagonal boron nitride. *Nat. Photonics* **2009**, *3*, 591-594.
15. Simonson, R.J.; Paffett, M. T.; Jones, M.E.; Koel, B. E. A vibrational study of borazine adsorbed on Pt (111) and Au (111) surfaces. *Surf. Sci.* **1991**, *254*, 29-44.
16. Nagashima, A.; Tejima, N.; Gamou, Y.; Kawai, T. Electronic structure of monolayer hexagonal boron nitride physisorbed on metal surfaces. *Phys. Rev. Lett.* **1995**, *75*, 3918-3921.

17. Preobrajenski, A. B.; Vinogradov, A. S.; Ng, M. L.; Cavar, E.; Westerstrom, R.; Mikkelsen, A.; Lundgren, E.; Martensson, N. Influence of chemical interaction at the lattice-mismatched h-BN/Rh (111) and h-BN/Pt (111) interfaces on the overlayer morphology *Phys. Rev. B* **2007**, *75*, 245412.
18. Paffett, M. T.; Simonson, R. J.; Papin, P.; Paine, R. T. Borazine adsorption and decomposition at Pt (111) and Ru (001) surfaces. *Surf. Sci.* **1990**, *232*, 286-296.
19. Sutter, P.; Lahiri, J.; Albrecht, P.; Sutter, E. Chemical vapor deposition and etching of high-quality monolayer hexagonal boron nitride films. *ACS Nano* **2011**, *5*, 7303-7309.
20. Shi, Y.; Hamsen, C.; Jia, X.; Kim, K. K.; Reina, A.; Hofmann, M.; Allen, L. H.; Zhang, K.; Li, H.; Juang, Z.-Y.; Dresselhaus, M. S.; Li, L.-J.; Kong, J. Synthesis of few-layer hexagonal boron nitride thin film by chemical vapor deposition. *Nano. Lett.* **2010**, *10*, 4134-4139.
21. Kim, K. K.; Hsu, A; Jia, X.; Kim, S. M.; Shi, Y.; Dresselhaus, M.; Palacios, T.; Kong, J. Synthesis and characterization of hexagonal boron nitride film as a dielectric layer for graphene devices. *ACS Nano* **2012**, *6*, 8583-8590.
22. Ismach, A.; Chou, H.; Ferrer, D. A.; Wu, Y.; Mcdonnell, S.; Floresca, H. C.; Covacevich, A.; Pope C.; Piner, R.; Kim, M. J.; Wallace, R. M.; Colombo, L.; Ruoff, R. S. Toward the controlled synthesis of hexagonal boron nitride films. *ACS Nano* **2012**, *6*, 6378-6385.
23. Kim, K. K.; Hsu, A.; Jia, X.; Kim, S. M.; Shi, Y.; Hofmann, M.; Nezich, D.; Rodriguez-Nieva, J. F.; Dresselhaus, M.; Palacios, T.; Kong, J. Synthesis of monolayer hexagonal boron nitride on Cu foil using chemical vapor deposition. *Nano Lett.* **2012**, *12*, 161-166.
24. Song, L.; Ci, L.; Lu, H.; Sorokin, P. B.; Jin, C.; Ni, J.; Kvashnin, A. G;.; Kvashnin, D. G.; Lou, J.; Yakobson, B. I.; Ajayan, P. M. Large scale growth and characterization of atomic hexagonal boron nitride layers. *Nano Lett.* **2010**, *10*, 3209-3215.
25. Lee, K. H.; Shin, H.-J.; Lee, J.; Lee, I.-Y.; Kim, G.-H.; Choi, J.-Y, Kim, S.-W. Large-scale synthesis of high-quality hexagonal boron nitride nanosheets for large-area graphene electronics. *Nano Lett.* **2012**, *12*, 714-718.
26. Wolf, G.; Baumann, J.; Baitalow, F.; Hoffmann, F. P. Calorimetric process monitoring of thermal decomposition of B–N–H compounds. *Thermochim. Acta* **2000**, *343*, 19-25.
27. Baitalow, F.; Baumann, J.; Wolf, G.; Jaenicke-Robler, K.; Leitner, G. Thermal decomposition of B–N–H compounds investigated by using combined thermoanalytical methods. *Thermochim. Acta* **2002**, *391*, 159-168.
28. Frueh, S.; Kellett, R.; Mallery, C.; Molter, T.; Willis, W. S.; King'ondu, C.; Suib, S. L. Pyrolytic decomposition of ammonia borane to boron nitride *Inorg. Chem.* **2011**, *50*, 783-792.

29. Wang, Y.; Zheng, Y.; Xu, X.; Dubuisson, E.; Bao, Q.; Lu, J.; Loh, K. P. Electrochemical delamination of CVD-grown graphene film: toward the recyclable use of copper catalyst. *ACS Nano* **2011**, *5*, 9927-9933.
30. Gao, L.; Ren, W.; Xu, H.; Jin, L.; Wang, Z.; Ma, T.; Ma, L.-P.; Zhang, Z.; Fu, Q.; Peng, L.-M.; Bao, X.; Cheng, H.-M. Repeated growth and bubbling transfer of graphene with millimetre-size single-crystal grains using platinum. *Nat. Commun.* **2012**, *3*, 699.
31. Gorvachev, R. V.; Riaz, I.; Nair, R. R.; Jalil, R.; Britnell, L.; Belle, B. D.; Hill, E. W.; Novoselov, K. S.; Watanabe, K.; Taniguchi, T.; Geim, A. K.; Blake, T. Hunting for monolayer boron nitride: optical and Raman signatures. *Small* **2011**, *7*, 465-468.
32. Arenal, R.; Ferrari, A. C.; Reich, S.; Wirtz, L.; Mevellec, J.-Y.; Lefrant, S.; Rubio, A.; Loiseau, A. Raman spectroscopy of single-wall boron nitride nanotubes. *Nano Lett.* **2006**, *6*, 1821-1816.
33. Blasé, X.; Rubio, A.; Louie, S. G.; Cohen, M. L. *Phys. Rev. B* **1995**, *51*, 6868-6875.
34. Mayer, J. C.; Chuvilin, A.; Algara-Siller, G.; Biskupek, J.; Kaiser, U. Quasiparticle band structure of bulk hexagonal boron nitride and related systems. *Nano Lett.* **2009**, *9*, 2683-2689.
35. Chopra, N. G.; Luyken, R. J.; Cherrey, K.; Crespi, V. H.; Cohen, M. L.; Louie, S. G.; Zettl, A. Boron nitride nanotubes. *Science* **1995**, *269*, 966-967.
36. Ci, L.; Song, L.; Jin, C.; Jariwala, D.; Wu, D.; Li, Y.; Srivastava, A.; Wang, Z. F.; Storr, K.; Balicas, L.; Liu, Feng.; Ajayan, P. M. Atomic layers of hybridized boron nitride and graphene domains. *Nat. Mater.* **2010**, *9*, 430-435.
37. Wang, X.; Zhi, C.; Li, L.; Zeng, H.; Li, C.; Mitome, M.; Goldberg, D.; Bando, Y. "Chemical Blowing" of Thin-Walled Bubbles: High-Throughput Fabrication of Large-Area, Few-Layered BN and Cx-BN Nanosheets. *Adv. Mater.* **2011**, *23*, 4072-7076.

Chapter 3: Catalytic Conversion of Hexagonal Boron Nitride to Graphene on Platinum for In-Plane Heterostructure

3.1 Abstract

Heterostructures of hexagonal boron nitride (h-BN) and graphene have attracted a great deal of attention for potential applications in 2D materials. While several methods have been developed to produce this material through the partial substitution reaction of graphene, the reverse reaction has not been reported. While the endothermic nature of this reaction might account for the difficulty and previous absence of such a process, we report herein a new chemical route in which the Pt substrate plays a catalytic role. We propose that this reaction proceeds through h-BN hydrogenation; subsequent graphene growth quickly replaces the initially etched region. Importantly, this conversion reaction enables the controlled formation of patterned in-plane graphene/h-BN heterostructures, without needing the commonly employed protecting mask, simply by using a patterned Pt substrate.

3.2 Introduction

Recent advances in the synthesis of graphene[1-2] and hexagonal boron nitride (h-BN)[3-4] have enabled the large-scale growth of their monolayers. Although graphene and h-BN have similar atomic arrangements and a negligible difference of about 2% between their lattice constants, their electronic structures are completely different; graphene is a zero band gap semiconductor, while h-BN is an insulator with a large band gap of 5.9 eV.[5] Because of the structural similarities between the two, it is expected that they can form a seamless interface when combined as a hybrid,[6-10] leading to precisely controlled electronic[11-13] and magnetic[14] properties through proper interface control. In-plane or lateral graphene/h-BN heterostructures have been successfully realized through heteroepitaxial (or sequential) growth[6-10] and patterned regrowth[15-17] methods. Several attempts have been made to develop a patterned substitution reaction to directly convert graphene to either h-BN or boron carbonitride (h-BNC).[18] This process of converting carbon materials to boron nitride structures, though novel to graphene,[9, 19] is being used since the 1990s. For example, boron nitride nanotubes can be synthesized by effecting a substitution reaction on their carbon analogs;[20-21] boron nitride sheets have been similarly synthesized from multiple carbon sources such as biomaterials and pulps.[22] However, to the best of our knowledge, the structurally- controlled in-plane heterostructure by the reverse reaction of substituting h-BN to

graphene has never been reported. Herein, we report on the first such technique by using h-BN on a Pt catalyst to form an in-plane graphene/h-BN heterostructure. We further elucidate the reaction mechanism using systematic control experiments. Furthermore, we develop a novel process for the formation of a patterned heterostructure through a spatially controlled conversion that does not utilize a protecting mask.

3.3 Experimental Section

3.3.1 Conversion Reaction of h-BN to Graphene on Pt metal Substrate

Single layers of h-BN were synthesized on Pt foil using ammonia borane as a CVD precursor. The precise experimental details can be found in our previous report.[3] The resulting complex was then loaded into the center of a vacuum quartz tube placed in a furnace. The tube was pumped down to 0.21 torr with pure argon gas (50 sccm), and then heated to 1000 °C at a steady rate for over 40 min. The reaction was initiated with a flow of methane gas (5 sccm) and argon (50 sccm); complete conversion was obtained after 20 min.

3.3.2 Transfer Method of the Heterostructure onto Target Substrate

The produced films were transferred from Pt to SiO_2/Si substrate using electrochemical delamination. First, poly(methyl methacrylate) (PMMA) was spin coated on the film/Pt foil. The resulting structure was then dipped into a 1 M aqueous solution of NaOH and used as a cathode; a piece of bare Pt foil was included as an anode. The application of a constant current for 1-5 min caused the formation of H_2 bubbles, effectively detaching the PMMA/film layer from the Pt. The PMMA/film layer was then washed with deionized water and transferred onto the target substrate, after which PMMA was removed with acetone.

For delaminating graphene from Pt substrate and h-BN from SiO_2 simultaneously, we used the electrochemical delamination using HF as electrolyte. First, PMMA was spin coated on the film/Pt-SiO_2 substrate. The resulting structure was then dipped into a solution of HF. The application of a constant current caused the formation of H_2 bubbles on the Pt surface. At the same time, SiO_2 under h-BN films can be etched by HF solution. The detached PMMA/film layer was then washed with deionized water and transferred onto the target substrate, after which PMMA was removed with acetone.

3.3.3 Characterization of the Heterostructure

The surface morphology of the samples was characterized by optical microscopy (Axio Scope.A1, Carl Zeiss), SEM (S-4800, Hitachi), and AFM (Dimension 3100, Veeco). Raman spectra were measured using a micro Raman spectrometer (Alpha 300s, WITec) equipped with a 532 nm laser. X-ray photoelectron spectra (K-Alpha, Thermo Fisher) were measured to identify h-BN boron and nitrogen atoms and graphene carbon atoms. Low-voltage aberration-corrected TEM (Titan Cube G2 60-300, FEI) was applied at 80 kV with a monochromated electron beam and combined with EELS in order to obtain ultra-high-resolution imaging of the h-BN and graphene surfaces. The surface potential of the samples was measured by Kelvin probe force microscopy (XE-70, PSIA) using a dual pass scanning probe technique in tapping mode. A SPECS JT-STM system was used for STM characterizations.

3.4 Results and Discussion

3.4.1 Catalytic Effect of Pt Metal Substrate for Conversion Reaction of h-BN to Graphene

To better understand the inherent difficulty of converting BN to carbon, we compared the thermodynamics of both the graphene to h-BN conversion and the reverse reaction using the standard enthalpy of reaction (ΔH_R), which can be easily calculated by Hess's law.[23]

$$B_3N_3H_6 + 6\ C\ (graphene) + 9\ H_2 \rightarrow 3\ BN\ (h\text{-}BN) + 6\ CH_4\ (\Delta H_R = -670.95\ kJ/mol) \quad (1)$$

$$BN\ (h\text{-}BN) + 3\ CH_4 \rightarrow 3\ C\ (graphene) + 2\ BH_3 + 2NH_3\ (\Delta H_R = 810.63\ kJ/mol) \quad (2)$$

Equation (1) was derived from experimental data produced by Lu et al.,[19] in which borazine was used as a source and methane was formed. In equation (2), methane was used as the carbon precursor, while borane and ammonia were produced. Overall, the conversion of h-BN is endothermic, while that of graphene is exothermic. Therefore, h-BN conversion to graphene requires a significant amount of energy to overcome the activation barrier, as shown in Figure 1. This explains why no reaction occurred when an h-BN sheet on a SiO_2/Si substrate was heated to 1000 °C under methane (Figure 2), even though it is known that graphene on a Si substrate under boric acid and ammonia does undergo conversion.[18]

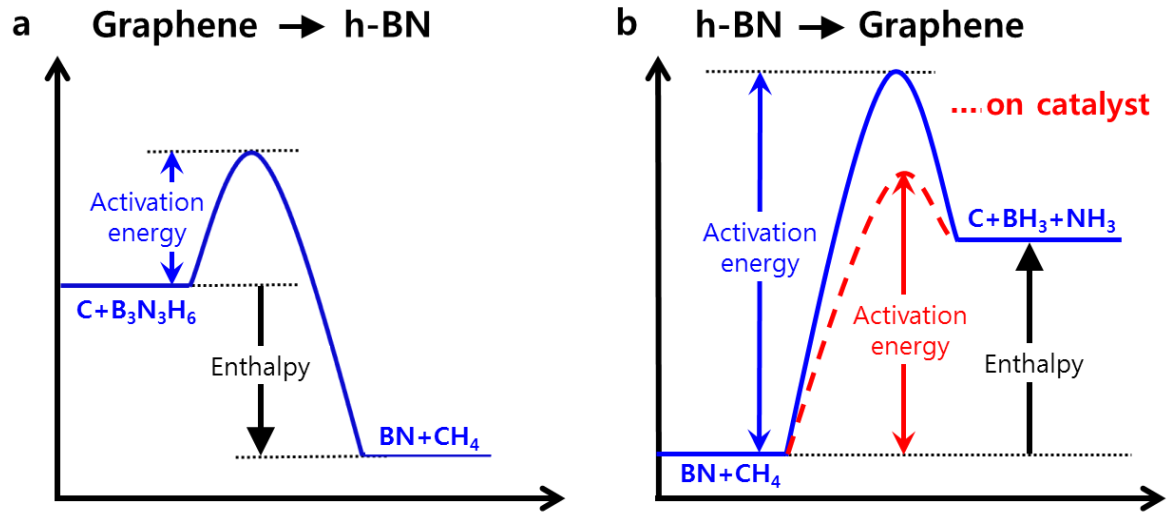

Figure 1. Thermodynamic energy diagrams of conversion reactions. (a) Conversion reaction from graphene to h-BN; exothermic reaction. (b) Conversion reaction from h-BN to graphene; endothermic reaction.

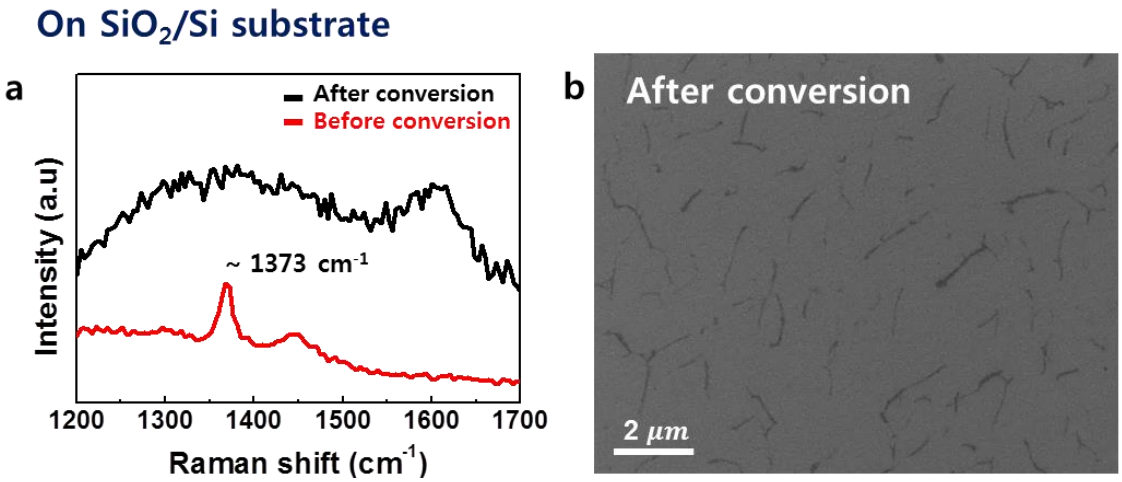

Figure 2. The conversion reaction on SiO_2/Si substrate. (a,b) Raman spectrum and SEM image of h-BN film transferred onto SiO_2/Si substrate before and after conversion reaction for 20 min. After the conversion reaction, the characteristic peak of h-BN at 1,373 cm^{-1} is not shown due to broad peaks of amorphous carbon.

3.4.2 Characterization of Graphene/h-BN In-Plane Heterostructure

In this study, we chose a Pt substrate as a catalyst, given extensive research demonstrating it to be the best catalyst for the hydrogenation[24] and the best substrate for growth of monolayer h-BN through low-pressure chemical deposition (LP-CVD).[3] Overall, the conversion was expected to proceed via a mechanism similar to the one outlined in Figure 3a. Reaction progress was monitored with samples that were transferred onto SiO_2/Si substrates after specific reaction times (Figure 3b-d) by using Raman spectroscopy (Figure 3e-g). Before conversion, a Raman band was observed at about 1373 cm^{-1}, which is attributed to the E_{2g} phonon mode of the monolayer h-BN (Figure 3e).[3, 25] However, the spectrum taken for a sample that had been subjected to a reaction for 20 min is characteristic of monolayer graphene (Figure 3g), with very narrow G (full width at half maximum (FWHM) = 16.10 cm^{-1}) and 2D (FWHM = 27.95 cm^{-1}) bands and a 2D/G intensity ratio of 2.5. In addition, the negligible D band observed implies that the produced graphene has the high quality.[26] A shorter 10 min reaction time gave a clear in-plane graphene and h-BN heterostructure (i-G/BN), as shown in Figure 3c; the purity of both the graphene (dark) and h-BN (bright) regions was also confirmed by the Raman spectra (Figure 3f).

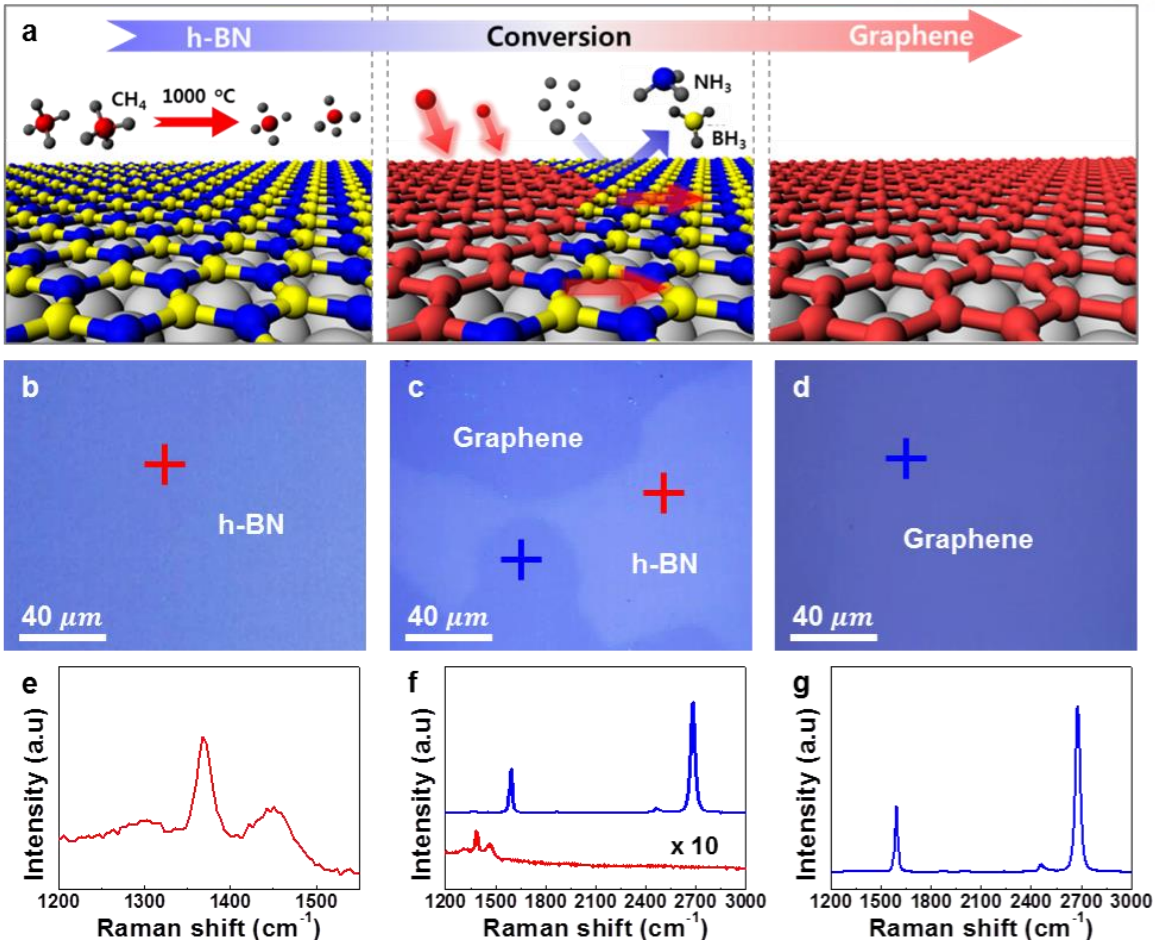

Figure 3. Conversion mechanism and Raman characterization. (a) Mechanism for the investigated conversion process. Boron, nitrogen, carbon, hydrogen, and platinum atoms are represented in yellow, blue, red, black, and gray, respectively. (b-g) Optical images (b-d) and Raman spectra (e-f) of h-BN, h-BN/graphene, and fully converted graphene samples transferred to SiO_2/Si substrates, resulting from the reaction times of 0 (b,e), 10 (c,f), and 20 min (d,g), respectively.

The pristine h-BN, i-G/BN, and fully converted graphene were further characterized by scanning electron microscopy (SEM), atomic force microscopy (AFM), and transmission electron microscopy (TEM). Figure 4a-c show SEM images of these samples transferred onto SiO_2/Si substrates. As expected, the graphene region was much brighter than the h-BN region given its higher conductivity. Furthermore, many dark lines were observed in the graphene region; these were identified as wrinkles by AFM (Figure 4d-f). The formation of this feature results from the differences in the thermal expansion coefficient between grown materials and metal substrates.[28] Although both graphene and h-BN have negative thermal expansion coefficients, that of graphene (approximately -8.0×10^{-6} K^{-1})[29] is far greater in magnitude than h-BN (approximately -2.7×10^{-6} K^{-1})[30], explaining why wrinkles are so pronounced in one and not the other.

TEM experiments revealed differences in vacancy formation due to the applied electron beam. A large triangular hole was generated in h-BN (Figure 4g) due to the difference in knock-on damage thresholds of boron (74 keV) and nitrogen (84 keV).[31] Because 80 keV of the electron beam was used for the measurement, boron atoms are removed first, followed by neighboring nitrogen atoms. On the other hand, the homoatomic configuration of graphene means that electron beam irradiation results in randomly shaped holes in the graphene sheet (Figure 4h).[32] Figure 4i shows electron energy loss spectroscopy (EELS) spectra for the h-BN (red line) and graphene (blue line) regions. h-BN had two visible edges, corresponding to the characteristic K-shell ionization edges of boron and nitrogen. In addition, the characteristic π^* and σ^* energy loss peaks at the boron K edge prove that the h-BN lattice has sp^2 bonds. Meanwhile, graphene showed that π^* and σ^* energy loss peaks at the carbon K edge are consistent with the sp^2 carbon bonds.

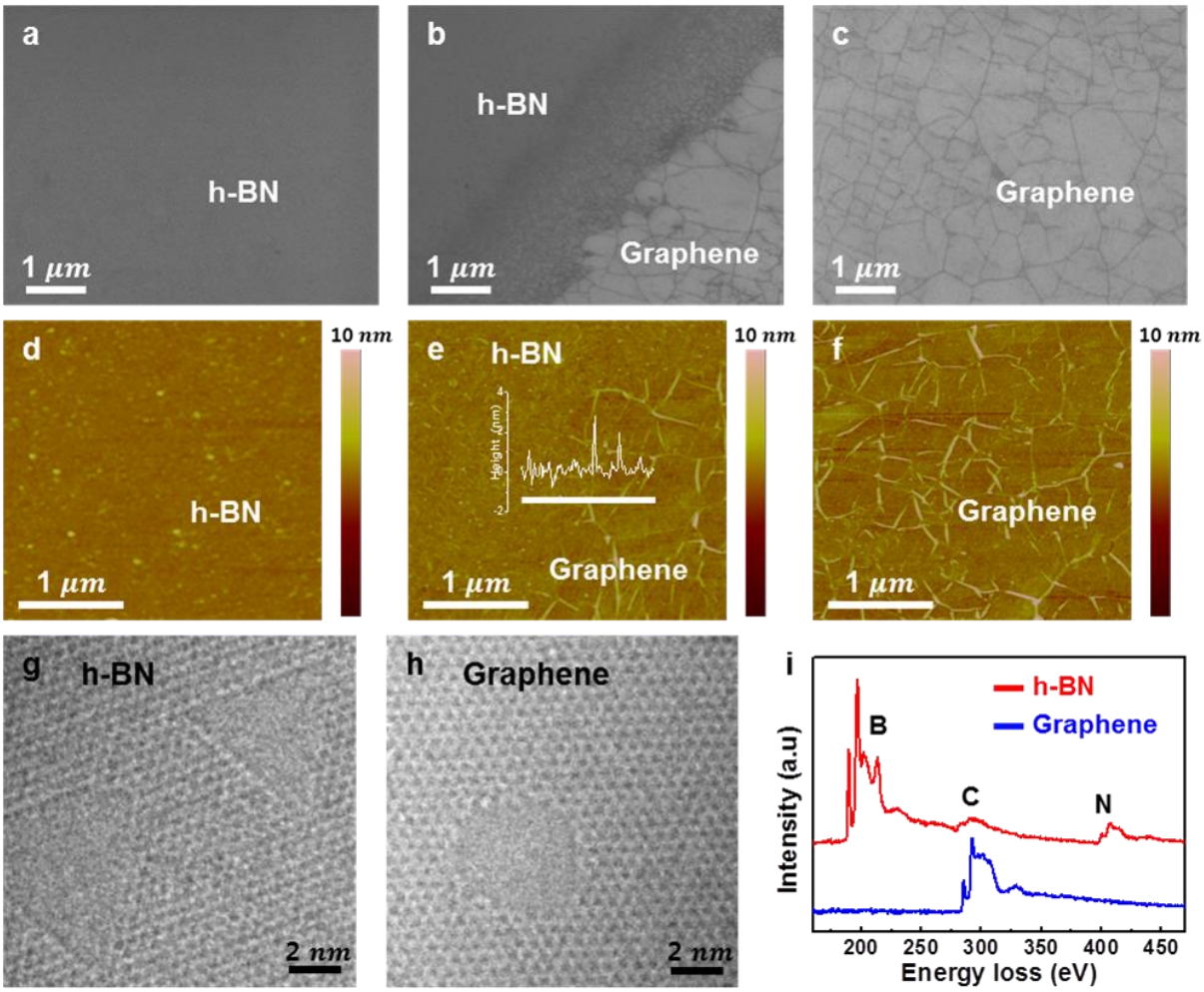

Figure 4. Morphology and microstructure. SEM and AFM images of h-BN (a,d), h-BN/graphene (b,e), and fully converted graphene (c,f) transferred onto SiO_2/Si substrates, of which conversion time was 0 min (a,d), 10 min (b,e), and 20 min (c,f), respectively. Inset of (e): Height profile corresponding to the white line in (e), indicative of significant wrinkles. (g-h) Atomic-resolution TEM images of monolayer h-BN and converted graphene. (i) EELS spectra of monolayer h-BN (red) and graphene (blue).

Figure 5a,b shows an optical image and Raman spectra for the interface region of h-BN and graphene. The interface Raman spectrum (green in Figure 5b) shows the G and D peaks of graphene with an intervening E_{2g} h-BN peak, further indicating hybridization.[18] The hybridized h-BNC was also identified in the SEM image of Figure 4b. Meanwhile, surface potential was estimated by measuring the contact potential difference with Kelvin probe microscopy (KPM).[33] The KPM image in Figure 5c shows that the measured effective surface potential (V_{sp}) of graphene ($V_{sp,G}$) is about 330 meV higher than that of h-BN ($V_{sp,h\text{-}BN}$). However, in the h-BNC region, this value changes gradually, which indicates a concentration gradient. The atomic concentration gradient of BN has been calculated from the V_{sp} values according to the following equation (3) (Figure 5d). We assumed that the measured surface potential at i-G/BN area was determined by the arithmetic mean of the surface potential of graphene and h-BN with concentration, since the surface potential is defined as electrostatic "*potential energy*" at the surface.

In probability theory, the arithmetic mean can be calculated as,

$$\mathrm{E(x)} = \sum_{i=0}^{\infty} x_i p_i \quad (x\text{: specific value, } p\text{: probability})$$

Accordingly, the surface potential can be written as,

$$V_{sp} = V_{sp,G} C_G + V_{sp,h-BN} C_{h-BN} \quad (\mathrm{C}: \text{concentration})$$

$$= V_{sp,G}(1 - C_{h-BN}) + V_{sp,h-BN} C_{h-BN}$$

From this equation, concentration of h-BN can be written as,

$$\text{Concentration of BN} = \frac{V_{sp} - V_{sp,h-BN}}{V_{sp,G} - V_{sp,h-BN}} \qquad (3)$$

These data confirm the presence of both fully converted and unconverted regions separated by a hybridized interface region in the partially reacted sample. This behavior is distinct from that observed during the conversion of graphene to h-BN;[18] in that case, the reaction proceeds throughout the sample. This observation implies that the Pt foil induces a spatial difference in reaction rate, indicating that the local reaction environment highly influences the conversion.

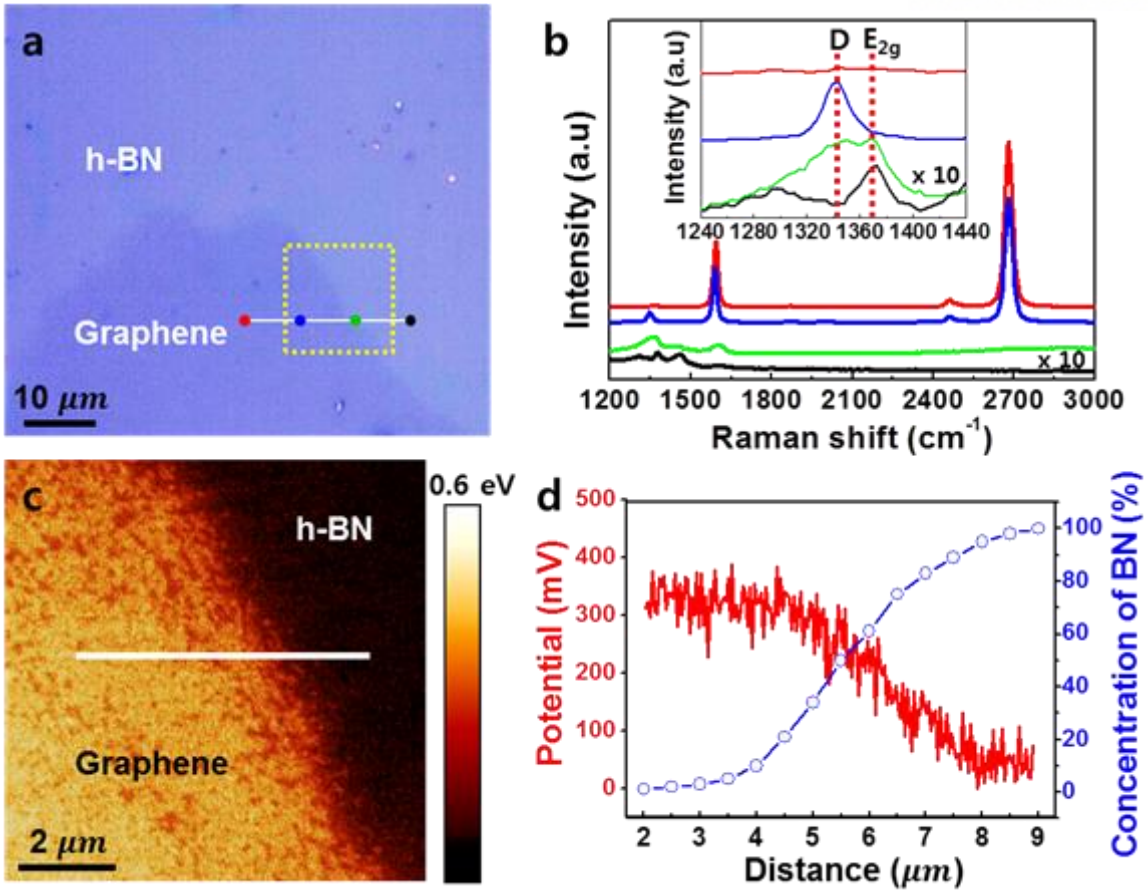

Figure 5. Measurement of surface potential for the i-G/BN heterostructure. (a) Optical image of the i-G/BN interface on SiO_2/Si substrate. (b) Raman spectra at different positions around the i-G/BN interface. (c) KPM image of the marked yellow area in (a), taken before transferring from the Pt substrate. (d) Plots of surface potential and BN concentration following the white line in (c).

Scanning tunneling microscopy (STM) was therefore used to further clarify the exact atomic structure and confirm conversion. The reaction was carried out on a Pt (111) single crystal for this purpose. STM images in Figure 6a and b show a narrow graphene region between the h-BN regions, and the height profile shown in Figure 6d indicates that Pt step edges were present under the graphene layer, as demonstrated by the illustration in Figure 6c. This observation indicates that the conversion reaction occurs at grain boundary of h-BN on the Pt step edges. A higher resolution STM image in Figure 6b shows that bonds were formed between graphene and h-BN, even though we could not clarify the exact atomic configuration of the interface between graphene and h-BN. Note than bright protrusions at h-BN region are not due to single atoms but due to the interfered Moire structure. The chemical configuration of each region was further analyzed by two-dimensional fast Fourier transform (2D-FFT) images and scanning tunneling spectroscopy (STS) spectra. The STS spectrum of the middle region (green line in Figure 6e) also shows marked differences from the side regions (blue and orange lines in Figure 6e), in that it shows a Dirac point at 0.3 eV below the Fermi level while the others do not. This is consistent with electron transfer from Pt to graphene, as confirmed by angle-resolved photoemission spectroscopy.[35] The $(01\bar{1}0)$ lattice spacing of 2.141 Å obtained in the middle region (Figure 6g) is shorter than the 2.193 and 2.182 Å values obtained for the left and right regions, respectively (Figure 6f and h). These values agree well with the $(01\bar{1}0)$ lattice spacing values of graphite (2.14 Å) and bulk h-BN (2.18 Å).[36] Meanwhile, the difference in the rotational orientations demonstrated by 2D-FFT in Figure 6f-h shows strong evidence that grain boundaries existed between the two h-BN domains before the conversion reaction; Figure 6f-h show three different regions with relative rotational orientation with $R0^{o}$, $R3^{o}$ and $R9.5^{o}$, respectively. The interfacial region in Figure 6 is obviously distinguished from the interface of an unreacted h-BN grain boundary shown in Figure 7a-b, in which the additional narrow graphene region does not appear between two h-BN layers. Thus, it supports that the narrow interface in Figure 6 is converted graphene.

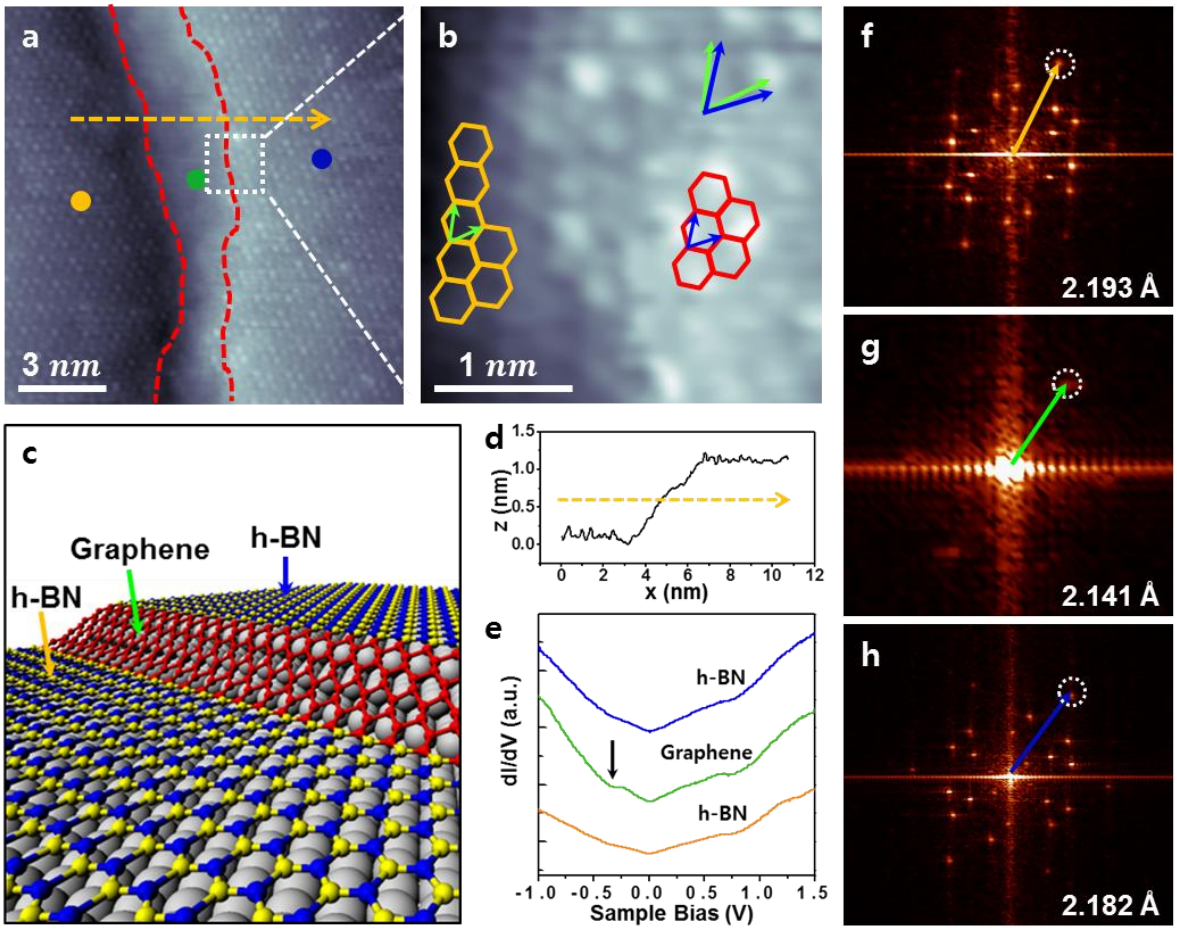

Figure 6. STM analysis of early conversion. (a) An STM image of the i-G/BN heterostructure on Pt (111). The sample bias (V_s) =50 mV, and the feedback current (I_f) = 5 nA. The interfaces between h-BN and graphene are marked with red dashed lines. (b) A magnification image of the marked white square in (a). (c) Illustration of the i-G/BN heterostructure. (d) Height profile corresponding to the orange line in (a). (e) d*I*/d*V* spectra corresponding to the colored points in (a). (f-h) FFT results corresponding to the colored points marked in (a). Colored arrows indicate (01-10) directions of h-BN or graphene layers, relative angles were estimated as R0° (orange), R3° (green), and R9.5° (blue), respectively.

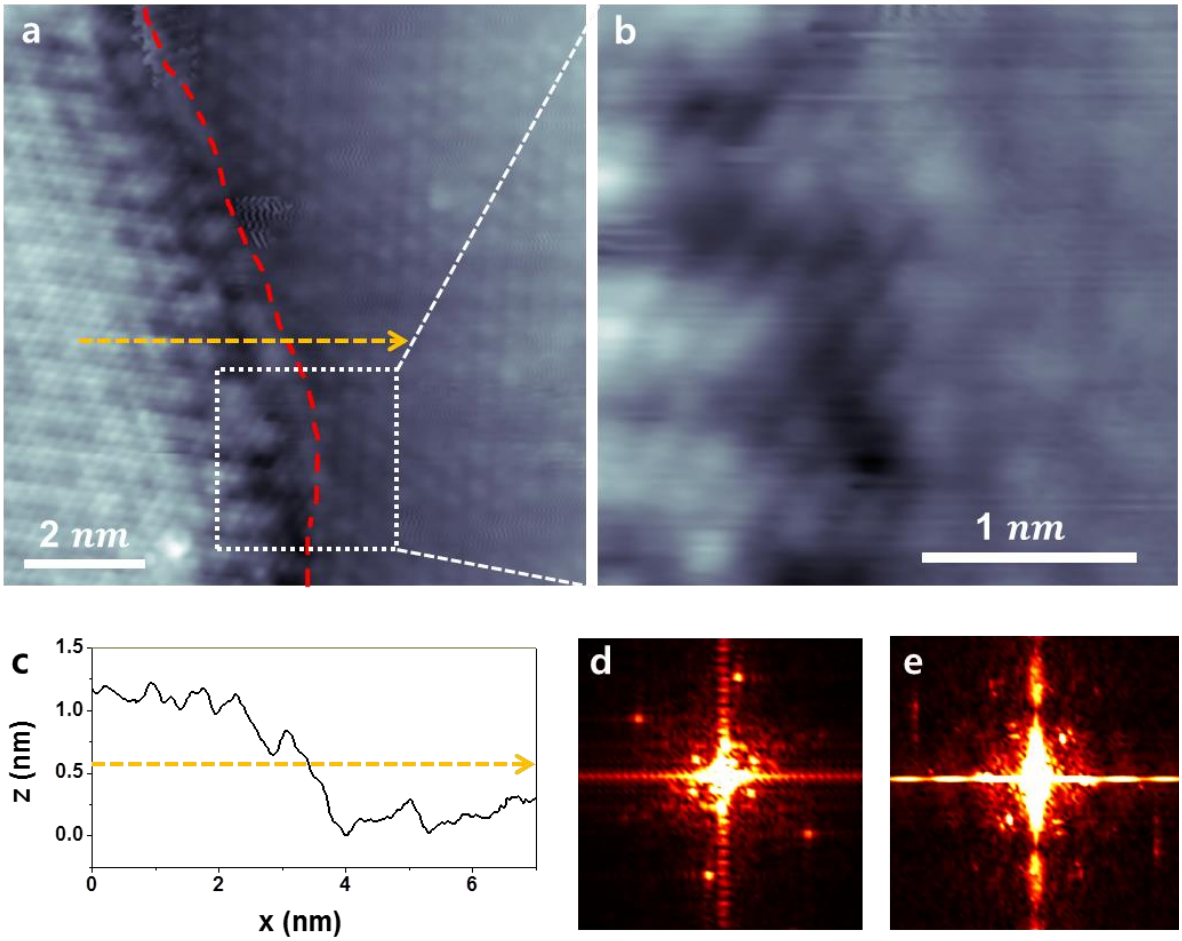

Figure 7. Scanning tunneling microscopy (STM) study on unreacted h-BN grain boundary in initial conversion reaction. (a) High-resolution STM image of h-BN on the step edge of Pt (111). The red dash line is marked on grain boundary of h-BN. (b) High-magnification image of the marked white square in (a). (c) Height profile corresponding to the orange line in (a). (d,e) The fast Fourier transform (FFT) results of h-BN (right) and h-BN (left) part. The rotational angle difference between two h-BN region was estimated as 23° from FFT images (d,e).

3.4.3 Conversion Process of h-BN to graphene on Pt for the In-Plane Heterostructure

Shorter reactions were performed to further elucidate the conversion process. Figure 8a-e track these conversions by SEM for the reaction times of 0, 0.5, 1, 3, and 5 min, respectively; the associated illustrations are provided in Figure 8f-j, respectively. Narrow dark lines of converted graphene are observed in the 0.5 min reaction, and become significantly wider after 1 min. In the 3 min reaction sample, the dark graphene regions have grown together, while the brighter h-BN regions take on isolated oval shapes. Complete conversion was observed in multiple portions after 5 min. This reaction occurs mainly at the underlying step edges of the catalyst, with no reaction occurring initially for sparser regions (Figure 9). The SEM image in Figure 9c shows h-BN layer, which is darker than h-BN in Figure 8b. The dark lines are supposed to be grain boundaries of h-BN. The conversion rate of h-BN is affected by step edges of Pt grain. Note that the conversion reaction at the region having numerous step edges (green box, Figure 9b) is faster than at sparse step edge region (yellow box, Figure 9c) in short reaction time. This is consistent with the fact that the catalytic activity of Pt atoms on the catalyst edges is significantly higher than that of Pt atoms in the bulk lattice.[34] Of course, longer reaction for 20 min induces full conversion of whole h-BN to graphene as shown in Figure 4 and 8.

In addition, the conversion rate is high near the catalyst grain boundaries (Figure 10). Note that h-BN near the Pt grain boundary was already converted to graphene ("G" region). The conversion reaction rate of the green box region (Figure 10d) is faster than that of the blue box region (Figure 10c). Gong et al.[18] suggested that graphene conversion to h-BN begins at point defects. However, if this were the case in our reaction, graphene islands should be observed rather than h-BN islands (Figure 11a-c). However, the observed behavior in Figure 8d indicates that the reaction proceeds from grain boundaries of h-BN (Figure 11d-f).

These observations suggest a plausible reaction mechanism. At high temperatures, methane molecules decompose into carbon and hydrogen radicals. The hydrogen radicals could bind to the Pt atoms, which would be followed by the etching of h-BN to form NH_x and BH_x. This would proceed most effectively at the h-BN grain boundaries because it would be easier for hydrogen atoms to diffuse at these points. We performed the hydrogenation of h-BN on Pt and SiO_2/Si substrates by flowing H_2 gas only, to elucidate that the hydrogen-etching by the hydrogen radicals decomposed from CH_4 occurs at the initial reaction step. Each h-BN film prepared on the Pt foil and SiO_2/Si substrate was placed in the center of the tube furnace, and only H_2 gas (10 sccm) was introduced into the furnace at 800 °C. We observed that the whole h-BN film was etched at 1000 °C even for 1 min, and so we carried out the hydrogen-etching reaction at low temperature, 800 °C. On the Pt substrate, the dissociation of the H_2 gas in that

temperature generates H radicals which can etch h-BN sheet by the H-assisted detachment of B and N from h-BN grain boundary.[9] After the hydrogenation of h-BN for 5 min, the sample was characterized by SEM and AFM image. Figure 12a,b show SEM and AFM images of hydrogen-etched h-BN film transferred onto SiO_2/Si substrate. We can easily distinguish the etched and unetched areas of h-BN film by SEM contrast. It is supposed that the etching of h-BN occurs from grain boundary possibly due to diffusion of hydrogen through the grain boundary. To confirm the catalytic role of Pt in h-BN etching, the hydrogen treatment of the h-BN film on SiO_2/Si substrate was attempted. However, it was found that h-BN sheet remained unetched on SiO_2/Si substrate (Figure 12c,d). Therefore, we confirmed that the h-BN on Pt substrate can be etched by hydrogenation, which is an initial step in the conversion mechanism.

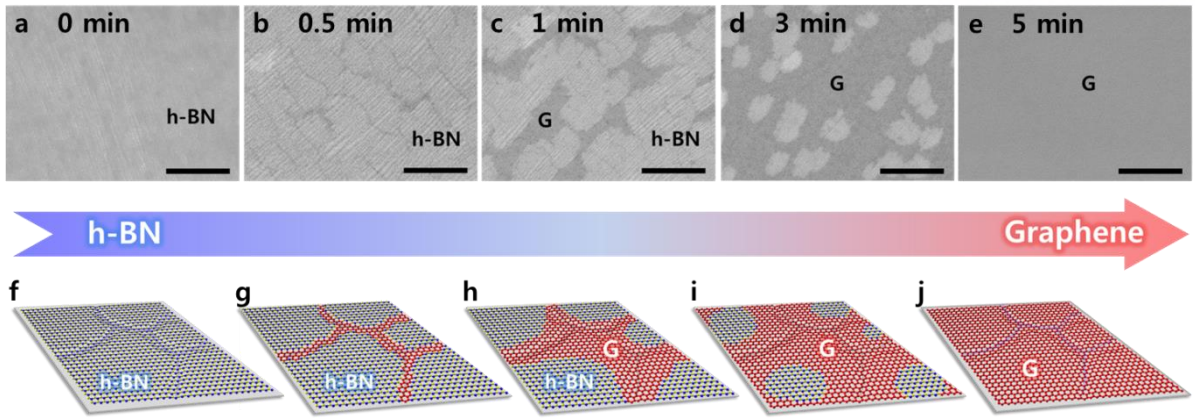

Figure 8. Early conversion of h-BN to graphene. (a-e) SEM images for the conversion times of (a) 0, (b) 0.5, (c) 1, (d) 3, and (e) 5 min, respectively. The SEM images were measured on Pt foil. All scale bars are 500 nm. (f-j) Schematic illustrations of time dependent reaction mechanism.

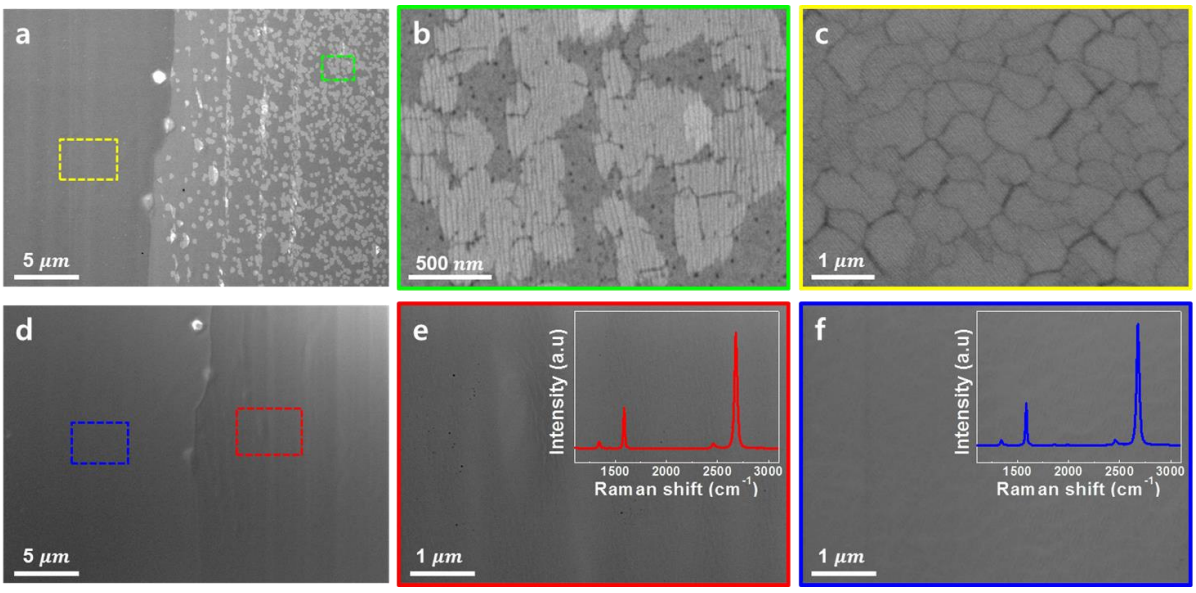

Figure 9. Effect of Pt step edges on the conversion reaction. (a) SEM image showing two Pt grains after the conversion reaction for 1 min. The contrast difference between two grains comes from the Pt grain orientation. (b,c) Zoom-in images of the green (b) and yellow (c) box in (a). The bright oval shapes in (b) are for h-BN and dark area is for graphene. (d) SEM image of conversion reaction on two Pt grains for 20 min shows full conversion to graphene. (e,f) Zoom-in images of the red (e) and blue (f) box in (d). Inset of (e,f): Raman spectra of fully converted graphene samples transferred onto SiO_2/Si substrate.

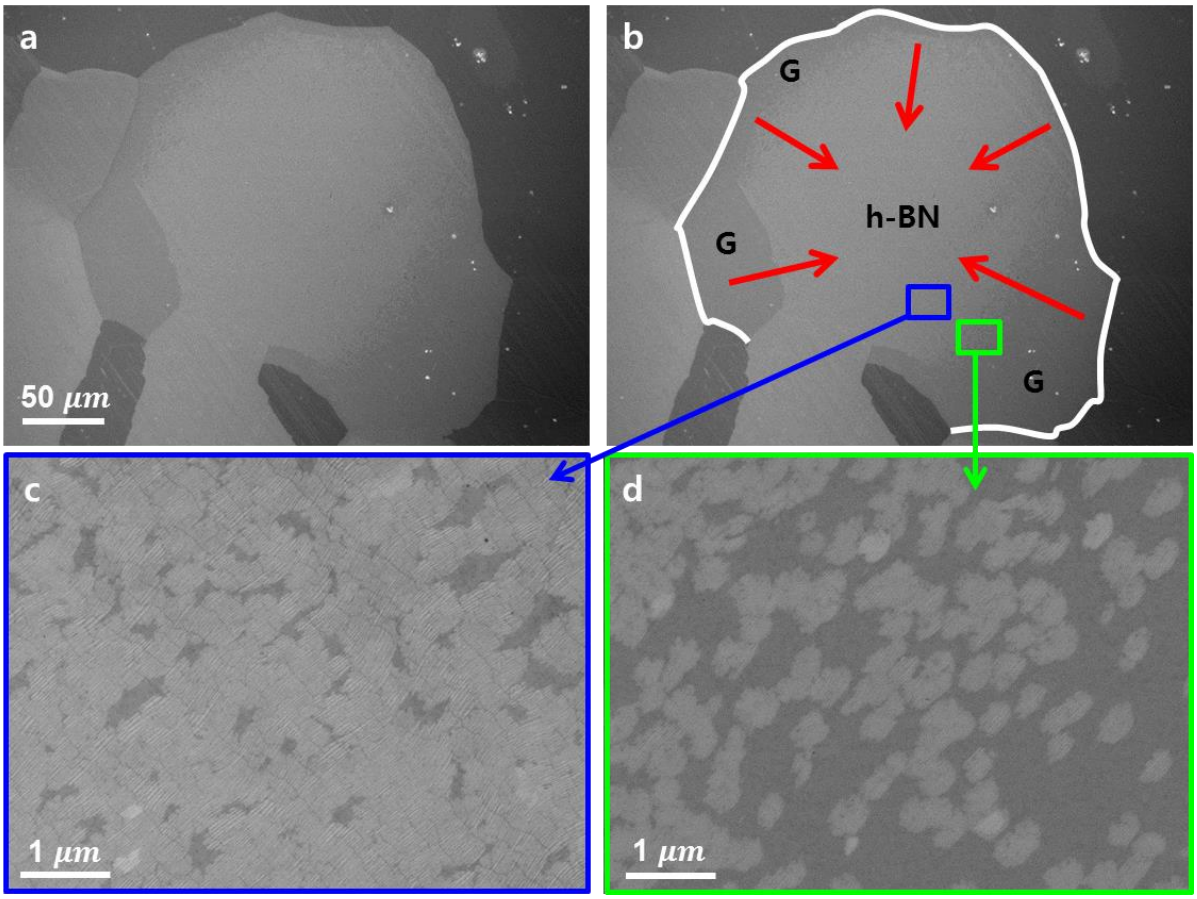

Figure 10. Effect of Pt grain boundary on the conversion reaction. (a,b) SEM images of conversion reaction on Pt grain for 1 min. The grain boundary of Pt is marked with the white line and the conversion reaction proceeds in the direction of red arrows. (c,d) Zoom-in images of the blue (c) and green (d) box in (b).

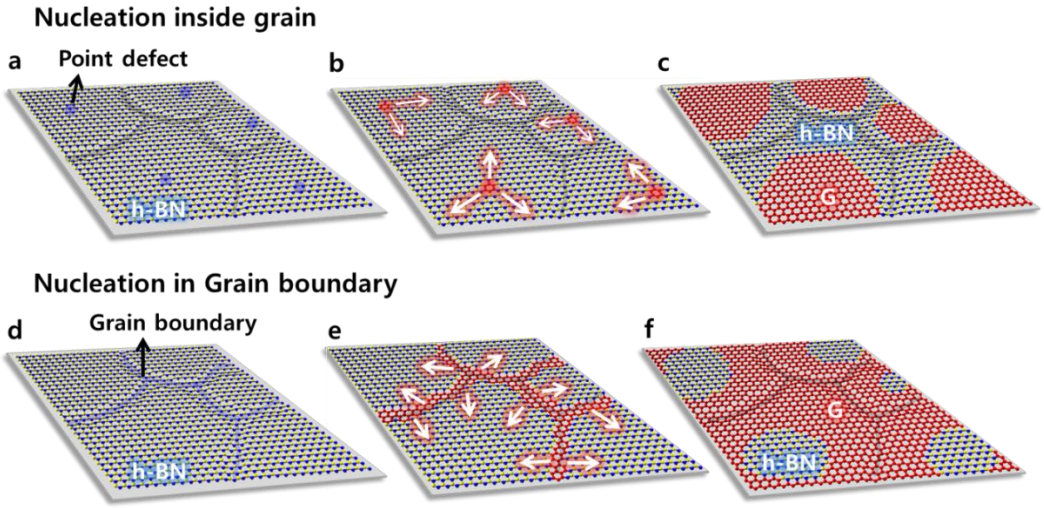

Figure 11. Schemes for two types of initial points in the conversion reaction. (a-c) scheme of the conversion reaction initialized on single defect in basal grain of h-BN. It induces graphene islands. (d-f) scheme of the conversion reaction initialized on grain boundary of h-BN. It induces h-BN islands.

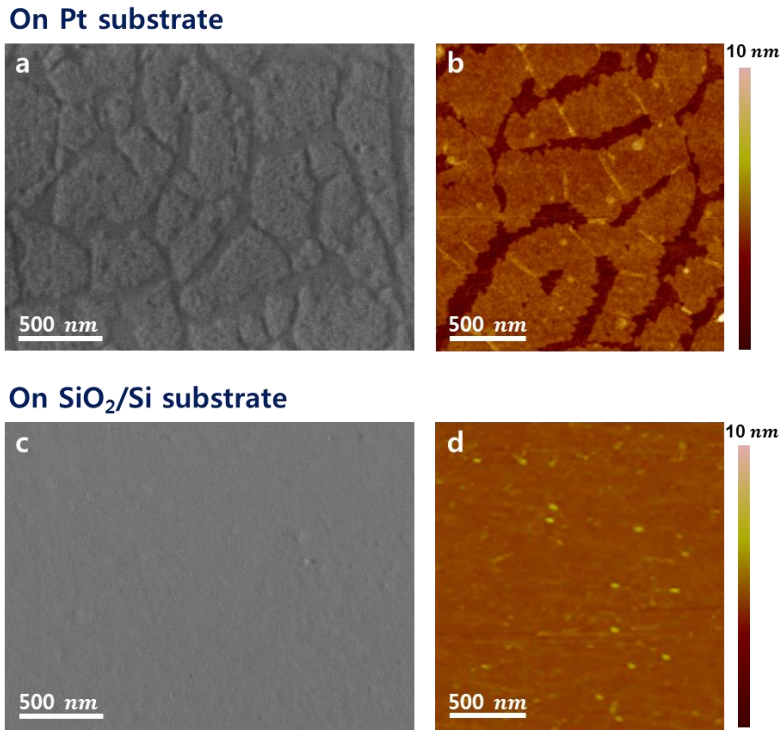

Figure 12. Hydrogen-etching of h-BN on Pt and SiO_2/Si substrates. (a,b) SEM and AFM images of hydrogen-etched h-BN film transferred on SiO_2/Si substrate after the hydrogenation on Pt substrate. (c,d) SEM and AFM images of hydrogen-etched h-BN film on SiO_2/Si substrate.

3.4.4 Conversion Reaction of h-BN on the Other Substrate (SiO_2, Cu, Ru)

In addition, to compare the catalytic effect of Pt with that of other substrates, we performed the conversion reaction of h-BN on SiO_2, Cu, and Ru substrates under the same experimental condition as Pt substrate. The Raman spectra in Figure 2a were taken from the sample before and after the conversion reaction on SiO_2/Si substrate for 20 min. The Raman spectrum of h-BN before the conversion reaction shows a characteristic peak of h-BN. The Raman spectrum after the conversion reaction indicates that the amorphous carbon was formed on h-BN during the reaction because of no catalytic effect of SiO_2. The characteristic peak of h-BN at 1,373 cm^{-1} is not shown due to broad peaks of amorphous carbon. In the SEM image of h-BN film on SiO_2/Si substrate after the reaction (Figure 2b), the dark lines were observed which are regarded as amorphous carbon lump possibly forming on wrinkles or grain boundary of h-BN during the reaction, which is consistent with the Raman spectrum. The Raman spectrum of the sample transferred onto SiO_2/Si substrate after doing the conversion reaction on Cu (Figure 13) also demonstrate the negligible conversion reaction on Cu substrate. We observed only Raman peak of h-BN even after the conversion reaction (Figure 13a). Note that h-BN sheet was transferred on Cu foil and its Raman spectrum was not measured before the conversion reaction due to fluorescence of Cu.

We also performed the conversion reaction on ruthenium (Ru) foil (Goodfellow). While Pt metal is known as the best catalyst for hydrogenation, Ru metal can be also used for selective hydrogenation. In 2011, Sutter *et al.* reported H_2 induced etching of h-BN grown on Ru substrate.[27] They mentioned that the hydrogen etching process is the H-assisted detachment of B and N from the h-BN films, forming hydrated BH_x and NH_x species from the h-BN edge. However, They considered that Pt metal has higher catalytic effect for hydrogenation than Ru.[27] To confirm their catalytic abilities for our reaction, we performed the conversion reaction of h-BN on Pt and Ru substrates and measured X-ray photoemission spectroscopy (XPS) spectra to investigate the degree of conversion reaction by comparing peak intensities of the elements B, N, and C. The B and N 1s peak of h-BN grown on Pt and Ru substrates are located at 190.08 eV and 397.58 eV, respectively, similarly to the position of h-BN in previously reported papers. After the conversion reaction of h-BN on Pt substrate for 20 min, we observed XPS spectra (Figure 13c-e) with only increased C peak corresponding to the graphene, but no B and N peaks. It means that the h-BN film on Pt substrate was completely converted to graphene. In contrast, we could observe the B and N 1s peaks after the same reaction on Ru foil, although their intensities decreased (Figure 13f-h). This observation demonstrated that h-BN was not fully converted to graphene, indicating lower catalytic ability of Ru than Pt. The B, N, and C atomic percent ratios from XPS survey before and after the conversion were calculated to be 32 : 31 : 27 and 22 : 22 : 56, respectively. Table 1

summarizes conversion ratios of h-BN to graphene on Pt and Ru at different reaction times, which were determined by XPS. The catalytic activity of Pt was reported once, but did not show controlled heterostructures; The exposure of ethylene to h-BN on Pt (111) involved significant hydrogen-induced etching of h-BN and subsequently independent nucleation and growth of graphene, which finally replaced h-BN.[9]

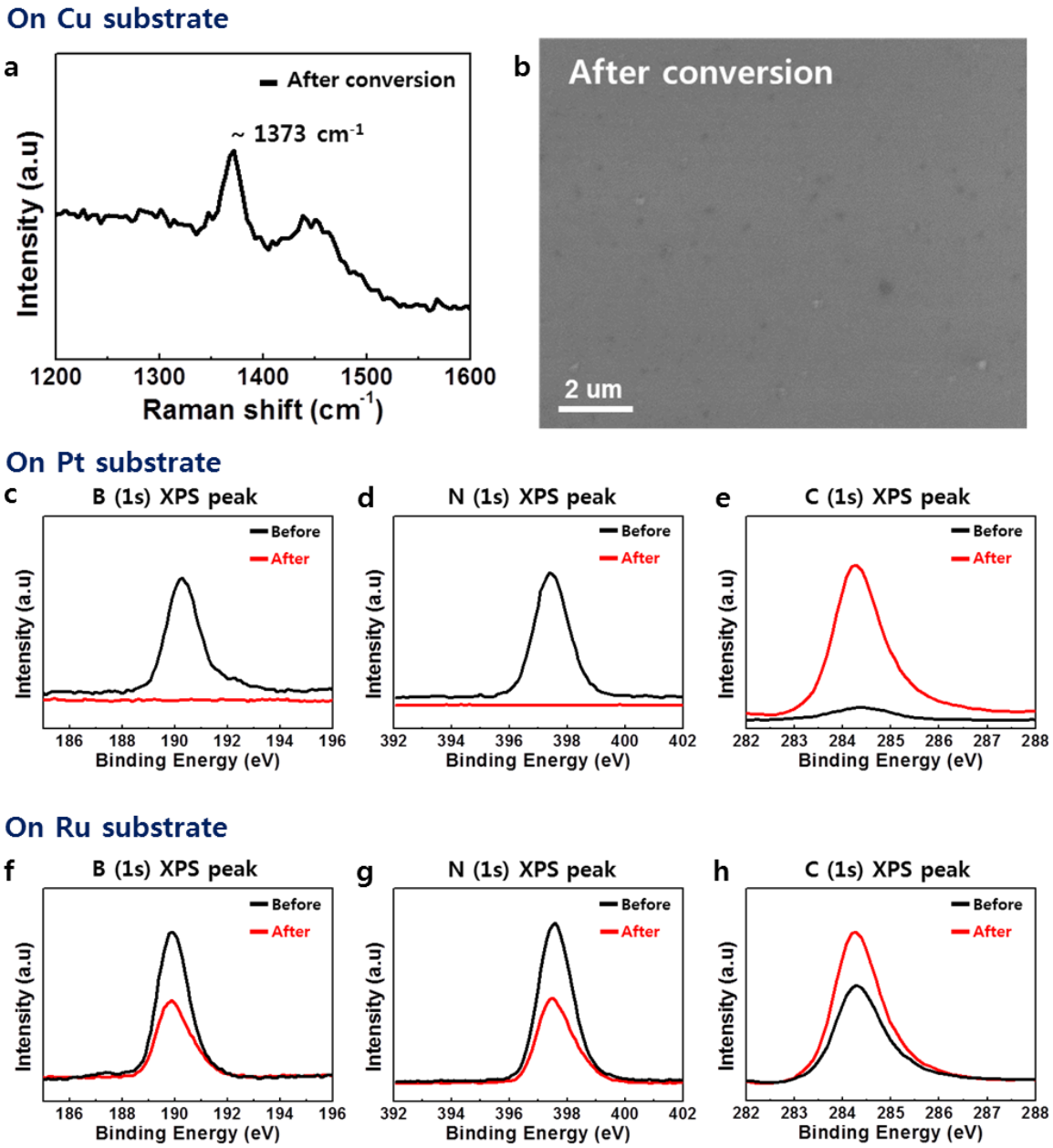

Figure 13. The conversion reaction on Cu, Pt, and Ru substrates. (a,b) Raman spectrum and SEM image of h-BN film transferred onto SiO_2/Si substrate after conversion reaction on Cu substrate. (c-e) XPS spectra of (c) B 1s, (d) N 1s, and (e) C 1s on Pt substrate. (f-h) XPS spectra of (f) B 1s, (g) N 1s, and (h) C 1s on Ru substrate. The black and red lines are associated with films before and after conversion reaction for 20 min, respectively.

Table 1. The conversion ratios of h-BN to graphene on Pt, Ru, Cu, and SiO_2/Si substrates

Substrate	Reaction Time (min)		
	5 min	10 min	20 min
Pt	20 %	50 %	100 %
Ru	- %	10 %	30 %
Cu	No conversion reaction		
SiO_2/Si	No conversion reaction		

* The CH_4 (5 sccm) and Ar (50 sccm) was introduced into the furnace at 1000 °C

3.4.5 Fabrication of Patterned In-Plane Heterostructure Using Patterned SiO_2-Pt Substrate

Since this conversion reaction is highly dependent on the substrate, it can be spatially controlled by patterned substrates. We first prepared a patterned substrate consisting of Pt and SiO_2 using e-beam lithography and reactive-ion etching. The CVD-grown h-BN film was then transferred to the patterned substrate, reacted, and transferred to a SiO_2/Si substrate (Figure 14a). Figure 14b shows an optical image of this alternative graphene/h-BN film on the SiO_2/Si substrate. Meanwhile, the red and blue lines in Figure 14c show the corresponding Raman spectra of the h-BN and graphene regions, respectively. Raman image mapping (Figure 14d) in the 2D band (2630-2730 cm^{-1}) confirms that only the h-BN layers on the Pt area were converted to graphene. This process is distinct from previous ones, in which a deposited silica mask was used as a protecting layer.[18] This newer, mask-free process is advantageous because we do not need to consider any diffusion of decomposed materials underneath the silica mask layer (Figure 15). In the case using a metal substrate, SiO_2 mask layer cannot prohibit the diffusion of decomposed carbon atoms in the metal substrate, and so converted graphene is not defined (Figure 16). However, in the case of Pt-SiO_2 substrate, the decomposed carbon atoms cannot diffuse to the SiO_2 region, and finally the conversion to graphene occurs only on Pt surface, providing with a defined graphene pattern. Therefore, the spatially controlled conversion on Pt-patterned substrate is applied to h-BN to graphene conversion reaction more appropriately. But, the optimizing the fabrication process including Pt etching and SiO_2 deposition is not simple. Especially, making a negligible height difference between Pt and deposited SiO_2 is very challenging. We are still improving this patterning process. Despite of technical problem for making patterned substrate, we believe conversion reaction itself has a significant advantage for the good sharpness between patterned graphene and h-BN, when metal substrate is used for the reaction owing to diffusion issue.

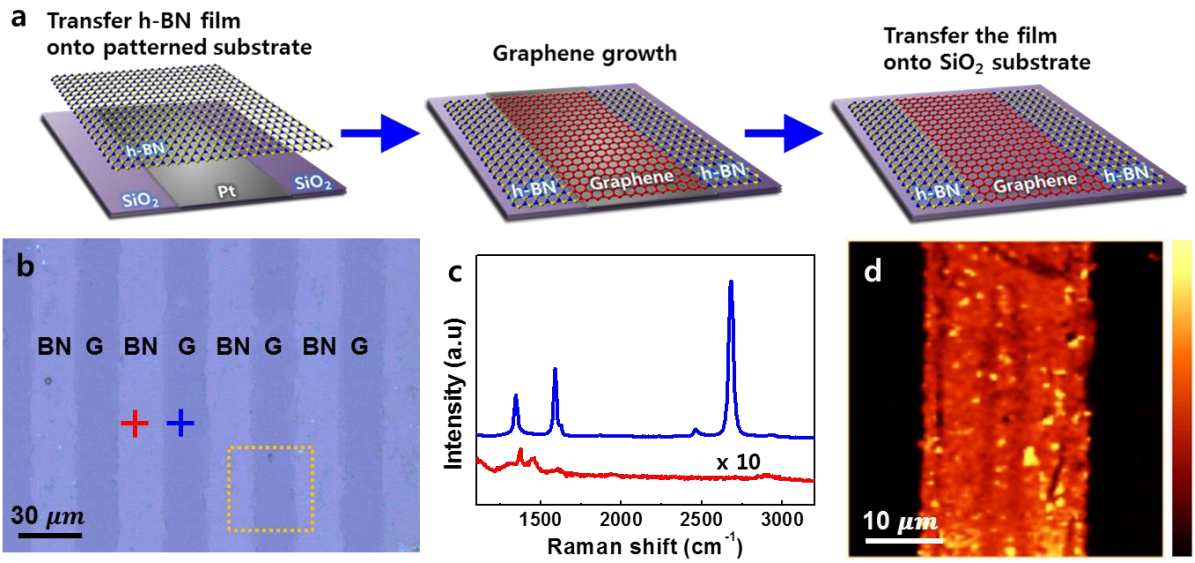

Figure 14. Fabrication of patterned i-G/BN heterostructures. (a) Mask-free patterning process on Pt-patterned substrate. The conversion only occurs at the Pt region. (b) Optical image of the graphene/h-BN stripes on SiO_2/Si substrate. (c) Raman spectra of the h-BN (red) and graphene (blue) regions marked in (b). (d) Raman mapping in the 2D (2630-2730 cm^{-1}) band for the marked area in (b).

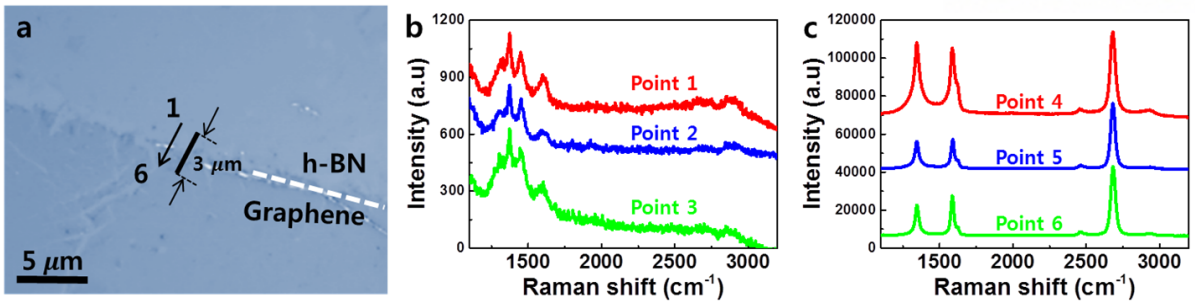

Figure 15. Interface of patterned i-G/BN heterostructures. (a) Optical image of the interface between graphene and h-BN grown on patterned substrate. The Raman spectra were obtained at different positions (black line) with 500 nm interval in (a). The white dash line is marked on the interface of h-BN and graphene. (b,c) the spectrum of h-BN (b) was changed to that of graphene (c) in the region between 3 and 4 point. At point 4, the D band is large due to contribution of the interface region. It means that the interface between graphene and h-BN has the good sharpness with less than ~ 500 nm.

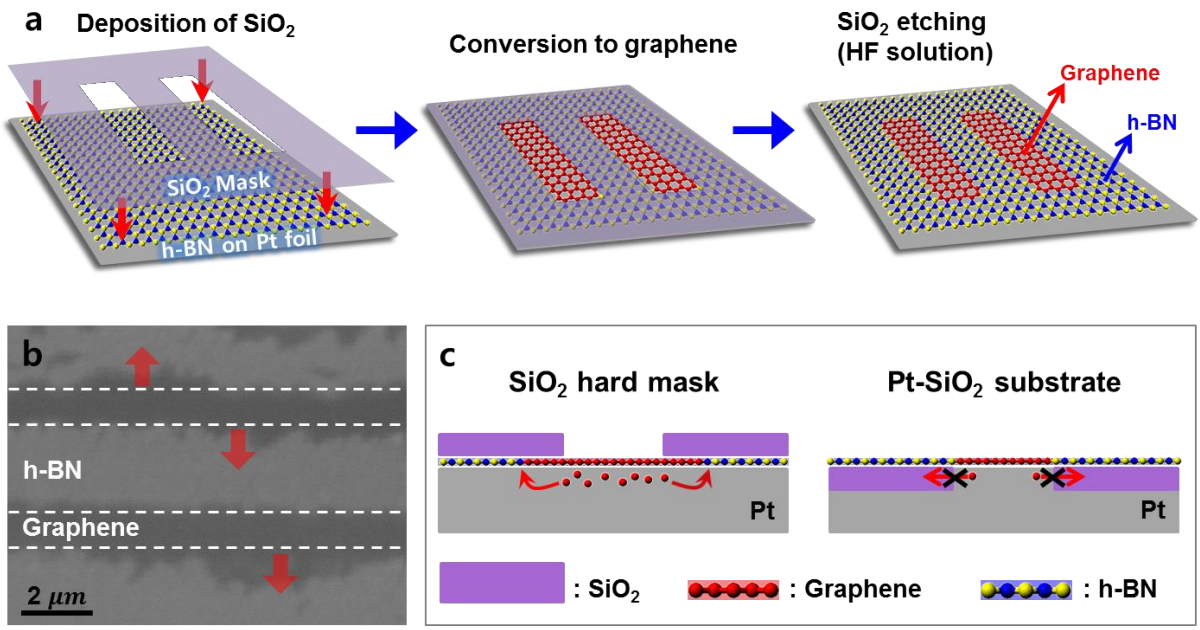

Figure 16. Comparison of patterned G/BN heterostructures. (a) Patterned conversion reaction using SiO_2 hard mask.[5] (b) SEM images of the graphene/h-BN stripes on Pt after the etching of SiO_2 mask. The removed SiO_2 masks on the h-BN regions are marked with white dashed lines. (c) Problem of patterned conversion using SiO_2 hard mask.

3.5 Conclusion

In conclusion, we first accomplished the conversion reaction of h-BN to graphene on a catalytic Pt substrate and fully characterized the resulting h-BN, i-G/BN, and converted graphene segments. Pt showed higher catalytic activity than SiO_2, Cu, and Ru, and followed a reaction pathway that began with hydrogenation and ended with graphene growth. Further analysis suggested that the hydrogenation process begins at the h-BN grain boundaries. Finally, we used the results obtained in this research to develop a new process for fabricating patterned i-G/BN heterostructures without a protecting mask layer. We believe that this work extends the available understanding of the thermodynamics of graphene and h-BN growth and will also accelerate the development of new types of i-G/BN heterostructure devices.

3.6 References

1. Yan, Z.; Peng, Z.; Tour, J. M. Chemical vapor deposition of graphene single crystals. *Acc. Chem. Res.* **2014**, *47*, 1327-1337.
2. Li, X.; Cai, W.; An, J.; Kim, S.; Nah, J.; Yang, D.; Piner, R.; Velamakanni, A.; Jung, I.; Tutuc, E.; Banerjee, S. K.; Colombo, L.; Ruoff, R. S. Large-area synthesis of high-quality and uniform graphene films on copper foils. *Science* **2009**, *324*, 1312-1314.
3. Kim, G.; Jang, A. R.; Jeong, H. Y.; Lee, Z.; Kang, D. J.; Shin, H. S. Growth of high-crystalline, monolayer hexagonal boron nitride on recyclable platinum foil. *Nano Lett.* **2013**, *13*, 1834-1839.
4. Kim, K. K.; Hsu, A.; Jia, X.; Kim, S. M.; Shi, Y.; Hofmann, M.; Nezich, D.; Rodriguez-Nieva, J. F.; Dresselhaus, M.; Palacios, T.; Kong, J. Synthesis of monolayer hexagonal boron nitride on Cu foil using chemical vapor deposition. *Nano Lett.* **2012**, *12*, 161-166.
5. Watanabe, K.; Taniguchi, T.; Kanda, H. Direct-bandgap properties and evidence for ultraviolet lasing of hexagonal boron nitride single crystal. *Nat. Mater.* **2004**, *3*, 404-409.
6. Han, G. H.; Rodríguez-Manzo, J. A.; Lee, C.-W.; Kybert, N. J.; Lerner, M. B.; Qi, Z. J.; Dattoli, E. N.; Rappe, A. M.; Drndic, M.; Johnson, A. T. C. Continuous growth of hexagonal graphene and boron nitride in-plane heterostructures by atmospheric pressure chemical vapor deposition. *ACS Nano* **2013**, *7*, 10129-10138.
7. Liu, L.; Park, J.; Siegel, D. A.; McCarty, K. F.; Clark, K. W.; Deng, W.; Basile, L.; Idrobo, J. C.; Li, A.-P.; Gu, G. Heteroepitaxial growth of two-dimensional hexagonal boron nitride templated by graphene edges. *Science* **2014**, *343*, 163-167.
8. Sutter, P.; Cortes, R.; Lahiri, J.; Sutter, E. Interface formation in monolayer graphene-boron nitride heterostructures. *Nano Lett.* **2012**, *12*, 4869-4874.
9. Sutter, P.; Huang, Y.; Sutter, E. Nanoscale integration of two-dimensional materials by lateral heteroepitaxy. *Nano Lett.* **2014**, *14*, 4846-4851.
10. Gao, Y.; Zhang, Y.; Chen, P.; Li, Y.; Liu, M.; Gao, T.; Ma, D.; Chen, Y.; Cheng, Z.; Qiu, X.; Duan, W.; Liu, Z. Toward monolayer uniform hexagonal boron nitride–graphene patchworks with zigzag linking edges. *Nano Lett.* **2013**, *13*, 3439-3443.
11. Jun, S.; Li, X.; Meng, F.; Ciobanu, C. V. Elastic properties of edges in BN and SiC nanoribbons and of boundaries in C-BN superlattices: A density functional theory study. *Phys. Rev. B* **2011**, *83*, 153407.
12. Li, J.; Shenoy, V. B. Graphene quantum dots embedded in hexagonal boron nitride sheets. *Appl. Phys. Lett.* **2011**, *98*, 013105.
13. He, J.; Chen, K.-Q.; Fan, Z.-Q.; Tang, L.-M.; Hu, W. P. Transition from insulator to metal induced by hybridized connection of graphene and boron nitride nanoribbons. *Appl. Phys. Lett.* **2010**, *97*,

193305.

14. Ramasubramaniam, A.; Naveh, D. Carrier-induced antiferromagnet of graphene islands embedded in hexagonal boron nitride. *Phys. Rev. B* **2011**, *84*, 075405.
15. Levendorf, M. P.; Kim, C.-J.; Brown, L.; Huang, P. Y.; Havener, R. W.; Muller, D. A.; Park, J. Graphene and boron nitride lateral heterostructures for atomically thin circuitry. *Nature* **2012**, *488*, 627-632.
16. Havener, R. W.; Kim, C.-J.; Brown, L.; Kevek, J. W.; Sleppy, J. D.; McEuen, P. L.; Park, J. Hyperspectral imaging of structure and composition in atomically thin heterostructures. *Nano Lett.* **2013**, *13*, 3942-3946.
17. Liu, Z.; Ma, L.; Shi, G.; Zhou, W.; Gong, Y.; Lei, S.; Yang, X.; Zhang, J.; Yu, J.; Hackenberg, K. P.; Babakhani, A.; Idrobo, J.-C.; Vajtai, R.; Lou, J.; Ajayan, P. M. In-plane heterostructures of graphene and hexagonal boron nitride with controlled domain sizes. *Nat. Nanotechnol.* **2013**, *8*, 119-124.
18. Gong, Y.; Shi, G.; Zhang, Z.; Zhou, W.; Jung, J.; Gao, W.; Ma, L.; Yang, Y.; Yang, S.; You, G.; Vajtai, R.; Xu, Q.; MacDonald, A. H.; Yakobson, B. I.; Lou, J.; Liu, Z.; Ajayan, P. M. Direct chemical conversion of graphene to boron-and nitrogen-and carbon-containing atomic layers. *Nat. Commun.* **2014**, *5*, 3193.
19. Lu, J.; Zhang, K.; Feng Liu, X.; Zhang, H.; Chien Sum, T.; Castro Neto, A. H.; Loh, K. P. Order–disorder transition in a two-dimensional boron–carbon–nitride alloy. *Nat. Commun.* **2013**, *4*, 2681.
20. Golberg, D.; Bando, Y.; Tang, C. C.; Zhi, C. Y. Boron nitride nanotubes. *Adv. Mater.* **2007**, *19*, 2413-2432.
21. Han, W.; Bando, Y.; Kurashima, K.; Sato, T. Synthesis of boron nitride nanotubes from carbon nanotubes by a substitution reaction. *Appl. Phys. Lett.* **1998**, *73*, 3085-3087.
22. Wang, X.-B.; Weng, Q.; Wang, X.; Li, X.; Zhang, J.; Liu, F.; Jiang, X.-F.; Guo, H.; Xu, N.; Golberg, D.; Bando, Y. Biomass-directed synthesis of 20 g high-quality boron nitride nanosheets for thermoconductive polymeric composites. *ACS Nano* **2014**, *8*, 9081-9088.
23. Atkins, P. W. Physical chemistry. In *Physical chemistry*; Atkins, P. W., Ed.; Oxford University Press: Oxford, 1982.
24. Rylander, P. N. Platinum Metal Catalysts. In *Catalytic Hydrogenation over Platinum Metals*; Rylander, P. N., Ed.; Academic Press: Waltham, 1967; pp 3-29.
25. Gorbachev, R. V.; Riaz, I.; Nair, R. R.; Jalil, R.; Britnell, L.; Belle, B. D.; Hill, E. W.; Novoselov, K. S.; Watanabe, K.; Taniguchi, T.; Geim, A. K.; Blake, P. Hunting for monolayer boron nitride: optical and Raman signatures. *Small* **2011**, *7*, 465-468.
26. Dresselhaus, M. S.; Jorio, A.; Hofmann, M.; Dresselhaus, G.; Saito, R. Perspectives on carbon nanotubes and graphene Raman spectroscopy. *Nano Lett.* **2010**, *10*, 751-758.

27. Sutter, P.; Lahiri, J.; Albrecht, P.; Sutter, E. Chemical vapor deposition and etching of high-quality monolayer hexagonal boron nitride films. *ACS Nano* **2011**, *5*, 7303-7309.
28. Chae, S. J.; Güneş, F.; Kim, K. K.; Kim, E. S.; Han, G. H.; Kim, S. M.; Shin, H.-J.; Yoon, S.-M.; Choi, J.-Y.; Park, M. H.; Yang, C. W.; Pribat, D.; Lee, Y. H. Synthesis of large-area graphene layers on poly-nickel substrate by chemical vapor deposition: wrinkle formation. *Adv. Mater.* **2009**, *21*, 2328-2333.
29. Yoon, D.; Son, Y.-W.; Cheong, H. Negative thermal expansion coefficient of graphene measured by Raman spectroscopy. *Nano Lett.* **2011**, *11*, 3227-3231.
30. Yates, B.; Overy, M. J.; Pirgon, O. The anisotropic thermal expansion of boron nitride: I. experimental results and their analysis. *Philos. Mag.* **1975**, *32*, 847-857.
31. Meyer, J. C.; Chuvilin, A.; Algara-Siller, G.; Biskupek, J.; Kaiser, U. Selective sputtering and atomic resolution imaging of atomically thin boron nitride membranes. *Nano Lett.* **2009**, *9*, 2683-2689.
32. Girit, Ç. Ö.; Meyer, J. C.; Erni, R.; Rossell, M. D.; Kisielowski, C.; Yang, L.; Park, C.-H.; Crommie, M. F.; Cohen, M. L.; Louie, S. G.; Zettl, A. Graphene at the edge: stability and dynamics. *Science* **2009**, *323*, 1705-1708.
33. Kim, S. M.; Hsu, A.; Araujo, P. T.; Lee, Y.-H.; Palacios, T.; Dresselhaus, M.; Idrobo, J.-C.; Kim, K. K.; Kong, J. Synthesis of patched or stacked graphene and hBN flakes: a route to hybrid structure discovery. *Nano Lett.* **2013**, *13*, 933-941.
34. Kim, C. S.; Korzeniewski, C.; Tornquist, W. J. Site specific co-adsorption at Pt (335) as probed by infrared spectroscopy: Structural alterations in the CO adlayer under aqueous electrochemical conditions. *J. Chem. Phys.* **1994**, *100*, 628-630.
35. Sutter, P.; Sadowski, J. T.; Sutter, E. Graphene on Pt (111): Growth and substrate interaction. *Phys. Rev. B* **2009**, *80*, 245411.
36. Oshima, C.; Nagashima, A. Ultra-thin epitaxial films of graphite and hexagonal boron nitride on solid surfaces. *J. Phys. Condens. Matter* **1997**, *9*, 1-20.

Chapter 4: Fabrication of Size-Controlled Uniform Graphene Quantum Dots Embedded in Monolayer Hexagonal Boron Nitride Using Conversion Reaction on Platinum Nanoparticles

4.1 Abstract

Many approaches such as hydrothermal cutting, electrochemical process for exfoliation, nanolithography, and stepwise organic syntheses have been developed to fabricate graphene quantum dots (GQDs). However, they are time-consuming and costly, and furthermore, precise control over the morphology and size distribution of GQDs remains challenging. Here, we demonstrate spatially controlled conversion of hexagonal boron nitride (h-BN) to graphene on an array of Pt nanoparticles (NPs) to realize an array of uniform GQDs embedded in a h-BN sheet. A uniform Pt NP array was formed on a SiO_2/Si substrate with the aid of self-patterning diblock copolymer micelles, and the h-BN sheet was transferred on the Pt NPs array, followed by the conversion of h-BN on Pt to GQDs. The size of the obtained GQDs corresponded with the sizes of the Pt NPs, because of the selective conversion of h-BN on top of Pt NPs. Uniform and precisely controlled size of the GQDs ranging from 7 to 13 nm was achieved. We grow graphene quantum dots (GQD) inside the matrix of hexagonal boron nitride (h-BN), which allows a dramatic reduction of the number of localized edge states along the perimeter of the quantum dots due to the similar lattice structure of graphene and h-BN. We used such GQDs embedded in h-BN as part of van der Waals heterostructures to produce vertical single electron tunneling transistors operating in Coulomb blockade regime, which opens even larger flexibility when designing future devices.

4.2 Introduction

Graphene quantum dots (GQDs) have received tremendous attention owing to the quantum confinement and functionalization effects, which enable control over their bandgap and improve the quantum efficiency in nanoscale optoelectronic devices. GQDs are typically fabricated by top-down methods including hydrothermal cutting and chemical exfoliation from bulk graphite.[1-3] These methods are simple and enable mass production because of the good solubility of GQDs in various solvents. However, they do not allow a precise control over the morphology and size distribution of the GQDs. To overcome this limitation, electron beam lithography was employed to etch graphene sheets on the

substrate to obtain specific sizes (30–250 nm).[4-7] Although the size can be controlled with a very high precision by e-beam lithography, fabrication of GQD arrays by this process requires very specialized equipment and is time-consuming, and it is not easy to produce the GQDs with sizes below 20 nm because of the limitations of the technique. Meanwhile, Lee *et al.* reported size-controlled fabrication of uniform GQDs with sizes ranging from 10 to 20 nm using a silicon nanoparticles (NPs) array as an etch mask on CVD-grown graphene films.[8] However, this method induced the oxygen functionalization during O_2 plasma treatment for etching, thereby leading to blue photoluminescence (PL) from sp^2 sub-domains isolated by oxygen-based functional groups in GQDs. Thus, it has been challenging to control the size and array of GQDs, to obtain well-defined structures to identify and study their intrinsic properties such as quantum confinement without the functionalization effects.

Hexagonal boron nitride (h-BN), a two-dimensional (2D) insulator with a large bandgap, is a suitable matrix for embedding GQDs owing to the small lattice mismatch (~2%) between graphene and h-BN, as it can protect the edges of GQDs from the functionalization effect. In fact, it is well-known that h-BN can be assembled with graphene in in-plane 2D heterostructures which has been successfully achieved by patterned regrowth,[9-11] heteroepitaxial growth,[12-14] and conversion reactions.[15, 16] Recently, graphene nanoribbons (GNRs) embedded on h-BN sheets were realized though a templated growth method using h-BN trenches.[17] The embedded GNR channels showed bandgap opening (>0.4 eV) and excellent electronic properties (on-off ratio: $>10^4$, carrier mobility: ~750 cm^2/V s) even at room temperature. However, in case of zero-dimensional GQDs, although there are several theoretical studies to estimate their stable electronic and magnetic properties without the edge effect[18-20], there have been no experimental studies. Moreover, it is important to embed GQDs in h-BN sheets so as to observe the quantum confinement depending on the size of the GQDs by passivating the GQD edges with the insulating material.

In this study, we fabricated arrays of uniform GQDs embedded in h-BN sheet via spatially controlled conversion of h-BN on Pt NPs arrays. Uniform Pt NPs were formed on a SiO_2/Si substrate using self-patterning micelles of a diblock copolymer on which h-BN films were transferred before carrying out the conversion reaction to obtain GQD. This method not only enables the fabrication of size-controllable GQDs depending on the size-scale of Pt NPs, but also allows the formation of GQD edges effectively passivated with h-BN. We would like to stress that our method allows the formation of GQDs of arbitrary shape, and also can be extended to the building of other structures and devices. We then used h-BN tunneling barrier and graphene electrodes in order to form contacts to such quantum dots, creating single electron tunneling transistors. Such method results in very precise, reproducible contact resistance, and the graphene-h-BN interface free of localized states.

4.3 Experimental Section

4.3.1 Growth of Graphene Quantum Dots Embedded in h-BN Sheet

The single layer of hexagonal boron nitride (h-BN) is synthesized on Pt foil using ammonia borane as a precursor using a chemical vapor deposition (CVD) method. Experimental details on the synthesis of CVD-grown h-BN on Pt can be found in a previous report.[21] The Pt nanoparticle (NPs) array on a SiO_2 substrate was prepared using self-patterning diblock copolymer micelles.[22] A monolayer of polystyrene-block-poly(4-vinylpyridine) (PS-P4VP) micelles with H_2PtCl_6, a precursor of Pt NPs, in their cores was spin-coated on the SiO_2 substrate. To fabricate the Pt NP array, the micellar film on the SiO_2 was annealed at 400 °C for 30 min in air. The h-BN films were transferred onto the Pt NPs/SiO_2 substrate using a wet-transfer method (electrochemical delamination). Then, the h-BN transferred on Pt NPs/SiO_2 was loaded into the center of a vacuum quartz tube in a furnace for the conversion reaction. The tube was pumped down to 0.21 Torr with pure Argon gas (50 sccm). Then the furnace was heated to 950 °C in 40 min. When the reaction starts, methane gas (5 sccm) with Argon (50 sccm) was flown as the source for graphene growth. During the reaction, the h-BN region on the Pt NPs was converted to graphene, and after 10 min of growth, a uniform GQD array embedded in h-BN film was obtained.

The GQD/h-BN film on Pt NPs/SiO_2 could be transferred onto any other substrate via a wet-transfer method using HF and an aqua regia solution. First, polystyrene (PS) was spin-coated on the sample, and it was immersed in a HF solution (5% in DI water) to remove the SiO_2 layer. Then, the floating PS film was transferred to the aqua regia solution (3:1 mixture of hydrochloric acid and nitric acid) to remove Pt NPs. Finally, the film was transferred onto the target substrate and the PS film was removed with toluene to obtain a GQD/h-BN film on the substrate.

4.3.2 Characterization of GQD/h-BN Heterostructure

Scanning electron microscopy (Verios 460, FEI) and atomic force microscopy (Dimension Icon, Bruker) were used to determine the surface morphology of the samples. Raman and PL spectra were measured using a micro Raman spectroscope (alpha 300, WITec GmbH) using 532-nm and 266-nm lasers, respectively. The UV-vis absorption spectra of the GQD/h-BN samples were recorded on a Cary 500 UV-vis-near IR spectroscope, Agilent. X-ray photoelectron spectroscopy (K-Alpha, Thermo Fisher) and Nano-FTIR (neaSNOM, neaspec) were performed to determine the composition of the GQD and confirm the formation of an interface between GQD and h-BN. Low voltage Cs aberration-corrected transmission electron microscopy (Titan Cube G2 60-300, FEI), operated at 80 kV with a

monochromated electron beam, was used for electron energy loss spectroscopy (EELS) analysis. The spatial resolution and energy resolution for EELS measurement are 0.2 nm and 0.25 eV, respectively.

4.3.3 Device Fabrication of Single Electron Tunneling Transistor

The electrical response of the graphene quantum dots (GQDs) embedded in monolayer h-BN was investigated by assembling vertical tunnel van der Waals heterostructures consisting of the stack of Si/SiO_2/30nm_h-BN/Gr/2h-BN/GQD/2h-BN/Gr/20nm_h-BN. Here, the bottom and top layers of h-BN were used for the purpose of encapsulation. As the GQDs are embedded in the large area monolayer h-BN on SiO_2/Si, the vertical heterostructure was assembled in two halves by adopting a mix of dry and wet flake transfer procedure: first, a stack of Si/SiO_2/~30 nm h-BN/Gr/h-BN was prepared by standard flake exfoliation and dry transfer procedure. To prepare the other half, a stack of 2L h-BN/Gr/ ~20 nm h-BN was prepared by the dry pick up procedure using a PMMA membrane. This stack on the membrane was aligned and dropped on the GQDs h-BN/SiO_2/ Si substrate. To release the stack from Si/SiO_2, 8% PMMA was spun on the sample and Si/SiO_2 was etched using KOH solution. The floated membrane was thoroughly rinsed with DI water several times to remove KOH residues from the membrane. Finally, to complete the device, this membrane containing GQDs/2L h-BN/Gr/~20nm h-BN was dropped on the stack prepared in the first half.

For electrical characterization of this vertical heterostructure, Cr/Au edge contacts were made on the top and bottom graphene layers using electron beam lithography followed by boron nitride etching, metal deposition, and lift-off process.

4.4 Results and Discussion

4.4.1 Fabrication and Surface Characterization of GQD/h-BN In-Plane Heterostructure

We developed a method for fabricating in-plane graphene/h-BN heterostructures using a conversion reaction on a patterned Pt-SiO_2 substrate.[16] Based on the spatially controlled conversion, the growth of in-plane GQD/h-BN heterostructure was achieved on the Pt nanoparticle (NP) array on the SiO_2 substrate, as illustrated in Figure 1. The h-BN film was first grown on Pt foils via a chemical vapor deposition (CVD) method using ammonia borane as the precursor.[21] The experimental details for the growth and the characterization of monolayer h-BN are provided in the experimental section and Figure 2. For the fabrication of GQD/h-BN, the h-BN film was transferred onto the Pt NP array on the SiO_2 substrate prepared with the aid of self-patterning diblock copolymer micelles.[22] Pt NPs were obtained by spin-coating a monolayer of polystyrene-block-poly(4-vinylpyridine) (PS-P4VP) micelles with H_2PtCl_6, the precursor for Pt NPs within their cores, followed by annealing at 400 °C. Then, the conversion of the h-BN sheet to graphene on the array of Pt NPs on the SiO_2 substrate was accomplished at ~950°C in methane/argon atmosphere. During the reaction, the h-BN on top of Pt NPs was selectively converted to graphene, with the formation of uniform GQD arrays embedded in the h-BN film (Figure 3). Notably, depending on the molecular weight of the diblock copolymer, the size of the Pt NPs was controlled in the range of 7 to 13 nm. The scanning electron microscopy (SEM) image presented in Figure 4a-c demonstrates the uniform arrays of Pt NPs with diameters of ~7, 10, and 13 nm. Next, the as-prepared GQD/h-BN in-plane heterostructure was placed in aqua regia solution to remove Pt NPs (Figure 4g-I), and finally, transferred onto arbitrary substrates for further characterization and processing. Note that the area of obtained GQDs is comparable to the size of the Pt NPs, as shown in Figure 4. The removal of the Pt NPs was confirmed by TEM and XPS (Figure 5-6)

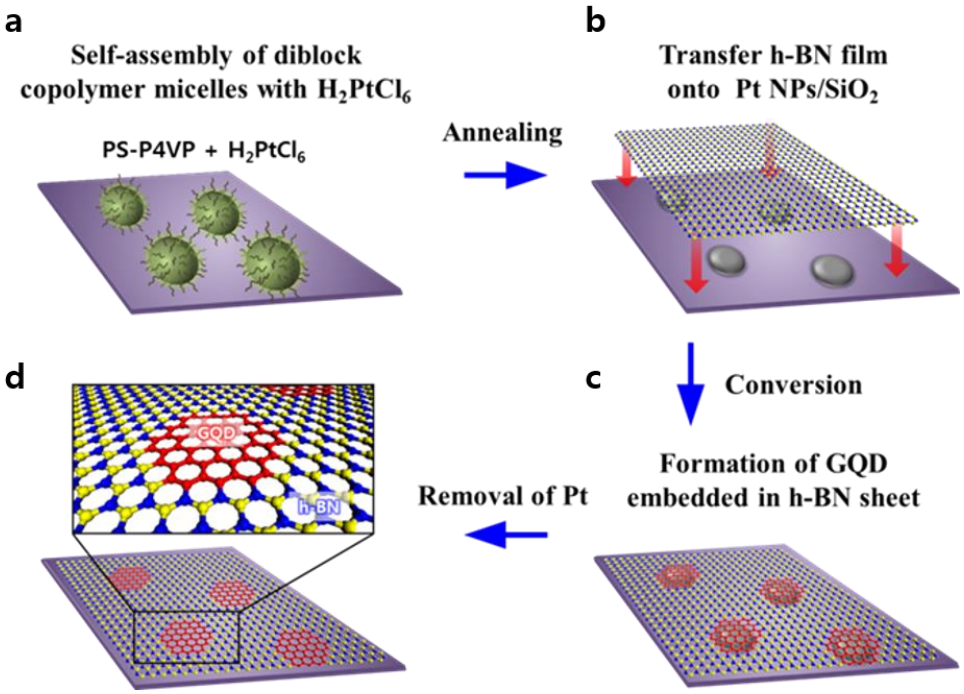

Figure 1. The fabrication steps of GQD/h-BN in-plane heterostructure based on h-BN to graphene conversion catalyzed by Pt NPs supported by a substrate of SiO_2. (a) The self-assembly of diblock copolymer micelles PS-P4VP with H_2PtCl_6 on Si/SiO_2 substrate. (b) Transfer of h-BN monolayer on SiO_2 substrate covered by Pt NPs (blue spheres – boron atoms, yellow spheres - nitrogen). (c) Formation of the GQDs on top of an array of Pt NPs by catalytically-assisted CVD (red spheres – carbon atoms). (d) The obtained in-plane GQD/h-BN heterostructure after the removal of Pt NPs.

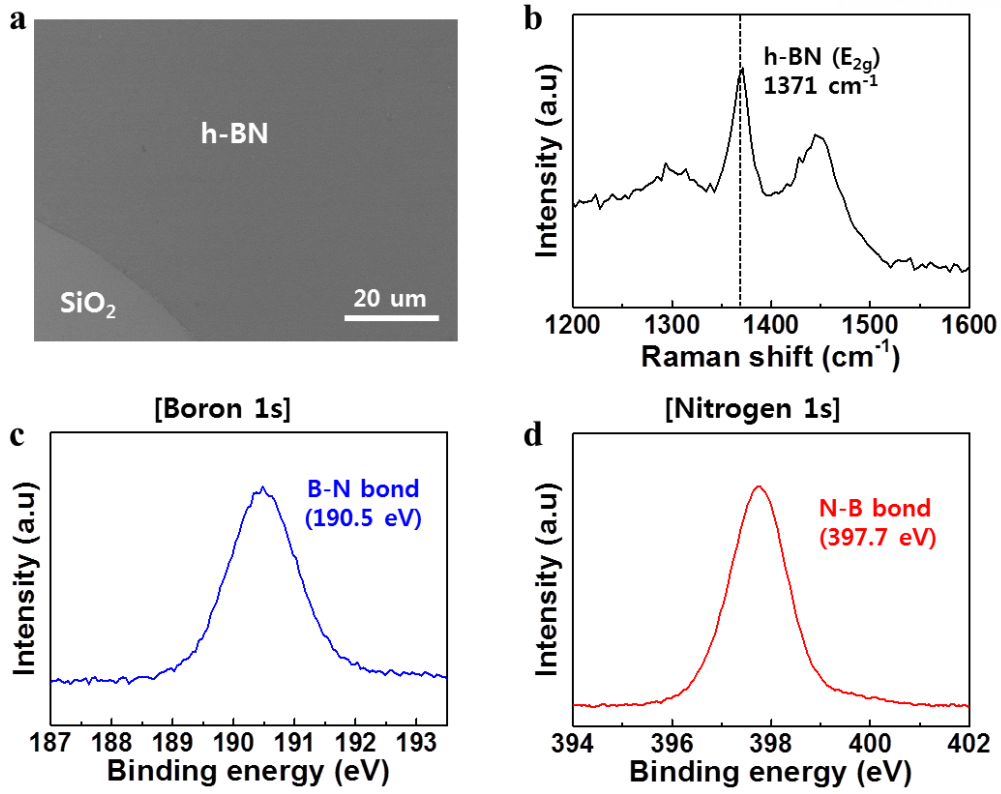

Figure 2. (a-b) The SEM image and Raman spectrum of the CVD grown pristine h-BN monolayer. (c-d) The corresponding XPS spectra: (c) Boron 1s, and (d) Nitrogen 1s.

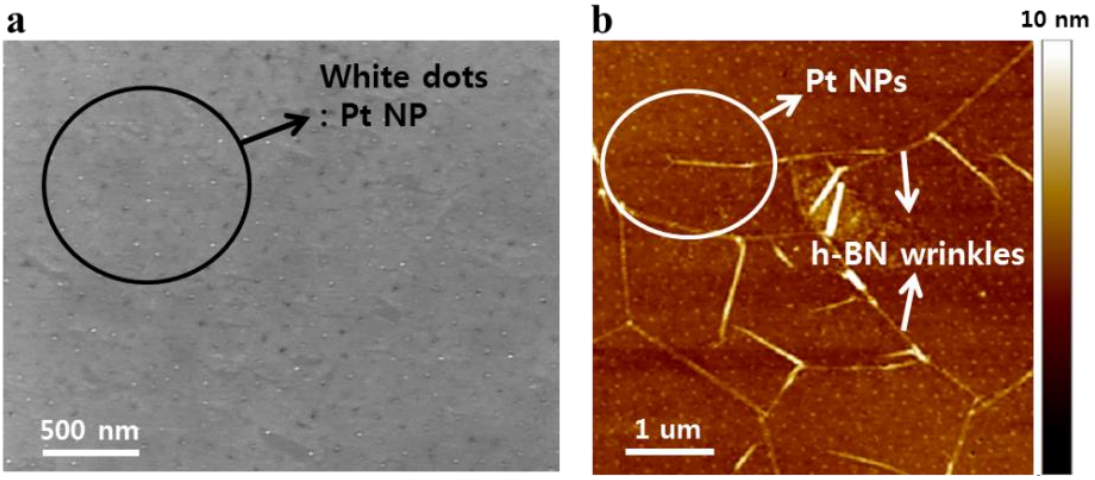

Figure 3. (a-b) The SEM and AFM images of the as-grown layer of GQD/h-BN on an array of Pt NPs (7 nm) spread over SiO_2 substrate.

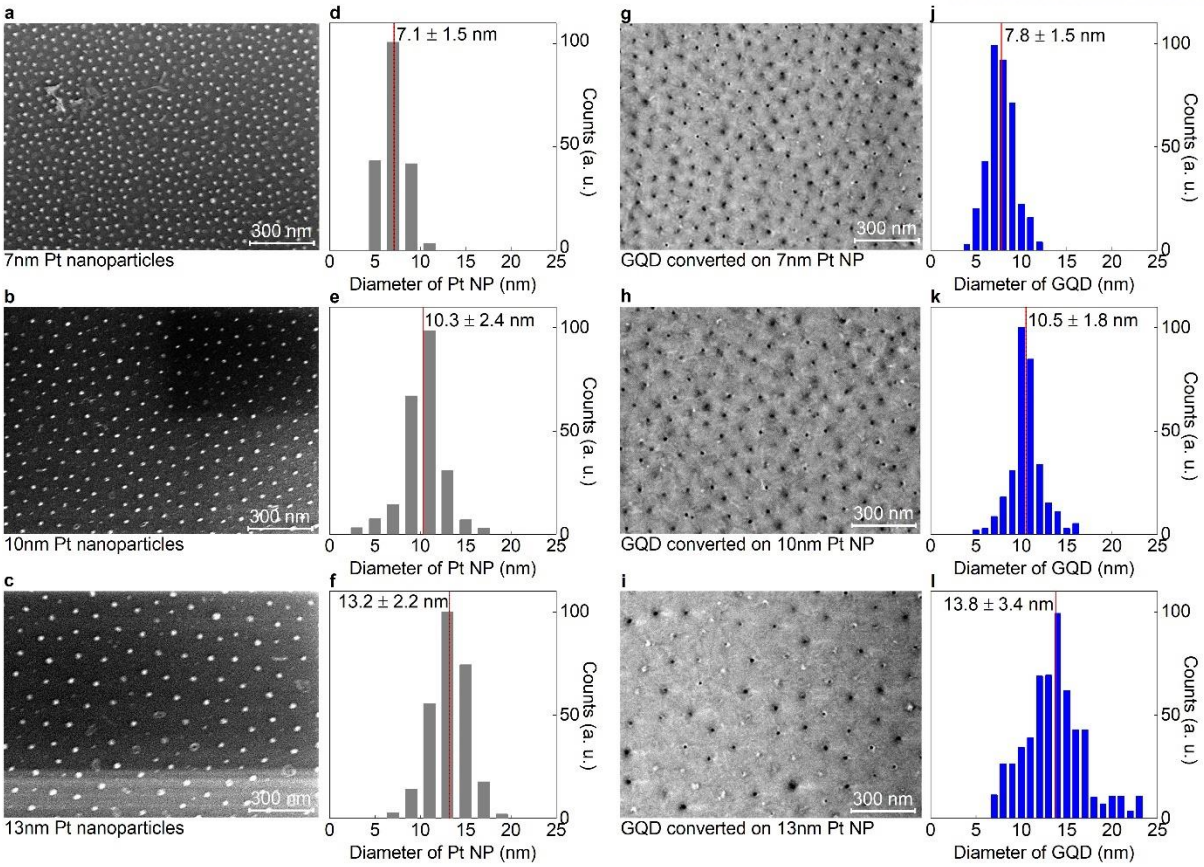

Figure 4. Size and spatial distribution of the GQDs. (a-c) The SEM images of 7, 10, and 13 nm sized arrays of Pt NPs on SiO_2 substrates, respectively. (d-f) Corresponding size distribution histograms of Pt NPs on SiO_2 substrates. Numbers give the average (marked by red lines) and the standard deviation. (g-i) The SEM images of GQD/h-BN samples prepared on pristine SiO_2. (j-l) Corresponding size histograms of GQD/h-BN samples. Numbers give the average (marked by red lines) and the standard deviation.

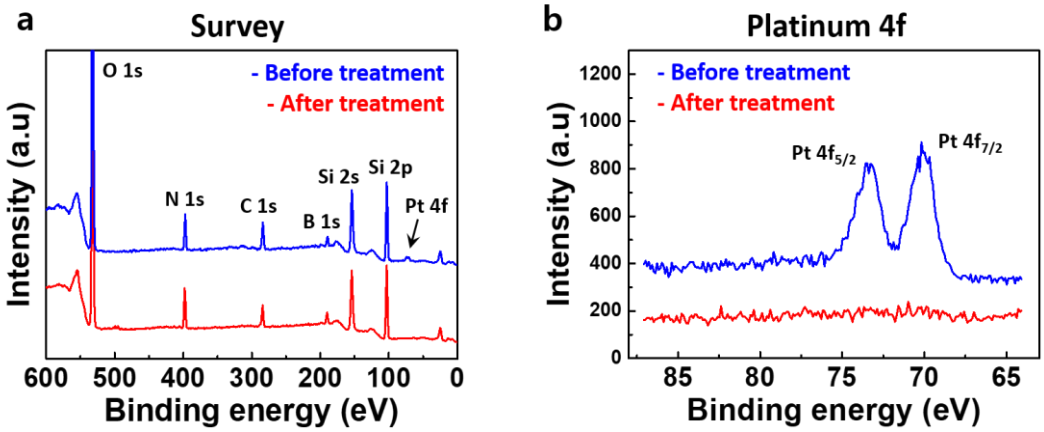

Figure 5. The XPS spectra of GQD/h-BN planar heterostructure on SiO_2 substrate. (a) Survey, and (b) Pt 4f spectra. Blue and red spectra are for as-prepared GQD/h-BN on Pt NPs/SiO_2 substrate (before the aqua regia treatment) and the GQD/h-BN after the aqua regia treatment to remove Pt NPs, respectively.

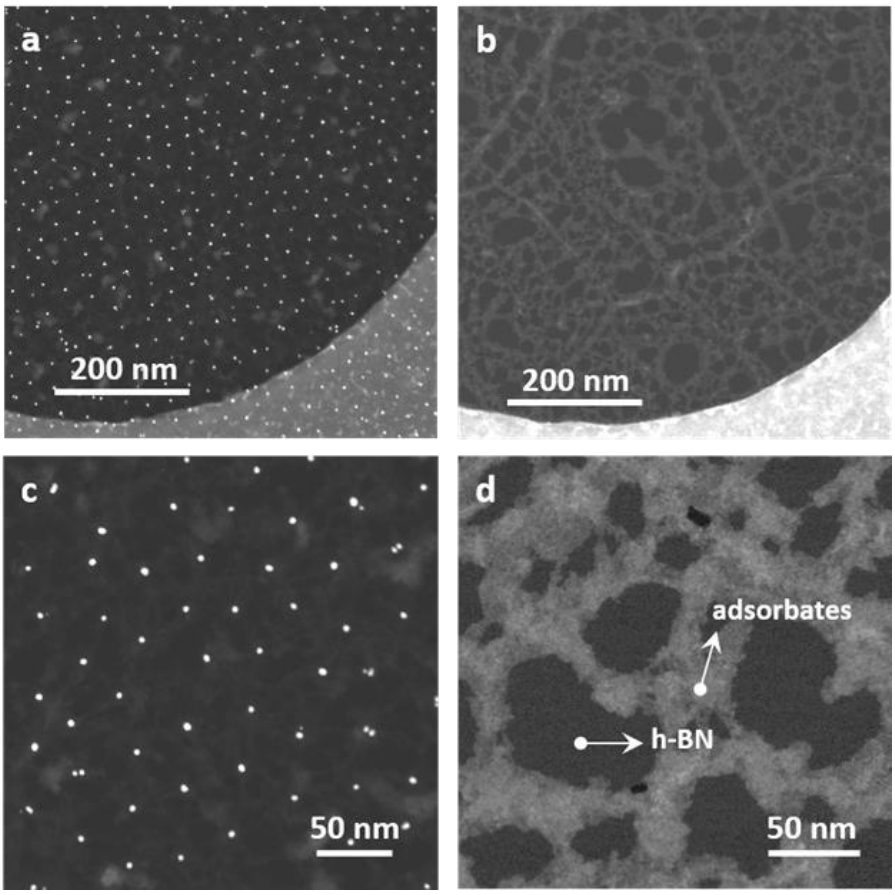

Figure 6. TEM images of GQD/h-BN. (a, c) Pt NPs on top of GQD/h-BN. (b, d) The GQD/h-BN after aqua regia treatment. The white dots in (a,c) are Pt NPs.

The formation of GQDs was confirmed by the Raman (Figure 7a) and EELS (Figure 8) spectroscopy. Typical Raman signals of GQDs and h-BN were observed from the in-plane heterostructure of GQD/h-BN transferred onto a SiO_2 substrate: the D (1345 cm^{-1}) and G (1595 cm^{-1}) bands of graphene with an intervening E_{2g} peak (1371 cm^{-1}) of an h-BN. Furthermore, the in-plane graphene domain size (L_a) was calculated using the ratio of the integrated intensity (I_D/I_G) according to the Tuinstra-Koenig relation[23] (Table 1), and is consistent with the size of GQDs, observed by SEM image (Figure 4). The formation of GQD/h-BN heterostructures was also confirmed EELS mapping (Figure 8). The boron signal was not detected at P4 to P7 where the Pt NP exist. Note that the points P5 and P6 with strong signal is due to strong background of Pt signal because we could not completely subtract the strong Pt background. Note that boron signal is absent in P5 and P6 (see panel g). In the nitrogen mapping image, the N signal is too low to be detected[21]. The EELS spectra were obtained at different positions (yellow line, P1 to P10) with 2 nm spatial resolution in f by subtracting the background of the Pt signal from the original EELS spectra. The peak for Boron is not detected in P4, P5, P6, and P7, indicating conversion of BN to graphene. Note that GQDs in c and g are not distinguishable from carbon signal of many adsorbates.

In order to characterize the interface between GQD and h-BN in the heterostructure, we performed X-ray photoelectron spectroscopy (XPS) and the spectra are shown in Figure 7b–d. The XPS B 1s peak in Figure 7b can be deconvoluted into two peaks at 189.7 eV and 190.4 eV, respectively. The XPS peak of B-N bond (190.4 eV) is very close to the measured value for B 1s (190.5 eV) in the as-grown h-BN transferred onto the SiO_2 substrate (Figure 2c). Further, the peak at the lower binding energy (189.7 eV) corresponds to B-C bonding[24]. The N 1s peak in Figure 7c can also be deconvoluted into two peaks corresponding to N-B bond (397.5 eV) and N-C bond (398.2 eV)[24]. Furthermore, the peaks of C-B (283.2 eV) and C-N bond (285.0 eV) are confirmed in the XPS C 1s spectrum (Figure 7d). The ratio of each deconvoluted peak in the C 1s spectrum (Table 2) is 22.2% (C-B bond) : 58.9% (C-C bond): 18.9% (C-N bond). This suggests that C-B bonds are more energetically favorable at the interface than C-N bonds owing to the difference in the binding energies ($E_{b,C-B}$: 0.45 eV and $E_{b,C-N}$: 0.41 eV),[13] as shown in Figure 9. In addition, we confirmed the C-N mode at 1273 cm^{-1} and the B-N mode at 1375 cm^{-1} in the measured infrared (IR) spectra of the GQD/h-BN sample (Figure 10). However, the B-C bond, which is expected to appear at approximately 1020 cm^{-1},[24] was not identified because of a very strong SiO_2 peak. These XPS and IR results provide evidence on the formation of an interface between them. Due to the small size of our quantum dots the lattice mismatch between graphene and h-BN is not expected to lead to the formation of dislocations as in the case of bulk graphene/h-BN planar heterostructures[25].

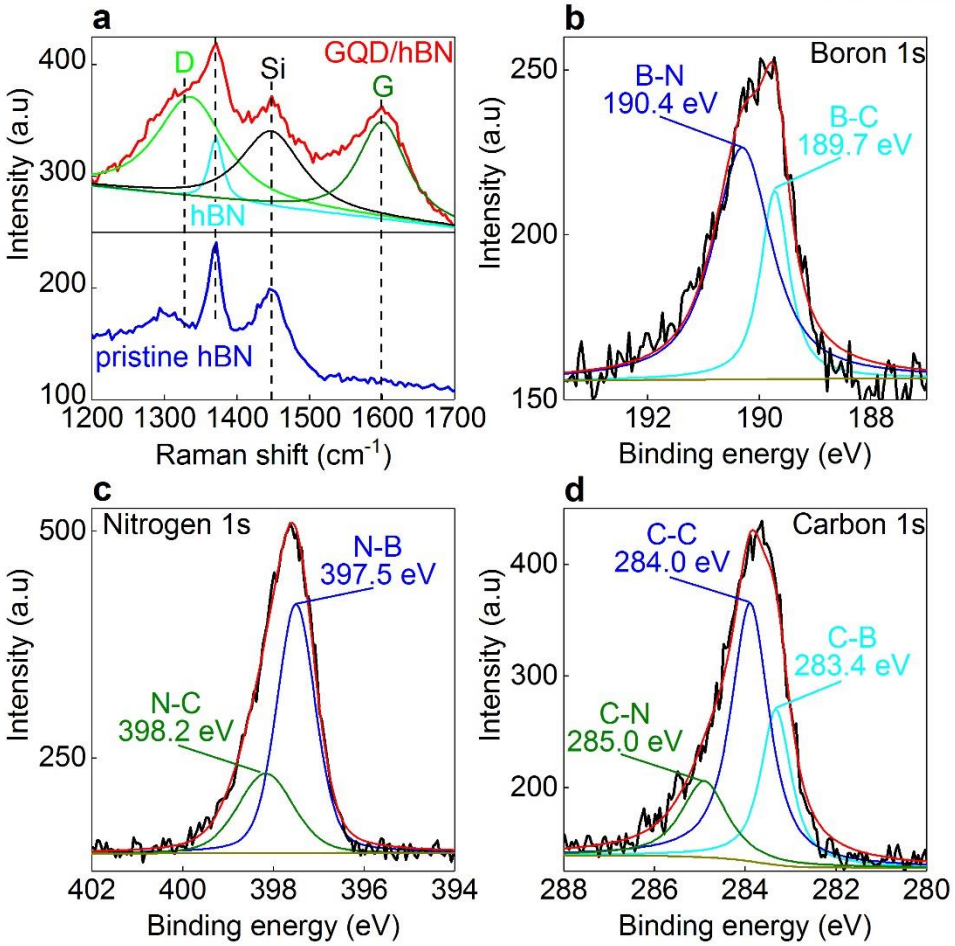

Figure 7. Characterization of GQD/h-BN interface of the in-plane heterostructure with GQDs of the size of 7 nm. (a) Raman spectra of GQD/h-BN planar heterostructure (red) and pristine h-BN (blue). XPS spectra of GQD/h-BN planar heterostructure: (b) boron 1s, (c) nitrogen 1s, and (d) carbon 1s spectrum.

Size of GQD (nm)	L_a (nm)
7 nm	8.98 nm
10 nm	10.12 nm
13 nm	11.79 nm

$$L_a(\mathrm{nm}) = (2.4 \times 10^{-10})\lambda_l^4\left(\frac{I_D}{I_G}\right)^{-1}$$

Table 1. Graphitic domain size. The integrated intensity ratio, I_D/I_G, was used to determine the in-plane crystallite size L_a (nm) using the Tuinstra-Koenig relationship[24], where λ is the wavelength of Raman excitation (532 nm).

Peak	Bonding	Binding energy (eV)	Ratio (%)
Boron 1s	B-C	189.7	31.9 %
	B-N	190.4	68.1 %
Nitrogen 1s	N-B	397.5	73.2 %
	N-C	398.2	26.8 %
Carbon 1s	C-B	283.2	22.2 %
	C-C	284.0	58.9 %
	C-N	285.0	18.9 %

Table 2. The proportion of the respective bonds in Figure 7b-c.

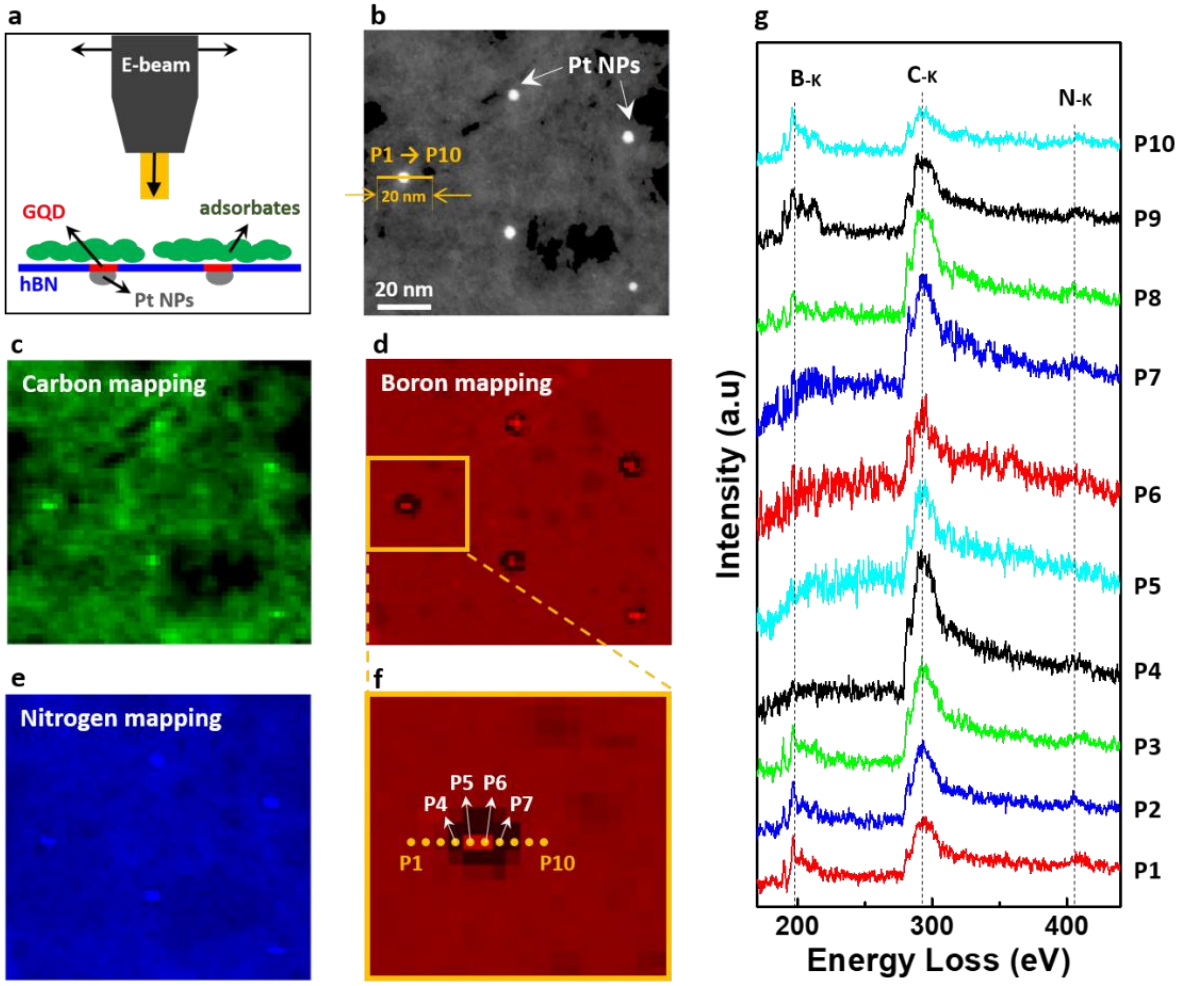

Figure 8. EELS analysis of GQD/h-BN. (a) Schematics of EELS mapping of GQD/h-BN on Pt NPs/SiO_2. (b) TEM image of GQD/h-BN on Pt NPs. The white dots are 7 nm Pt NPs. (c-e) Corresponding EELS mapping images of (c) carbon, (d) boron, and (e) nitrogen, respectively. (f) Magnified image marked in (d). (g) The EELS spectra were obtained at different positions (yellow line, P1 to P10) with 2 nm spatial resolution in f by subtracting the background of the Pt signal from the original EELS spectra.

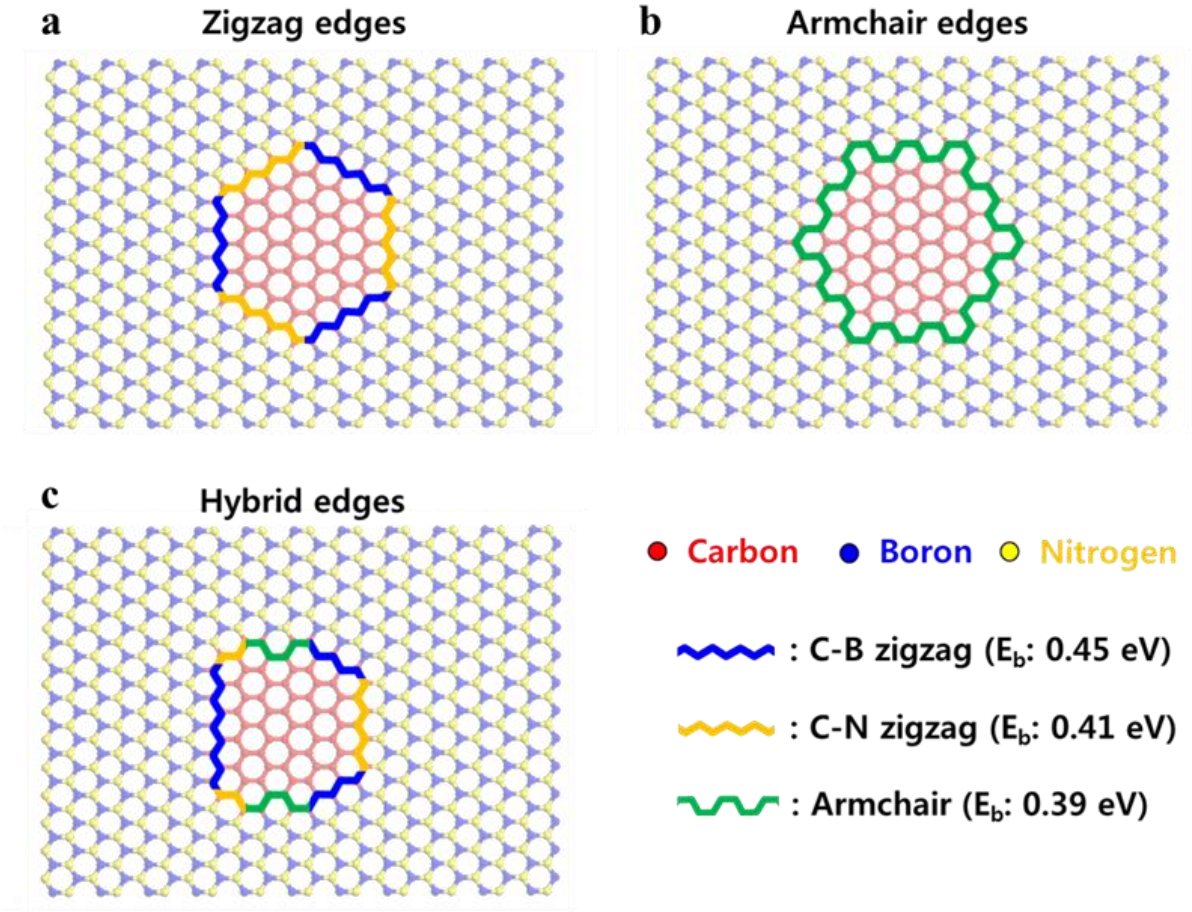

Figure 9. Scheme of ideal GQD/h-BN heterostructures with (a) zigzag and (b) armchair edges. (c) Estimated heterostructures with more C-B zigzag bonds compared to the C-N zigzag bonds. The binding energies for C-B zigzag, C-N zigzag, and armchair bond in the graphene/h-BN in-plane heterostructure are calculated to be 0.45, 0.41, and 0.39 eV, respectively, by DFT calculations[13].

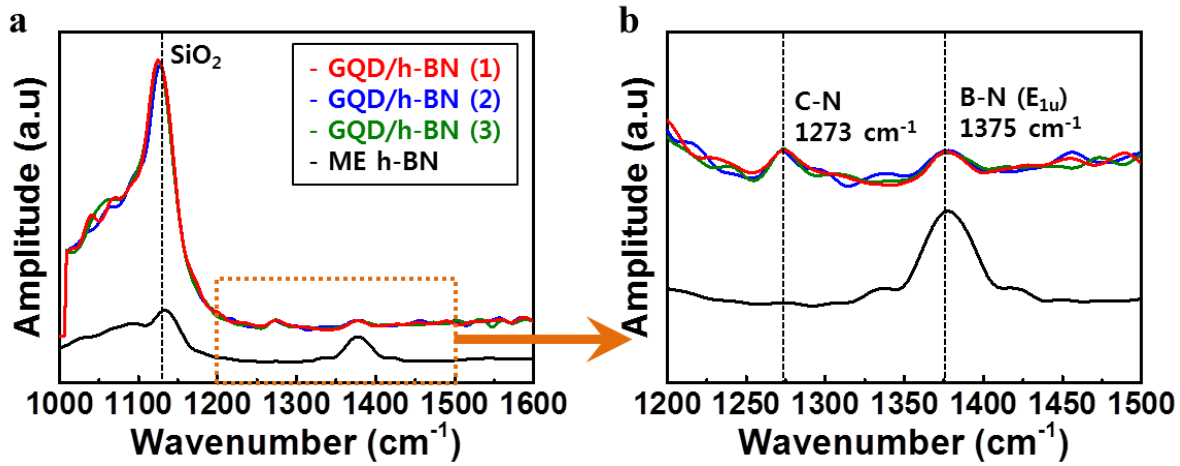

Figure 10. (a) The measured IR spectra for the GQD/h-BN and mechanical exfoliated h-BN (2 nm thickness) on SiO_2 by AFM-IR. Three spectra on different points were measured for a GQD/h-BN sample. (b) Magnified spectra in the range from 1200 to 1500 cm^{-1}.

4.4.2 Photoluminescence Emission on GQD/h-BN Heterostructure

The emission colors of GQDs from various synthetic methods range from blue to yellow (400–650 nm) in the visible region.[2, 26-30] However, the mechanism of PL emission has not been appropriately investigated, with several factors such as the size effect on quantum confinement[26, 27] and edge effect by various functional groups[2, 28-30] remaining not completely understood. In this regard, the structure of our GQDs embedded in the insulating h-BN is unique to observe the quantum confinement depending on the sizes of the GQDs due to the passivation of the GQD edges by the h-BN sheets. In order to confirm the optical properties of the heterostructure, UV-vis absorption and PL measurements were performed on quartz and SiO_2 substrates, respectively. The UV-vis spectra (Figure 11a) of the GQD/h-BN heterostructure shows the typical absorption band of h-BN located at 200 nm and those of GQDs at 263 nm and 330 nm ($\pi \rightarrow \pi^*$ transition),[2] respectively, confirming the existence of both h-BN and the GQD formed through the spatially controlled conversion. Figure 11b presents the corresponding PL spectra of the 7, 10, and 13 nm sized GQD/h-BN heterostructures under excitation with a 266 nm laser. New PL emission peaks at 407, 411, and 420 nm, respectively, are observed. Theoretically, the PL wavelengths corresponding to 7, 10, and 13 nm GQDs are located in the far-IR range owing to the size effect of quantum confinement.[31] It is noted that absorption and PL studies on our GQD/h-BN were not carried out in the IR range, but we confirm the size effect of the GQD induced by quantum confinement by measuring the Coulomb blockade, as discussed in the following section.

In order to understand the mechanism of PL in detail, we performed PL measurements on several control samples. It is noted that no PL peaks (Figure 12) are observed from bare Pt NPs on SiO_2 substrate (black) and bare h-BN on SiO_2 substrate (green), and also from a control sample obtained by carrying out the conversion reaction without the Pt NPs, indicating that the PL results from the in-plane heterostructure of GQD and h-BN. We consider three possible origins for PL from the hybrid structure of GQD and h-BN: First, the PL may originate from the edge effect due to oxidation[2] or sp^2 sub-domains created by oxygen-functional groups inside the GQDs[8, 32] during the aqua regia treatment or growth process (Figure 13). Second, with respect to the h-BN material, the GQD/h-BN heterostructure consists of nano-sized holes of h-BN, which may be one of the origins of the PL[33-35] (Figure 14). Third, the PL can be due to new energy levels generated from the graphene edges connected with h-BN.[35]

Previous studies reported that 10 nm-sized GQDs can yield PL emission at ~ 400 nm due to edge effect by oxidation[2] and the ~ 3 nm sp^2 sub-domains isolated by oxygen-functional group of the quantum dot[8, 32]. In the regard, GQDs in our study may be formed with the oxidized edges or sp^2 sub-domains by oxygen-functional group during the aqua regia treatment or growth process (Origin 1, Figure 13). First,

we measured the PL emission of the GQD/h-BN on Pt NPs/SiO_2 substrate before aqua regia treatment (Figure 13b). We confirmed PL emission at ~ 410 nm wavelength on GQD/h-BN on Pt NPs/SiO_2 (blue spectrum in Figure 13e), even though the PL intensity decreased slightly, showing that the oxidation by aqua regia treatment is not an origin of PL emission. Second, in order to check PL emission of bare GQD without h-BN, the sample was prepared using CVD grown graphene. Bare GQDs were prepared via O_2 plasma etching process by using the Pt NPs array as a pattern mask (Figure 13c).[32] We can easily distinguish the GQD arrays and SiO_2 regions by SEM contrast (Figure 13d). The PL peak (red spectrum) at 400 nm wavelength in Figure 13e was not observed from the bare GQD fabricated by O_2 plasma treatment. Above results indicate that the PL emission in GQD/h-BN is not due to sp^2 sub-domains or edge effect by oxygen functional group.

Several papers reported that the defect points in h-BN sheets have the quantum emission in the 2 ~ 4 eV energy range[33-35] (Figure 14a). In order to check this possibility, the h-BN sheet with nano-sized holes was prepared by using hydrogen-etching of h-BN though the annealing process on Pt NPs in H_2 atmosphere.[16, 36] The CVD-grown monolayer h-BN was transferred onto the Pt NPs/SiO_2 substrate and etched away on Pt NPs by annealing at 700 ^oC in H_2 flow (30 sccm). Figure 14b shows AFM image of hydrogen-etched h-BN film with holes transferred onto SiO_2 substrate. No PL emission of the sample was observed as shown in Figure 14c. Furthermore, as shown in Figure 12b, we did not observe any PL of h-BN on SiO_2 substrate after carrying out the conversion reaction without Pt NPs. Therefore, above results indicate that the PL in GQD/h-BN is not due to nano-sized holes of h-BN nor any defect in h-BN. We confirmed that the PL emission is not due to the oxidized edges and sp^2 sub-domains in the GQDs and nano-sized holes of h-BN by the absence of PL from the control samples. Therefore, we consider that the emission is due to a new localized energy state at the interface region between the GQD and h-BN.

Recently, a theoretical study was reported on the electronic density of states in polycrystalline structures with graphene and h-BN grains.[37] Localized density of states at −1.2 and 2 eV were observed at the interface of graphene and h-BN grains. Further experimental investigations on the contribution of the localized energy states at the interface to PL are required. We performed PL measurements on the in-plane heterostructure of graphene and h-BN (Figure 15). The heterostructure was prepared by a previously reported conversion reaction to fabricate graphene on a Pt substrate.[16] We note that a small PL peak at 410 nm wavelength is observed corresponding to the interface of graphene and h-BN, whereas no PL is observed for graphene only and h-BN only regions, implying that localized energy states are dominantly formed between graphene and h-BN and the PL is due to this interface.

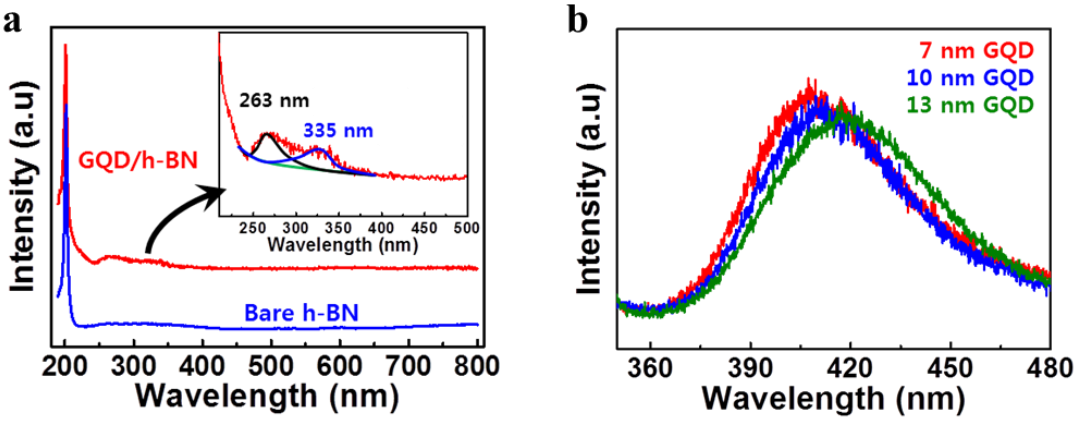

Figure 11. (a) UV-vis absorbance spectra of bare h-bN and GQD/h-BN heterostructure. (b) PL spectra of GQD/h-BN samples prepared on 7 (red), 10 (blue), and 13 nm (green) sized Pt NPs/SiO_2 substrate, respectively.

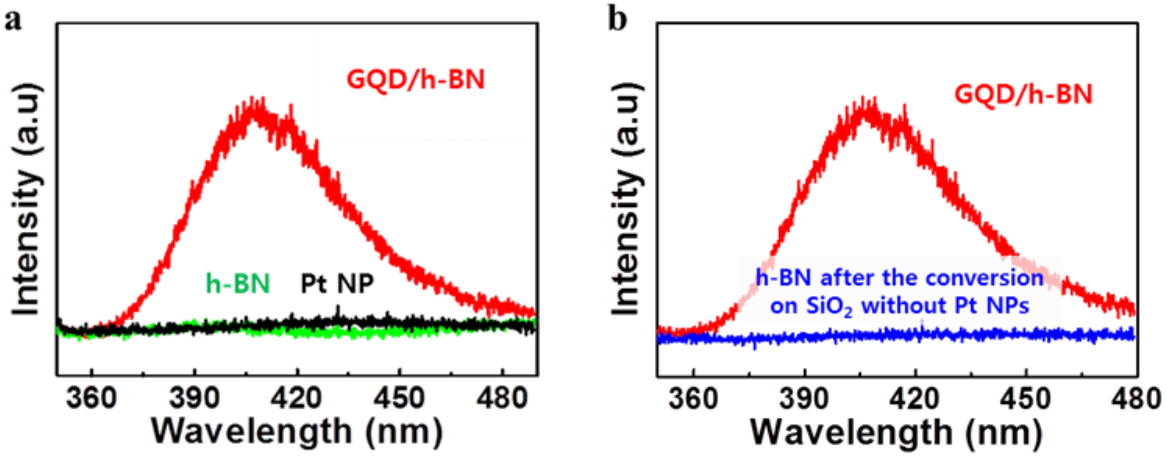

Figure 12. (a) PL spectra of bare h-BN/SiO_2 (green spectrum) and Pt NPs/SiO_2 substrate (black spectrum). (b) PL spectrum of h-BN on SiO_2 substrate (blue spectrum) after carrying out the conversion reaction without Pt NPs in the same condition. The PL spectrum of GQD/h-BN is provided as a reference in (a) and (b).

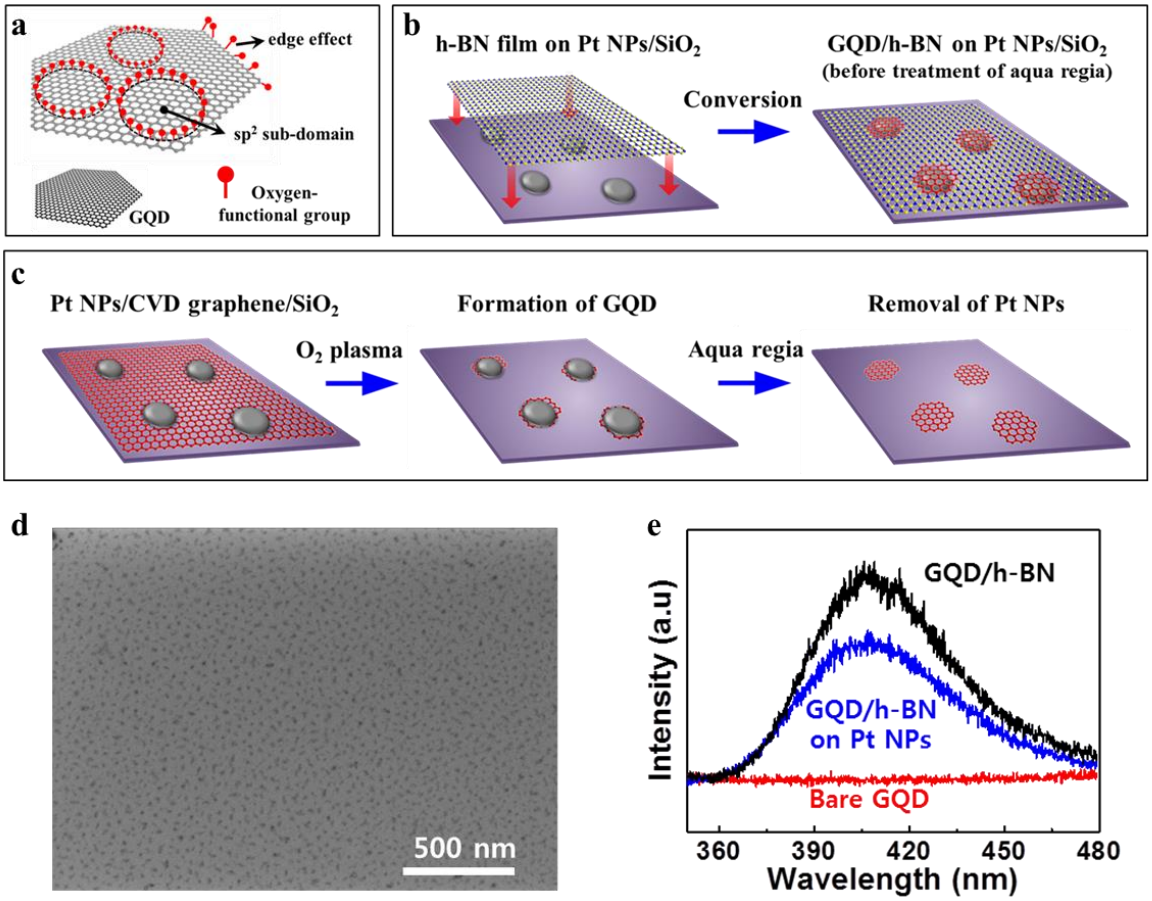

Figure 13. (a) Scheme of GQDs with the oxidized edges and sp^2 sub-domains isolated by oxygen-functional group (Origin 1). (b) Scheme of the fabrication process of as-prepared GQD/h-BN on Pt NPs/SiO_2 substrate before the treatment with aqua regia. (c) Scheme of bare GQD prepared by O_2 plasma treatment of CVD grown graphene. (d) SEM image of a bare GQD (~7 nm) array prepared in (c). (e) PL spectra of bare GQD (red spectrum) and as-prepared GQD/h-BN on Pt NPs/SiO_2 substrate (blue spectrum).

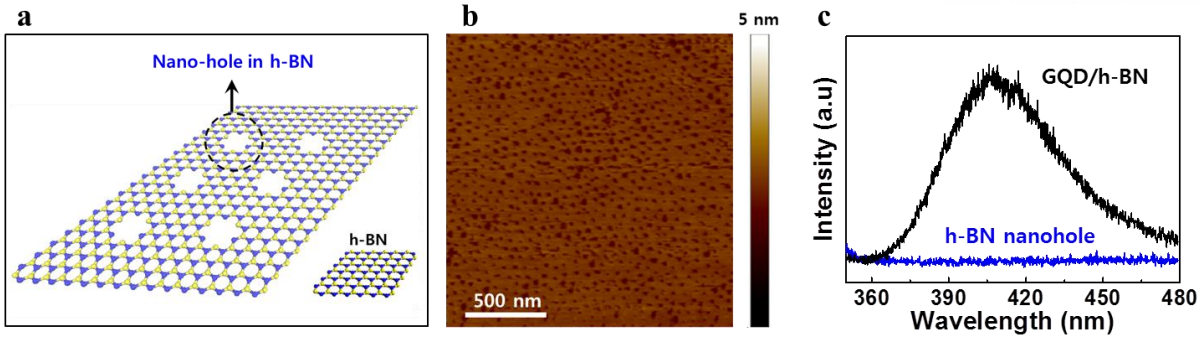

Figure 14. (a) Scheme of h-BN sheets with nano-sized holes. (b) AFM image of h-BN nano-sized holes by annealing process in H_2 atmosphere. (c) PL spectra of h-BN nano-sized hole (blue spectrum).

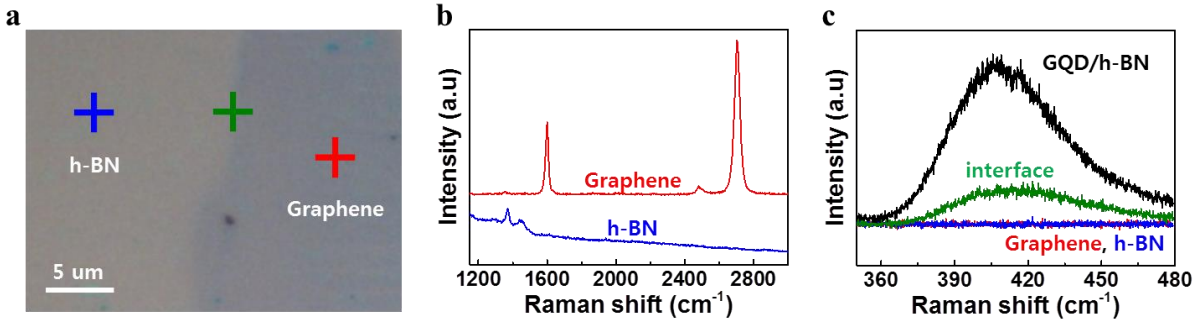

Figure 15. (a) Optical image of in-plane graphene/h-BN heterostructure on SiO_2 substrate.[16] (b) Raman spectra of graphene (red) and h-BN (blue) on SiO_2 substrate by using a 532-nm laser. Integration time: 5 sec (graphene), and 60 sec (h-BN). (c) PL spectra of graphene (red), h-BN (blue), and interface (green) by using a 266-nm laser. The reason for the weak PL intensity is because the fraction of the interface regions in the heterostructure is smaller than in the GQD/h-BN structure.

4.4.3 Single Electron Tunneling Transistor Using GQD/h-BN Heterostructure

Such GQDs embedded in a h-BN matrix are ideally suited for the formation of van der Waals heterostructures[38-40]. To this end, several van der Waals heterostructures Si/SiO_2/30nm_h-BN/Gr/2h-BN/GQD/2h-BN/Gr/20nm_h-BN have been assembled on Si/SiO_2 substrate (acting as a back gate) by using dry transfer method[41] (Figure 16). Here, 30nm_h-BN stands for the h-BN layer with approximate thickness 30 nm, Gr – for graphene, 2h-BN – for 2 layer thick exfoliated h-BN, GQD – for GQD/h-BN lateral heterostructure. Schematic structure and the layer arrangement of our devices is presented on Figure 17a. Devices with two (2h-BN, see Figure 17a) and three (3h-BN) layer thick h-BN tunneling barriers have been produced. For all the layers (apart from the GQD/h-BN layer) mechanically exfoliated crystals have been used. The GQD layer was sandwiched between two thin h-BN layers to isolate the quantum dots from the contacts to ensure a long lifetime of electrons within the quantum dots, thus, to allow the detection of the single electron energy levels. All our devices were fabricated in a symmetric configuration - with the same number of h-BN layers on each side of GQD. In total 6 devices have been measured which produce very similar results.

We performed tunneling spectroscopy on our van der Waals heterostructures at $T = 0.25$ K, by applying a mixed signal of AC and DC bias voltage between the two graphene electrodes and a gate voltage to the silicon substrate[42]. Figure 17 presents a colour map of differential conductance $G\,(V_g, V_b) = dI/dV_b$ as a function of the gate (V_g) and bias (V_b) voltages. Two types of sharp peaks can be identified on top of the smooth background; *(i)* those organized into overlapping diamonds, *(ii)* those which follow square root dependence. We attribute the peaks with square root dependence in $G\,(V_g, V_b)$ to be due to tunneling through impurities and the diamond-shaped features - to Coulomb blockade diamonds due to tunneling through single electron states in individual graphene quantum dots.

Each diamond corresponds to a Coulomb blockade regime in one particular GQD. For a single GQD, one would observe a sequence of diamonds which connect to each other only at vertices. Since we have a large number of GQDs connected in parallel – we observe a number of overlapping diamonds[43]. Because of the technology we used, there are roughly 4 times more 7 nm GQD per unit area than there are 13 nm GQD, thus, there are more overlapping diamonds for 7 nm GQD. The zero-bias conductance within the diamond, Figure 17h is given by the background tunneling through the 5 layer h-BN (2 layers of h-BN on each side of the middle h-BN layer with GQD) and is within the expected range[44], indicating the absence of the pin-holes in the barrier. We also produced devices of the type Si/SiO_2/30nm_h-BN/Gr/2h-BN/CVD h-BN/2h-BN/Gr/20nm_h-BN. In such devices we used the same CVD-grown h-BN, but without GQD in it. We didn't observe Coulomb diamonds in such devices (Figure 18 and 19).

Furthermore, the conductivity of such devices is significantly lower than that for devices with GQD, which proves that the Coulomb diamonds we observe are indeed coming from the GQD.

The schematics of the formation of the diamonds are presented in Figure 20a-c. When the size quantisation levels in the GQD are positioned outside of the bias window – no current flows through the quantum dots. At positive biases, a finite conductance starts to be observed once the size quantization level is below the Fermi level in the top graphene (such events are modelled by red lines in Figure 20d) and above the Fermi level in the bottom graphene (modelled by blue lines in Figure 20d). The combination of four of such lines gives a diamond of low conductivity. If the Fermi level in one of the graphene contacts is close to the Dirac point, where the density of states vanishes – the electrostatics dictates[45] that the edges of the diamonds will not be straight lines anymore and will have square root dependence in the V_g-V_b coordinates, Figure 20d. Such events indeed can be observed in our measurements, Figure 17f.

The width of the diamonds in V_b gives the characteristic energy required to place an extra electron into the quantum dot. For our 13 nm and 7 nm quantum dots we measure it to be of the order of 80 meV and 160 meV respectively, well in line with what is expected for the size quantization for quantum dots of such a diameter[46-48]. The fact that the size quantization energy scales as expected with the size of the GQD serves as an additional argument that the tunneling occurs through the states in the quantum dots.

Simultaneously with the characteristic diamonds, a few peaks which approximately follow the square root behaviour have been observed. The square root behaviour is coming from the linear density of states in the graphene electrodes and the fact that, due to the small density of states the bottom graphene electrode doesn't entirely screen the electric field from the gate[49]. We attribute these features to the tunneling through localized states in the central GQD layer[50, 51]. Each localized state produces two lines in G (V_g, V_b) – when it aligns with the Fermi level in the bottom and in the top graphene contacts. The energy positions of these lines can be fitted with very high precision (Figure 17d,f). From such a fitting we can extract the energy position of the localized states with respect to the Dirac points in the graphene layers as well as their spatial positions in the barrier. Thus, we found that all the localized states are indeed located in the central layer (h-BN with GQDs), and their energy covers the range of ±150 meV in the vicinity of the Dirac points in the contacts.

In our diagrams, each set of diamonds corresponds to a particular graphene quantum dot. Thus, we can estimate the number of GQDs involved in tunneling – which gives us approximately 40 quantum dots connected in parallel for the device with 13 nm GQD. At the same time, the number of localized states we can see in our devices is very low (between 3 and 6, depending on the particular device) much

lower than the number of the GQD observed. This suggests that the edges of our GQDs are well passivated and do not produce additional localized states. Also, the number of GQDs we see participating in tunneling is much smaller than the total number of GQDs within the area of the device (~50 GQD per μm^2, the total area of the device ~30 μm^2 for the sample with 13 nm GQD). Currently we don't have an explanation for this effect. We can speculate, however, that as it is silicon gate (which is 300 nm away) which provides the most efficient screening (graphene electrodes provide only weak screening) – GQD within 300 nm radius interact strongly between themselves via Coulomb interaction. It means that the Coulomb diamonds we see are the result of the collective behaviour of several GQDs within 300 nm radius. This would also explain the different intensity of the conductivity peaks.

In order to avoid the large number of GQDs to be connected in parallel, thus obscuring the Coulomb diamonds, we prepared h-BN with low density of graphene islands. To this end we used a strongly diluted micellar solution to achieve low concentration of H_2PtCl_6. To this end 1 mL of the PS-P4VP copolymer solution with H_2PtCl_6 was diluted by 400 mL of pure PS-P4VP. The mixed solution was spin-coated on the SiO_2 substrate, and the micellar film was treated by oxygen plasma to produce Pt NPs. The h-BN monolayer was transferred onto the Pt NPs/SiO_2 substrate, and the conversion reaction was performed for conversion of the hBN on Pt NPs to graphene. After the aqua regia treatment to remove Pt NPs, we obtained a GQD/h-BN sample with a relatively long spacing (0.5 to 1.5 μm), as shown in Figure 21a. Note, that this method gives non-uniform distribution of GQDs.

We used this h-BN with low density GQDs to prepare single electron tunneling transistors Si/SiO_2/30nm_h-BN/Gr/2h-BN/CVD_h-BN/2h-BN/Gr/20nm_h-BN as it has been described above, Figure 17a. The conductance of one of our device (with the active area 30 μm^2) as a function of the gate and bias voltages is presented on Figure 21b. Note, that the characteristic conductance for such a device is at least an order of magnitude smaller that for devices with periodic, high density arrays of GQDs (see the data presented on Figure 17). This is because the tunneling now occurs through a smaller number of GQDs. At the same time, the Coulomb diamonds are visible much clearer in such devices, Figure 21b.

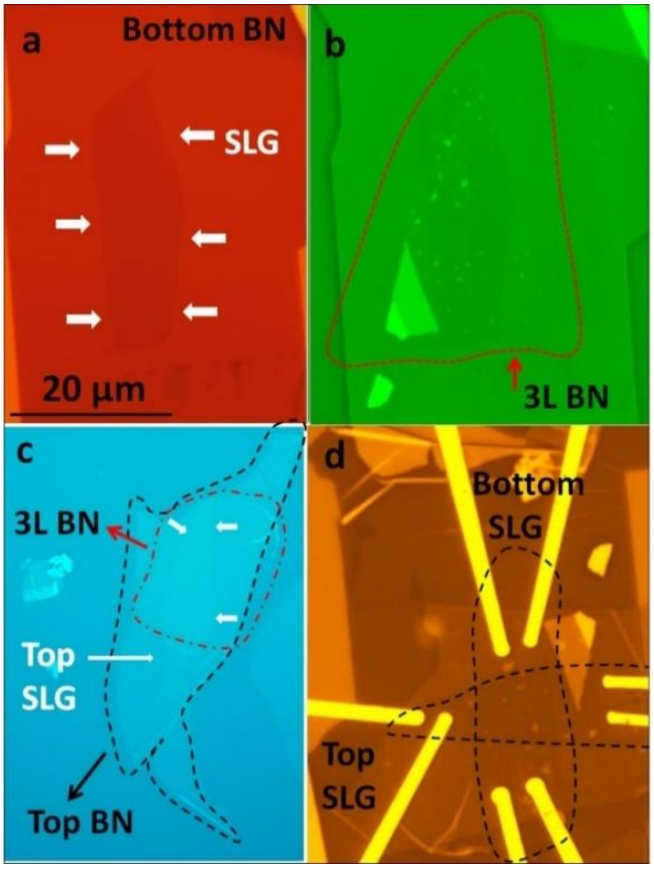

Figure 16. Fabrication procedure for van der Waals tunnel heterostructure comprising the stack of Si/SiO_2/20nm_h-BN/SLG/3L_h-BN/GQD_h-BN/3L_h-BN/SLG/10nm_h-BN. (a) Single layer graphene (SLG), indicated by white arrows, was transferred by flake peeling method on bottom h-BN supported on Si/SiO_2 substrate. (b) Trilayer h-BN, outlined by red dashed line, was then transferred on SLG shown in (a). (c) Separately a PMMA membrane was prepared with ~ 10nm h-BN, another SLG and trilayer h-BN was picked up using this h-BN. This PMMA membrane containing the stack of 3L_h-BN/SLG/10_h-BN was further aligned and dropped on GQD_h-BN on Si/SiO_2. To release this stack from Si/SiO_2, wet transfer procedure following standard KOH etching procedure was performed. (d) Finally, the heterostructure of GQD_h-BN/3L_h-BN/SLG/10nm_h-BN was aligned, and transferred on Si/SiO_2/20nm_h-BN/SLG/3L_h-BN shown in (b). Contacts to top and bottom SLG, as shown in (d), were made by standard electron beam lithography. Scale bar shown in (a) is same for all images.

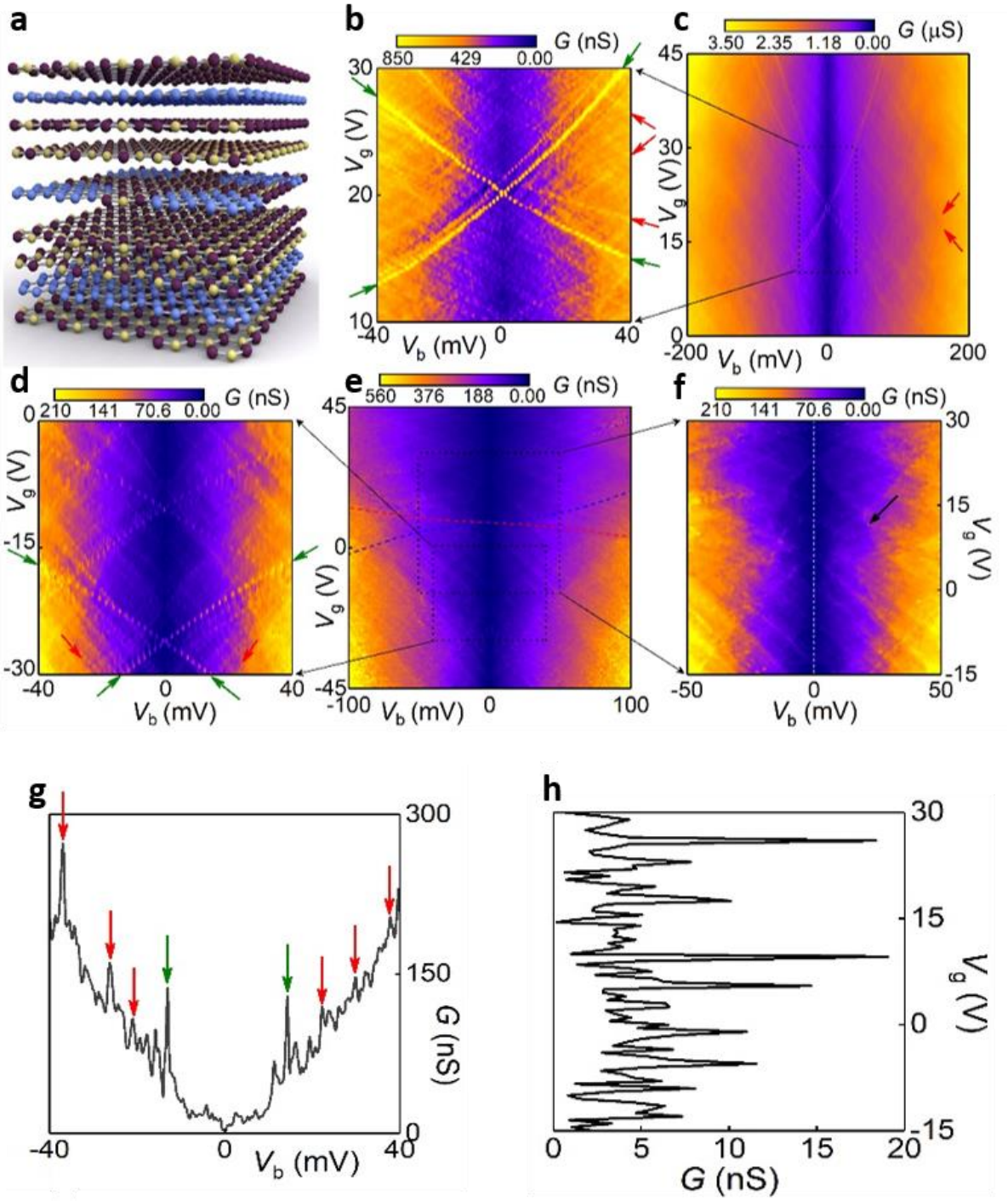

Figure 17. The h-BN/Gr/2h-BN/GQD/2h-BN/Gr/h-BN multi-channel single electron tunneling transistors. (a) Schematic structure of the van der Waals stack. Double layer graphene system separated by hexagonal boron nitride layers with GQDs embedded in the central layer of h-BN. (b) The low excitation measurements of low bias region of (c). Green arrows indicate the tunneling events through the localized impurity states in the middle h-BN layer with 7 nm GQD. Impurity assisted features

correspond to the localized state which is located approximately 90 meV above the Dirac points in the graphene contacts. (c) $G(V_g,V_b)$ for a device with 7 nm GQDs. (d) The low excitation measurements of low bias region of (e), indicating the tunneling events through the localized density of states in the middle h-BN layer with 13 nm GQD. The olive arrows denote the localized states with the energy 140 meV below the Dirac point. (e) $G(\underline{V}_g,V_b)$ for a device with 13 nm GQDs. The red (blue) dashed line mark the event of the Fermi level in the top (bottom) graphene layer aligning with the Dirac point. (f) The magnified plot of (e) denoting a peculiar shape of the Coulomb diamonds when the Fermi level in one of the graphene contacts aligns with the Dirac point. The dashed grey line indicates the cross-section presented in (h). (g) The conductance G(-30V, V_b) plot indicating both peaks of prominent peaks of overlapping diamond boundaries (red arrows) and background of peaks from impurity assisted-tunneling (green arrows) for a device with 13 nm GQD. (h) The conductance $G(V_g$, 0mV) plot indicating peaks occurring from overlapping diamonds in (f). Red arrows in all the plots indicate conductivity peaks which correspond to tunneling through single electron states in GQD.

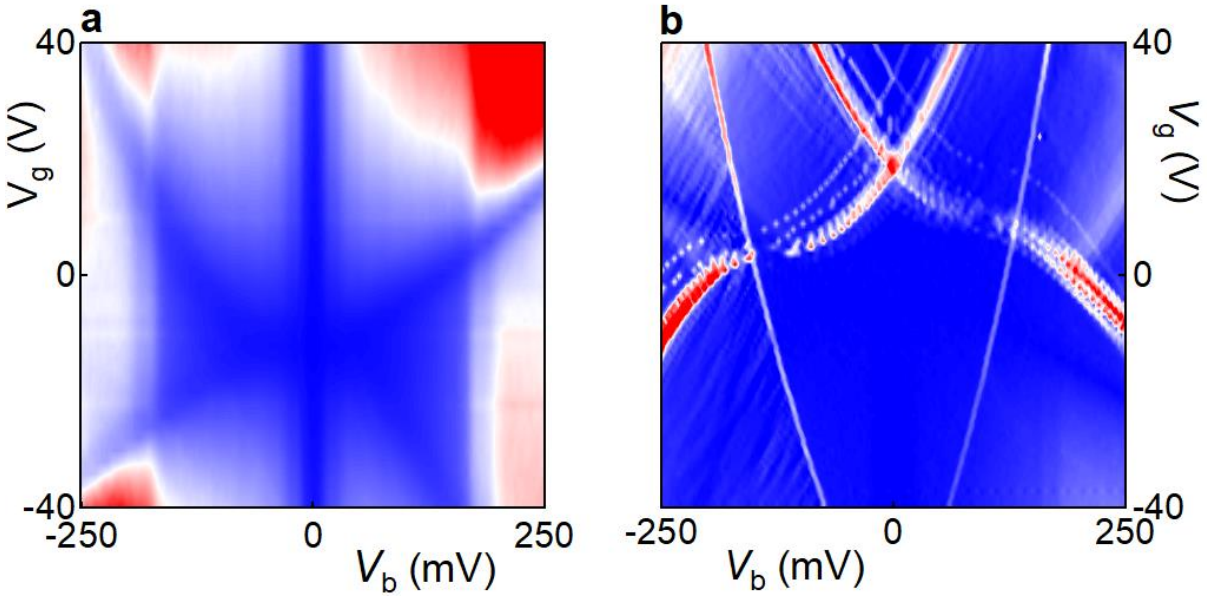

Figure 18. T = 1.5K tunneling conductance $G(V_b,V_g)$ of Si/SiO_2 substrate supported Gr/h-BN/Gr heterostructures. (a) Tunneling through pristine h-BN trilayer mounted in-between two graphene monolayers (colour scale is blue to white to red, 20nS to 2μS to 4μS). Dark Blue X shaped region corresponds to the event of the passage of chemical potential through DPs of graphene layers; vertical features represent phonon-assisted resonant tunneling process. (b) Tunneling through impurity states of low quality tetralayer h-BN mounted in-between monolayer graphene electrodes (colour scale is blue to white to red, 0nS to 20nS to 40nS). Peaks in conductance (red and white) correspond to the tunneling through localized states and follow the square root dependence.

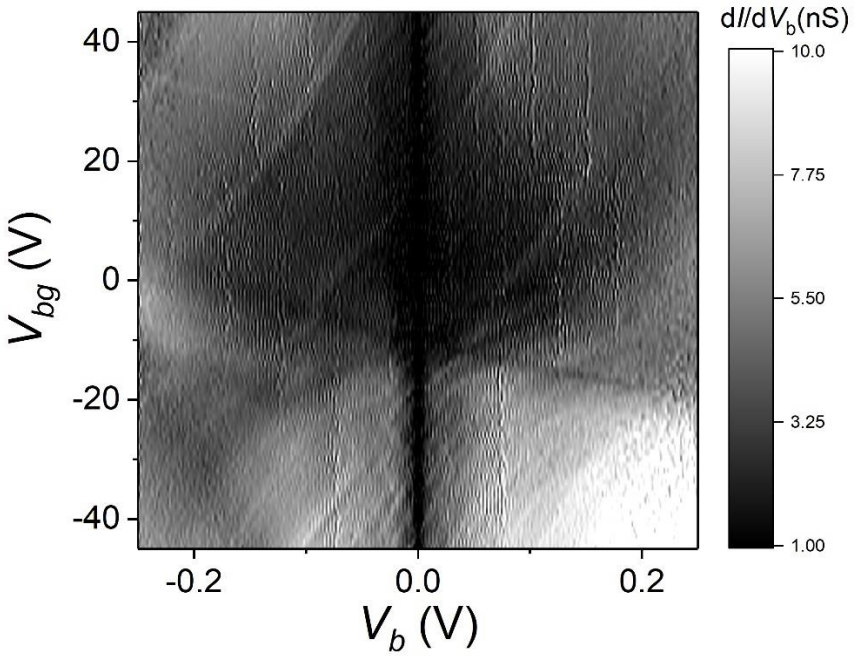

Figure 19. T = 260 mK tunneling conductance $G(V_b,V_g)$ of Si/SiO_2 substrate supported h-BN/Gr/2h-BN/CVD h-BN/2h-BN/Gr/h-BN heterostructure. The area of the device is 82 μm^2. Note, the middle h-BN monolayer was grown by CVD, but no GQD were formed on it. Note, significantly lower conductivity (even though the area of the device is significantly larger than for those presented in the main text) due to the absence of the additional conductance channels due to GQD. There is a small number of the impurity states, however, which might be originating from either defect in the CVD h-BN or due to contamination in between the layers introduced during the fabrication.

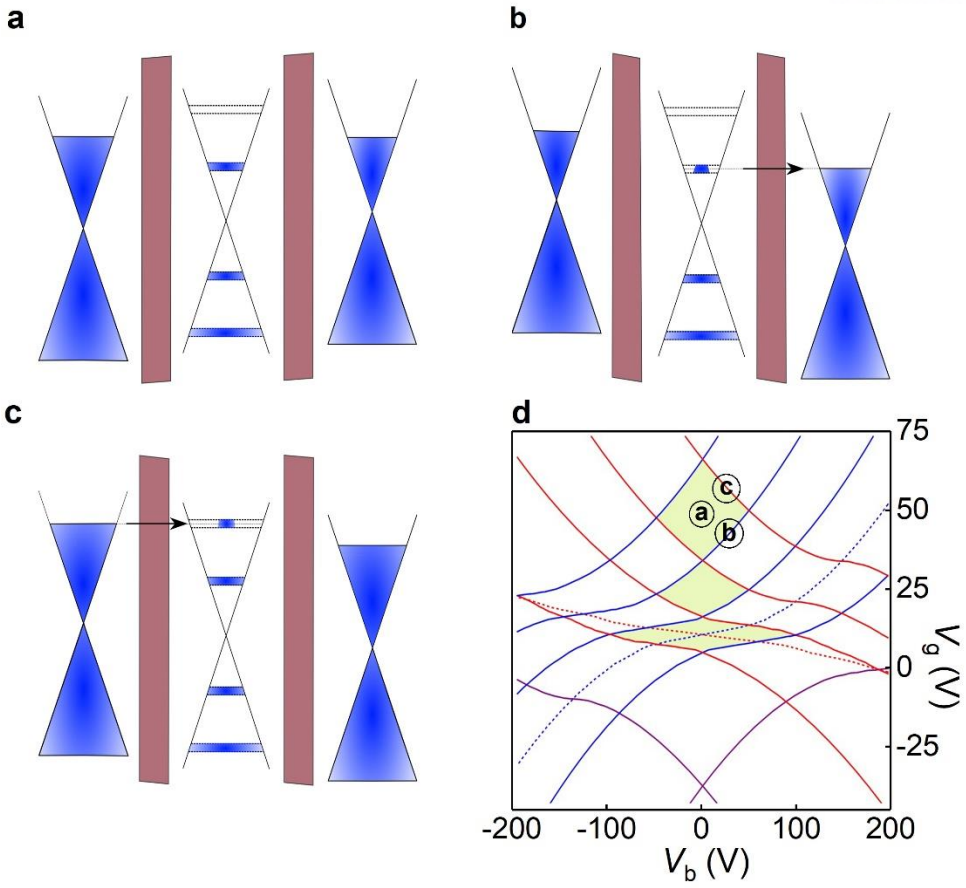

Figure 20. Modelling of the single electron charging effect. (a-c) Schematic representation of a single electron charging effect. The corresponding electrostatic lines are denoted in (d). (d) Modelling example of the alignment of the different energy levels in a device with 13 nm GQD. Red (blue) dashed lines - Fermi level in top (bottom) graphene electrode aligning with the Dirac point. Purple lines – Fermi levels in the graphene contacts being aligned with the localized state located in the middle h-BN layer with energy 140 meV below the Dirac point. The set of solid red (blue) lines correspond to single electron energy levels in GQD aligning with the Fermi level in the top (bottom) electrode. Space between four of such lines forms a Coulomb blockade diamond. Note the distorted shape of the diamond when the Fermi level in the contacts passes through the Dirac points.

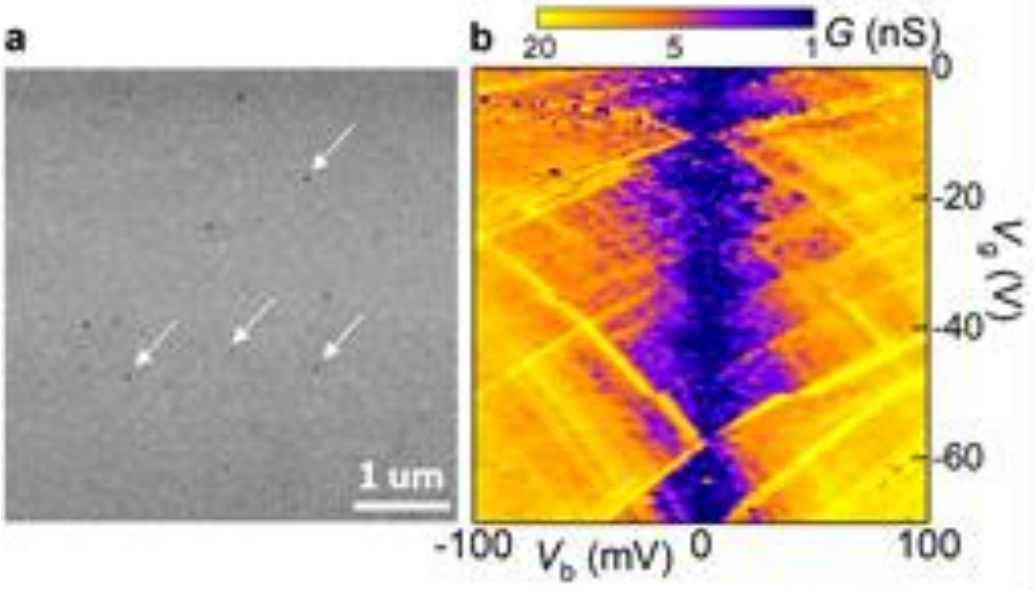

Figure 21. Low density non-periodic array of GQD embedded in h-BN matrix and h-BN/Gr/2h-BN/GQD/2h-BN/Gr/h-BN multi-channel single electron tunneling transistors based on such GQD. (a) SEM image of a GQD/h-BN sample obtained after the transfer of h-BN monolayer Pt NPs/SiO_2 substrate and the conversion reaction. It shows GQDs with a long spacing (0.5 to 1.5 μm), marked by white arrows. (b) $G(V_g,V_b)$ for a device with such GQDs.

4.5 Conclusion

In conclusion, we accomplished the formation of uniform GQD arrays embedded in a h-BN sheet using spatially controlled conversion of h-BN on Pt NPs array. This method not only enables to fabricate uniform size-controllable GQD arrays, but also to realize new optical property of the GQD because of the contact of the graphene edges with h-BN. Furthermore, the geometry allows easy incorporation into van der Waals heterostructures, where we demonstrate single electron tunneling transistors. Our approach – the combination between the in-plane and van der Waals heterostructures – allows the fabrication of high quality graphene quantum dots for transport experiments. The in-plane heterostructures allow fabrication of graphene quantum dots without the dangling bonds and localized states at the perimeter. At the same time the van der Waals heterostructures allow fabrication of controlled tunneling barriers, again without any localized states. We hope that our approach will pave the way for many new types of devices and physical phenomena to be studied.

4.6 Reference

1. Liu, F.; Jang, M. H.; Ha, H. D.; Kim, J. H.; Cho, Y. H.; Seo, T. S. Facile synthetic method for pristine graphene quantum dots and graphene oxide quantum dots: origin of blue and green luminescence. *Adv. Mater.* **2013**, *25*, 3657-3662.
2. Pan, D.; Zhang, J.; Li, Z.; Wu, M. Hydrothermal route for cutting graphene sheets into blue-luminescent graphene quantum dots. *Adv. Mater.* **2010**, *22*, 734-738.
3. Zhuo, S.; Shao, M.; Lee, S.-T. Upconversion and downconversion fluorescent graphene quantum dots: ultrasonic preparation and photocatalysis. *ACS Nano* **2012**, *6*, 1059-1064.
4. Ponomarenko, L.; Schedin, F.; Katsnelson, M.; Yang, R.; Hill, E.; Novoselov, K.; Geim, A. Chaotic Dirac billiard in graphene quantum dots. *Science* **2008**, *320*, 356-358.
5. Stampfer, C.; Güttinger, J.; Molitor, F.; Graf, D.; Ihn, T.; Ensslin, K. Tunable Coulomb blockade in nanostructured graphene. *Appl. Phys. Lett.* **2008**, *92*, 012102.
6. Stampfer, C.; Schurtenberger, E.; Molitor, F.; Guttinger, J.; Ihn, T.; Ensslin, K. Tunable graphene single electron transistor *Nano Lett.* **2008**, *8*, 2378-2383.
7. Neubeck, S.; Ponomarenko, L. A.; Freitag, F.; Giesbers, A.; Zeitler, U.; Morozov, S. V.; Blake, P.; Geim, A. K.; Novoselov, K. S. From one electron to one hole: quasiparticle counting in graphene quantum dots determined by electrochemical and plasma etching. *Small* **2010**, *6*, 1469-1473.
8. Lee, J.; Kim, K.; Park, W. I.; Kim, B.-H.; Park, J. H.; Kim, T.-H.; Bong, S.; Kim, C.-H.; Chae, G.; Jun, M.; Hwang, Y.; Jung, Y. S.; Jeon, S. Uniform graphene quantum dots patterned from self-assembled silica nanodots. *Nano Lett.* **2012**, *12*, 6078-6083.
9. Levendorf, M. P.; Kim, C.-J.; Brown, L.; Huang, P. Y.; Havener, R. W.; Muller, D. A.; Park, J. Graphene and boron nitride lateral heterostructures for atomically thin circuitry. *Nature* **2012**, *488*, 627.
10. Havener, R. W.; Kim, C.-J.; Brown, L.; Kevek, J. W.; Sleppy, J. D.; McEuen, P. L.; Park, J. Hyperspectral imaging of structure and composition in atomically thin heterostructures. *Nano Lett.* **2013**, *13*, 3942-3946.
11. Liu, Z.; Ma, L.; Shi, G.; Zhou, W.; Gong, Y.; Lei, S.; Yang, X.; Zhang, J.; Yu, J.; Hackenberg, K. P.; Babakhani, A.; Idrobo, J.-C.; Vajtai, R.; Lou, J.; Ajayan, P. M. *Nat. Nanotechnol.* **2013**, *8*, 119-124.
12. Sutter, P.; Cortes, R.; Lahiri, J.; Sutter, E. Interface formation in monolayer graphene-boron nitride heterostructures. *Nano Lett.* **2012**, *12*, 4869-4874.
13. Gao, Y.; Zhang, Y.; Chen, P.; Li, Y.; Liu, M.; Gao, T.; Ma, D.; Chen, Y.; Cheng, Z.; Qiu, X.; Duan, W.; Liu, Z. Toward monolayer uniform hexagonal boron nitride–graphene patchworks with zigzag linking edges. *Nano Lett.* **2013**, *13*, 3439-3443.

14. Liu, L.; Park, J.; Siegel, D. A.; McCarty, K. F.; Clark, K. W.; Deng, W.; Basile, L.; Idrobo, J. C.; Li, A.-P.; Gu, G. Heteroepitaxial growth of two-dimensional hexagonal boron nitride templated by graphene edges. *Science* **2014**, *343*, 163-167.
15. Lu, J.; Zhang, K.; Liu, X. F.; Zhang, H.; Sum, T. C.; Neto, A. H. C.; Loh, K. P. Order–disorder transition in a two-dimensional boron–carbon–nitride alloy. *Nat. Commun.* **2013**, *4*, 2681.
16. Kim, G.; Lim, H.; Ma, K. Y.; Jang, A.-R.; Ryu, G. H.; Jung, M.; Shin, H.-J.; Lee, Z.; Shin, H. S. Catalytic conversion of hexagonal boron nitride to graphene for in-plane heterostructures. *Nano Lett.* **2015**, *15*, 4769-4775.
17. Chen, L.; He, L.; Wang, H. S.; Wang, H.; Tang, S.; Cong, C.; Xie, H.; Li, L.; Xia, H.; Li, T.; Wu, T.; Zhang, D.; Deng, L.; Yu, T.; Xie, X.; Jiang, M. Oriented graphene nanoribbons embedded in hexagonal boron nitride trenches. *Nat. Commun.* **2017**, *8*, 14703.
18. Li, J.; Shenoy, V. B. Graphene quantum dots embedded in hexagonal boron nitride sheets. *Appl. Phys. Lett.* **2011**, *98*, 013105.
19. He, J.; Chen, K.-Q.; Fan, Z.-Q.; Tang, L.-M.; Hu, W. Transition from insulator to metal induced by hybridized connection of graphene and boron nitride nanoribbons. *Appl. Phys. Lett.* **2010**, *97*, 239.
20. Zhou, Y.; Wang, Z.; Yang, P.; Gao, F. Novel electronic and magnetic properties of graphene nanoflakes in a boron nitride layer. *J. Phys. Chem. C* **2012**, *116*, 7581-7586.
21. Kim, G.; Jang, A. R.; Jeong, H. Y.; Lee, Z.; Kang, D. J.; Shin, H. S. Growth of high-crystalline, monolayer hexagonal boron nitride on recyclable platinum foil. *Nano Lett.* **2013**, *13*, 1834-1839.
22. Kim, S.-S.; Park, M. J.; Kim, J.-H.; Ahn, G.; Ryu, S.; Hong, B. H.; Sohn, B.-H. Strain-assisted wafer-scale nanoperforation of monolayer graphene by arrayed pt nanoparticles. *Chem. Mater.* **2015**, *27*, 7003-7010.
23. Cançado, L.; Takai, K.; Enoki, T.; Endo, M.; Kim, Y.; Mizusaki, H.; Jorio, A.; Coelho, L.; Magalhaes-Paniago, R.; Pimenta, M. General equation for the determination of the crystallite size of nanographite by Raman spectroscopy. *Appl. Phys. Lett.* **2006**, *88*, 163106.
24. Romanos, J.; Beckner, M.; Stalla, D.; Tekeei, A.; Suppes, G.; Jalisatgi, S.; Lee, M.; Hawthorne, F.; Robertson, J. D.; Firlej, L.; Kuchta, B.; Wexler, C.; Yu, P.; Pfeifer, P. Infrared study of boron–carbon chemical bonds in boron-doped activated carbon. *Carbon* **2013**, *54*, 208-214.
25. Lu, J.; Gomes, L. C.; Nunes, R. W.; Neto, A. H. C.; Loh, K. P. Lattice relaxation at the interface of two-dimensional crystals: Graphene and hexagonal boron-nitride. *Nano Lett.* **2014**, *14*, 5133-5139,
26. Peng, J.; Gao, W.; Gupta, B. K.; Liu, Z.; Romero-Aburto, R.; Ge, L.; Song, L.; Alemany, L. B.; Zhan, X.; Gao, G.; Vithayathil, S. A.; Kaipparettu, B. A.; Marti, A. A.; Takuya, H.; Zhu, J.-J.; Ajayan, P. M. Graphene quantum dots derived from carbon fibers *Nano Lett.* **2012**, *12*, 844-849.
27. Dong, Y.; Chen, C.; Zheng, X.; Gao, L.; Cui, Z.; Yang, H.; Guo, C.; Chi, Y.; Li, C. M. One-step and

high yield simultaneous preparation of single-and multi-layer graphene quantum dots from CX-72 carbon black. *J. Mater. Chem.* **2012**, *22*, 8764-8766.

28. Jin, S. H.; Kim, D. H.; Jun, G. H.; Hong, S. H.; Jeon, S. Tuning the photoluminescence of graphene quantum dots through the charge transfer effect of functional groups. *ACS Nano* **2013**, *7*, 1239-1245.
29. Zhu, S.; Zhang, J.; Tang, S.; Qiao, C.; Wang, L.; Wang, H.; Liu, X.; Li, B.; Li, Y.; Yu, W.; Wang, X.; Sun, H.; Yang, B. Surface chemistry routes to modulate the photoluminescence of graphene quantum dots: From fluorescence mechanism to up-conversion bioimaging applications. *Adv. Func. Mater.* **2012**, *22*, 4732-4740.
30. Gupta, V.; Chaudhary, N.; Srivastava, R.; Sharma, G. D.; Bhardwaj, R.; Chand, S. Luminscent graphene quantum dots for organic photovoltaic devices. *J. Am. Chem. Soc.* **2011**, *133*, 9960-9963.
31. Sk, M. A.; Ananthanarayanan, A.; Huang, L.; Lim, K. H.; Chen, P. Revealing the tunable photoluminescence properties of graphene quantum dots. *J. Mater. Chem. C* **2014**, *2*, 6954-6960.
32. Yoon, H.; Chang, Y. H.; Song, S. H.; Lee, E. S.; Jin, S. H.; Park, C.; Lee, J.; Kim, B. H.; Kang, H. J.; Kim, Y. H.; Jeon, S. Intrinsic photoluminescence emission from subdomained graphene quantum dots. *Adv. Mater.* **2016**, *28*, 5255-5261.
33. Tran, T. T.; Bray, K.; Ford, M. J.; Toth, M.; Aharonovich, I. Quantum emission from hexagonal boron nitride monolayers. *Nat. Nanotechnol.* **2016**, *11*, 37-41.
34. Bourrellier, R.; Meuret, S.; Tararan, A.; Stéphan, O.; Kociak, M.; Tizei, L. H.; Zobelli, A. Bright UV Single Photon Emission at Point Defects in h-BN. *Nano Lett.* **2016**, *16*, 4317-4321.
35. Tran, T. T.; Elbadawi, C.; Totonjian, D.; Lobo, C. J.; Grosso, G.; Moon, H.; Englund, D. R.; Ford, M. J.; Aharonovich, I.; Toth, M. Robust multicolor single photon emission from point defects in hexagonal boron nitride. *ACS Nano* **2016**, *10*, 7331-7338.
36. Sutter, P.; Lahiri, J.; Albrecht, P.; Sutter, E. Chemical vapor deposition and etching of high-quality monolayer hexagonal boron nitride films. *ACS nano* **2011**, *5*, 7303-7309.
37. Barrios-Vargas, J. E.; Mortazavi, B.; Cummings, A. W.; Martinez-Gordillo, R.; Pruneda, M.; Colombo, L.; Rabczuk, T.; Roche, S. Electrical and thermal transport in coplanar polycrystalline graphene–hbn heterostructures. *Nano Lett.* **2017**, *17*, 1660-1664.
38. Withers, F. *et al.* Light-emitting diodes by band-structure engineering in van der Waals heterostructures. *Nat. Mater.* **2015**, *14*, 301-306.
39. Khestanova, E.; Guinea, F.; Fumagalli, L.; Geim, A. K.; Grigorieva, I. V. Universal shape and pressure inside bubbles appearing in van der Waals heterostructures. *Nat. Commun.* **2016**, *7*, 12587.
40. Liu, X. M.; Watanabe, K.; Taniguchi, T.; Halperin, B. I.; Kim, P. Quantum Hall drag of exciton condensate in graphene. *Nat. Phys.* **2017**, *13*, 746-748.
41. Wang, L. *et al.* One-dimensional electrical contact to a two-dimensional material. *Science* **2013**,

342, 614-617.

42. Vdovin, E. E. *et al.* Phonon-Assisted Resonant Tunneling of Electrons in Graphene-Boron Nitride Transistors. *Phys. Rev. Lett.* **2016**, *116*, 186603.
43. De Franceschi, S. *et al.* Single-electron tunneling in InP nanowires. *Appl. Phys. Lett.* **2003**, *83*, 344-346.
44. Britnell, L.; Gorbachev, R. V.; Jalil, R.; Belle, B. D.; Schedin, F.; Mishchenko, A.; Georgiou, T.; Katsnelson, M. I.; Eaves, L.; Morozov, S. V.; Peres, N. M. R.; Leist, J.; Geim, A. K.; Novoselov, K. S.; Ponomarenko, L. A. *Science* **2012**, *335*, 947-950.
45. Mishchenko, A. *et al.* Twist-controlled resonant tunnelling in graphene/boron nitride/graphene heterostructures. *Nat. Nanotechnol.* **2014**, *9*, 808-813.
46. Chen, H. Y.; Apalkov, V.; Chakraborty, T. Fock-Darwin states of dirac electrons in graphene-based artificial atoms. *Phys. Rev. Lett.* **2007**, *98*, 186803.
47. Zhang, Z. Z.; Chang, K.; Peeters, F. M. Tuning of energy levels and optical properties of graphene quantum dots. *Phys. Rev. B* **2008**, *77*, 5.
48. Zarenia, M.; Pereira, J. M.; Chaves, A.; Peeters, F. M.; Farias, G. A. Simplified model for the energy levels of quantum rings in single layer and bilayer graphene. *Phys. Rev. B* **2010**, *81*, 045431.
49. Li, L. H.; Tian, T.; Cai, Q.; Shih, C.-J.; Santos, E. J. G. Asymmetric electric field screening in van der Waals heterostructures. *Nat. Commun.* **2018**, *9*, 1271.
50. Chandni, U.; Watanabe, K.; Taniguchi, T.; Eisenstein, J. P. Evidence for defect-mediated tunneling in hexagonal boron nitride-based junctions. *Nano Lett.* **2015**, *15*, 7329-7333.
51. Chandni, U.; Watanabe, K.; Taniguchi, T.; Eisenstein, J. P. Signatures of phonon and defect-assisted tunneling in planar metal-hexagonal boron nitride-graphene junctions. *Nano Lett.* **2016**, *16*, 7982-7987.

[Publication List]

1. Planar and van der Waals Heterostructures for Vertical Tunnelling Single Electron Transistors

G. Kim, S. S. Kim, J. Jeon, S. I. Yoon, S. Hong, Y. J. Cho, A. Misra, S. Ozdemir, D. Ghazaryan, A. Mishchenko, D. V. Andreeva, Y. J. Kim, H. J. Chung, A. K. Geim, K. S. Novoselov*, B. S. Sohn*, H. S. Shin*

Nat. Commun. **2019**, *Accepted*

2. Hexagonal Boron Nitride/Au Substrate for Manipulating Surface Plasmon and Enhancing Capability of Surface-Enhanced Raman Spectroscopy

G. Kim, M. Kim, C. Hyun, S. Hong, K. Y. Ma, H. Lim*, H. S. Shin*

ACS Nano **2016**, *10*, 11156.

3. Catalytic Conversion of Hexagonal Boron Nitride to Graphene for In-Plane Heterostructures

G. Kim, H. Lim, K. Y. Ma, A. R. Jang, G. H. Ryu, M. Jung, H. J. Shin, Z. Lee, H. S. Shin*

Nano Lett. **2015**, *15*, 4769.

4. Growth of High-Crystalline, Monolayer Hexagonal Boron Nitride on Recyclable Platinum Foil

G. Kim, A. R. Jang, H. Y. Jeong, Z. Lee, D. J. Kang, H. S. Shin*

Nano Lett. **2013**, *13*, 1834.

5. AA'-Stacked Trilayer Hexagonal Boron Nitride Membrane for Proton Exchange Membrane Fuel Cells

S. I. Yoon, D. J. Seo, **G. Kim**, M. Kim, C. Y. Jung, Y. G. Yoon, S. H. Joo, T. Y. Kim*, H. S. Shin*

ACS Nano **2018**, *12*, 10764.

6. Evidence of Local Commensurate with Lattice Match of Graphene on Hexagonal Boron Nitride

N. Y. Kim, H. Y. Jeong, J. H. Kim, **G. Kim**, H. S. Shin, Z. Lee*

ACS Nano **2017**, *11*, 7084.

7. Probing Evolution of Twist-Angle-Dependent Interlayer Excitons in $MoSe_2/WSe_2$ van der Waals Heterostructure

P. K. Nayak, Y. Horbatenko, S. Ahn, **G. Kim**, J. U. Lee, K. Y. Ma, A. R. Jang, H. Lim, D. Kim, S. Ryu, H. Cheong, N. Park, H. S. Shin*

ACS Nano **2017**, *11*, 4041.

8. Chemical Vapor-Deposited Hexagonal Boron Nitride as a Scalable Template for High-Performance Organic Field-Effect Transistors

T. H. Lee, K. Kim, **G. Kim**, H. J. Park, D. Scullion, L. Shaw, M. G. Kim, X. Gu, W. G. Bae, J. G. Santos, Z. Lee, H. S. Shin, Y. Nishi, Z. Bao*

Chem. Mater. **2017**, *29*, 2341.

9. Prevention of Transition Metal Dichalcogenide Photodegradation by Encapsulation with h-BN Layers

S. Ahn, **G. Kim**, P. K. Nayak, S. I. Yoon, H. Lim, H. J. Shin, H. S. Shin*

ACS Nano **2016**, *10*, 8973.

10. Wafer-Scale and Wrinkle-Free Epitaxial Growth of Single-Orientated Multilayer Hexagonal Boron Nitride on Sapphire

A. R. Jang, S. Hong, C. Hyun, S. I. Yoon, **G. Kim**, H. Y. Jeong, T. J. Shin, S. O. Park, K. Wong, S. K. Kwak, N. Park, K. Yu. E. Choi, A. Mishcenko, F. Withers, K. Novoselov, H. Lim*, H. S. Shin*

Nano Lett. **2016**, *16*, 3360.

11. Atomic-Scale Dynamics of Triangular Hole Growth in Monolayer Hexagonal Boron Nitride under Electron Irradiation

G. H. Ryu, H. J. Park, J. Ryou, J. Park, J. Lee, **G. Kim**, H. S. Shin, C. W. Bielawski, R. S. Ruoff, S. Hong*, Z. Lee*

Nanoscale **2015**, *7*, 10660.

12. Superstructural Defects and Superlattice Domains in Stacked Graphene

J. M Yuk, H. Y. Jeong, N. Y. Kim, H. J. Park, **G. Kim**, H. S. Shin, R. S. Ruoff, J. Y. Lee*, Z. Lee*

Carbon **2014**, *80*, 755.

13. Stacking of Two-Dimensional Materials in Lateral and Vertical Directions

H. Lim, S. I. Yoon, **G. Kim**, A. R. Jang, H. S. Shin*

Chem. Mater. **2014**, *26*, 4891.

14. Reversibly Light-Modulated Dirac Point of Graphene Functionalized with Spiropyran

A. R. Jang, E. K Jeon, D. Kang, **G. Kim**, B. S. Kim, D. J. Kang, H. S. Shin*

ACS Nano **2012**, *6*, 9207.

Acknowledgements

제주를 떠나 울산을 온 지가 어느덧 10년이 되었네요. 저에게 있어 울산은 제 2의 고향이자 행복한 추억이 가득했던 곳으로 기억될 것입니다. 학부 4년, 대학원과정 6년을 유니스트에서 보내면서 많은 일들이 있었고, 다양한 사람들도 만났습니다. 학위 과정을 마무리하면서 많이 부족한 저를 도와 주신 고마운 분들께 감사의 말을 전하고자 합니다.

먼저, 신현석 교수님! 방황하던 저를 연구실 학부 인턴생으로 받아 주시고, 교수님 덕분에 연구자로서 많은 것들을 경험하고 좋은 성과를 얻을 수 있었습니다. 진심으로 감사 말씀 전합니다. 그리고 바쁘신 와중에서 귀중한 시간 내에 논문 심사 해주신 신형준 교수님, 권순용 교수님, 정후영 교수님, 박혜성 교수님께서 감사드립니다. 6년을 연구실에서 보내면서 함께 고생했던 연구실 사람들에게도 고마움을 전합니다. 저에게 연구의 흥미를 알려주신 현섭이형, 학부생 때부터 많은 도움을 준 영원한 사수 아랑이형, 우리 연구실의 우상 지은누나, 장난도 많이 쳤지만 즐겁게 받아 주신 동우형. 선배님들 고맙습니다. 그리고, 가장 긴 생활을 함께 동고동락했던 나의 동기 성준이 성인이, 앞으로 우리 연구실을 책임질 사랑하는 후배님들 경열이형, 훈주형, 영진이형, 석모, 현태, 민수, 그리고 우리 연구실의 활력소 김해 세자매 혜진이, 초희, 윤정이까지, 모두 감사합니다.

그리고, 가족들과 친구들에게도 감사 인사 드립니다. 제가 너무나 사랑하는 저의 아내 민혜, 오랜 시간 동안 우여곡절이 많았는데 항상 옆자리를 지켜 주어 고맙습니다. 그리고, 언제나 잘하고 있다고 힘을 주셨던, 어무이, 아부지, 사랑하는 나의 동생 명준이, 하늘이, 그리고, 새로운 가족이 된 장인어른, 장모님, 휘곤이형 모두 감사합니다. 항상 나에게 진심 어린 조언을 해주었던 룸메이트 본재, 늙지 않는 영원한 우리 패밀리 재희, 영진이, 득규, 인선이, 기원이, 대학원 생활 하면서 많이 친해진 윤호, 승영이, 언제나 나를 반갑게 맞아주었던 지구경로당 친구들까지. 여러분 덕분에 지치지 않고 학위 과정 잘 마무리 했습니다.

유니스트에서의 10년의 생활을 마치고 새로운 도전을 시작하려고 합니다. 좋은 추억들을 기억하며 항상 최선을 다해 살아가는 모습을 보여드리겠습니다. 그동안 저를 믿어 주시고 도와 주신 모든 분들께 다시 한 번 진심으로 감사드립니다.